ALMA MATER STUDIORUM · UNIVERSITÀ DI BOLOGNA

Scuola di Scienze
Dipartimento di Fisica e Astronomia
Corso di Laurea in Astrofisica e Cosmologia

Radio morphology-accretion mode link in FRII low-excitation radio galaxies

Tesi di Laurea

Presentata da:
Duccio Macconi

Relatore:
Chiar.mo Prof.
Cristian Vignali

Co-relatrici:
Prof.ssa Paola Grandi
Dott.ssa Eleonora Torresi
Dott.ssa Bia Boccardi

Sessione IV
Anno Accademico 2017-2018

This thesis has been carried out at INAF/OAS Bologna as part of the Institute research activities.

Abstract

Radio Galaxies (RG) are Radio-Loud Active Galactic Nuclei (AGN) characterized by powerful relativistic jets, oriented at relatively large inclination angles with respect to the observer's line of sight. The aim of my thesis project is to investigate the connection between gas accretion and jet ejection and propagation. Since RGs are among the most energetic manifestations of the AGN phenomenon, they are extraordinarily relevant to address important issues such as the interaction between Super Massive Black Holes (SMBHs), the radio jets and their environment.

RGs are commonly classified on the basis of their radio morphology into low radio power FRI (core-dominated) and high radio power FRII (lobe-dominated). On the basis of their optical spectra, they are further divided into Low-Excitation Radio Galaxies (LERGs) and High-Excitation RGs (HERGs/BLRGs). This latter classification corresponds to different accretion regimes (efficient vs. inefficient): in particular, HERGs/BLRGs accrete efficiently (quasar-mode), while LERGs are characterized by low excitation modes typical of inefficient accretion regimes (ADAF mode). Almost all HERGs present a FRII radio morphology, while LERGs can assume both FRI and FRII morphologies. LERGs classified as FRII are intriguing sources because they share the same radio properties of HERGs/BLRGs, host BHs with similar masses but are less bright than HERGs/BLRGs in the [OIII] line by a factor of 10; therefore, they are the key targets to fulfill the goal of the present project, i.e. to explore the mutual relationship among accretion, jet power and environment.

To this aim, I reduced and analyzed the X-ray data of all FRII-LERGs (19) belonging to the 3CR sample at $z<0.3$. This is the best suited catalog since it has been extensively observed from radio to X-rays. The X-ray band is essential since it allows to probe the most energetic processes at work on small ($\leq$pc) and large (kpc) scales. In addition, I have reduced and analyzed 31 FRII-HERGs/BLRGs ($z<0.3$) for which public observations were available in the *Chandra* and XMM-*Newton* archives, and I have considered 13 FRI-LERGs data from the literature. These two groups of standard radio galaxies (FRII-HERGs/BLRGs and FRI-LERGs) have been used as control samples.

Three possible scenarios are investigated: (i) FRII-LERGs and FRII-HERGs are the same objects seen through different obscuring screens; (ii) FRII-LERGs form FRII morphologies due to favorable environmental conditions; (iii) FRII-LERGs were powerful HERGs in the past. The main result of this work is that FRII-LERGs have intermediate properties (X-ray luminosity, column density and accretion rate in terms of Eddington luminosity) with respect to FRII-HERGs and FRI-LERGs. The moderate gas column density and accretion rate found in FRII-LERGs favor an evolutionary scenario. The large-scale radio structures could be the heritage of a past AGN activity at higher efficiency, while the nuclear activity has recently decreased due to depletion of the cold gas.

Sommario

Le Radio Galassie (Radio Galaxies) fanno parte dei Nuclei Galattici Attivi (Active Galactic Nuclei) radio emittenti caratterizzati da potenti getti relativistici, orientati con angoli di inclinazione relativamente grandi rispetto alla linea di vista. Dato che le RG sono tra gli AGN più energetici, esse sono straordinariamente rilevanti al fine di affrontare questioni importanti come l'interazione tra i buchi neri supermassivi (Super Massive Black Holes), i getti radio e l'ambiente circostante. Le RG sono comunemente classificate, sulla base della loro morfologia radio, in FRI e FRII, le prime caratterizzate da bassa potenza radio e dominanza dell'emissione nucleare, mentre le seconde da alta potenza radio e dominanza dell'emissione proveniente dai lobi. Tuttavia, esse possono essere classificate anche sulla base dei loro spettri ottici in: RG di bassa eccitazione (Low Excitation Radio Galaxies) e RG di alta eccitazione (High Excitation Radio Galaxies /Broad Lines Radio Galaxies). Quest'ultima classificazione corrisponde a diversi regimi di accrescimento (efficiente o inefficiente): in particolare, is sistemi HERG / BLRG sono associati ad accrescimenti efficienti (quasar-mode), mentre i LERG sono caratterizzati da bassa eccitazione tipica di regimi di accrescimento inefficienti (Advection Dominated Accretion Flow-mode). Quasi tutte le HERG presentano una morfologia radio FRII, mentre le LERG possono assumere entrambe le morfologie (FRI e FRII). Le LERG classificate come FRII costituiscono un'interessante fonte di ricerca poiché condividono le stesse proprietà radio di HERG / BLRG e buchi neri centrali con masse simili, ma sono meno brillanti delle HERG / BLRG nell'emissione in riga dell'[OIII] di circa un fattore di 10. Esse costituiscono quindi il target ideale per raggiungere l'obiettivo del presente progetto, vale a dire esplorare la relazione tra accrescimento, potenza del getto e ambiente delle RG.

A questo scopo ho ridotto e analizzato i dati di tutte i FRII-LERG (19) appartenenti al catalogo 3CR con $z < 0.3$. Questo è il catalogo più adatto dal momento che è stato ampiamente osservato nell'intero spettro elettromagnetico: dalla banda radio ai raggi X. Questi ultimi sono la banda più adatta per lo studio presente poiché consentono di sondare i processi più energetici che operano su piccole (<pc) e grandi (kpc) scale. Inoltre, ho ridotto e analizzato 31 FRII-HERG / BLRG per le quali erano disponibili osservazioni pubbliche negli archivi Chandra e XMM-Newton, e ho considerato 13 FRI-LERG dalla letteratura. Questi due gruppi di radio galassie standard (FRII-HERG / BLRG e FRI-LERG) sono stati utilizzati come campioni di controllo. Al fine di comprendere la natura delle FRII-LERG vengono esaminati tre possibili scenari: (i) FRII-LERG e FRII-HERG sono gli stessi oggetti visti attraverso diversi oscuramenti dovuti all'orientazione; (ii) FRII-LERG hanno morfologie FRII a causa dell'ambiente esterno; (iii) FRII-LERG erano potenti HERG in passato. Il risultato principale di questo lavoro è: le FRII-LERG hanno proprietà intermedie (in termini di: luminosità X, densità delle colonna e tasso di accrescimento) rispetto a FRII-HERG e FRI-LERG. I valori moderati di densità di colonna e il tasso di accrescimento riscontrato in FRII-LERG favoriscono lo scenario evolutivo. Le strutture radio su larga scala potrebbero essere l'eredità di un'attività AGN passata di maggiore efficienza, mentre l'attività nucleare è recentemente diminuita a causa dell'esaurimento del gas freddo.

Contents

Chapter 1

Active Galactic Nuclei

Super Massive Black Holes (SMBHs) inhabit the center of almost all massive galaxies to whom they are intimately related, as attested by the empirical scaling relations between black hole mass and galaxy velocity dispersion [Magorrian et al., 1998, Tremaine et al., 2002, McConnell et al., 2011]. About 99% of them is silent, but a small fraction ($\approx 1\%$) is active: they are called Active Galactic Nuclei (AGN). About 10% of AGN produce strong relativistic jets which emit at radio wavelengths. The AGN presence is revealed not only thanks to jets detection but also via the optical spectrum. In fact, the spectrum of a normal galaxy is the sum of stars, gas and dust emission, while the spectrum of the galaxy which hosts an AGN has stronger emission lines. A comparison between optical spectra of normal galaxy and an AGN is shown in Figure 1.1.

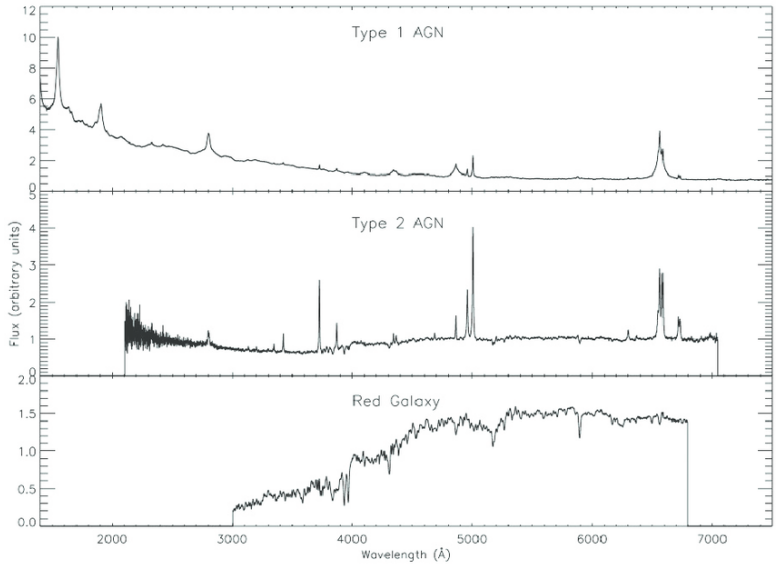

Figure 1.1: Comparison of type 1 (*top panel*) and type 2 (*middle panel*) AGN optical spectra with respect to a normal and red galaxy spectrum (*bottom panel*). Credit: Trump et al. [2007].

AGN are among the most energetic manifestations in the Universe, since they produce an enormous amount of energy in a very small volume ($\ll pc^3$). In fact, as it is shown in Figure 1.2, the galaxy size is about 10^4 times larger than the AGN scale. The enormous amount of energy

is produced by gravitational accretion of matter onto the central BH. Indeed, an AGN is a direct evidence of BH accretion and it is fundamental to address issues related to BH-galaxy formation, evolution and AGN-galaxy interactions.

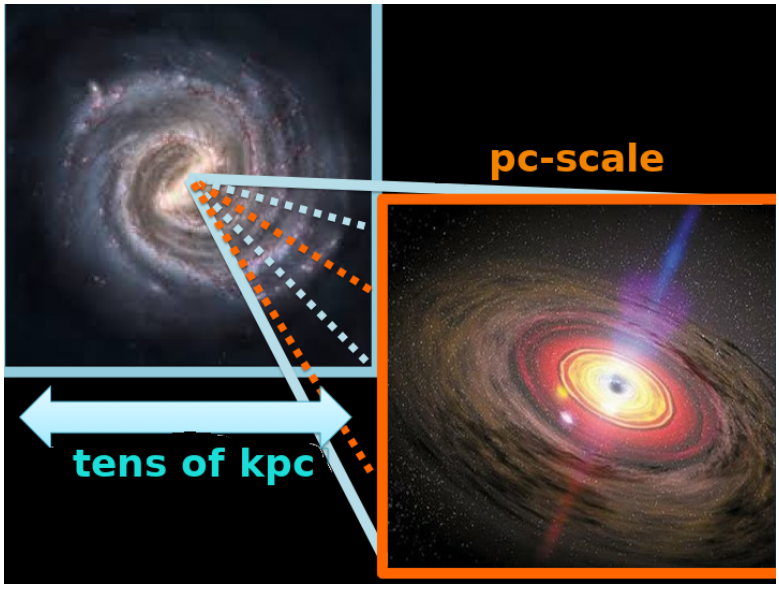

Figure 1.2: *Left panel*: a "face-on" spiral galaxy; *right panel* a zoom on its innermost region, with an AGN at the centre. Credits: `http://star-www.st-and.ac.uk/~ds207/`.

The AGN main constituents are:

- **Central Super Massive Black Hole (SMBH):** its mass can range between $10^6 M_\odot$ and $10^{10} M_\odot$. The SMBH properties are function of three parameters: mass (M), spin (J) and charge (Q). Generally, the last one is assumed as 0, since the BH is thought to be neutral. Instead, J can span between 0 and 1, representing respectively the non-rotating (Schwarzchild metric) and maximally rotating BH (Kerr metric);

- **Hot Corona:** composed by optical thin gas with a temperature of about 10^{8-9} K. It is thought to be located above the disc and be responsible for the hard X-ray continuum emission;

- **Accretion disc:** its temperature spans from $\approx 10^4$ to 10^6 K while its size reaches values up to $\approx 10^4$ R_S[1]. For a disc surrounding a $10^8 M_\odot$ BH, accreting at the Eddington regime (see Section 1.3), the frequency peak emission of the inner part of the disc is in the extreme ultraviolet band (≈ 100 Å);

- **Broad Line Region (BLR):** within $\approx (1-20) \times 10^{16}$ cm from the center, it is thought to comprise a collection of dense clouds (with density values up to 10^{10}cm^{-3}) at 10^4 K. The high density allows the presence of permitted lines only, while the proximity to the SMBH causes high speed rotation of clouds, and consequently, the broadening of spectral lines;

[1] R_S is defined as the Schwarzschild radius and it is equal to $R_S = \frac{2GM}{c^2}$.

- **Torus:** its distance from the BH can range from few pc to tens of pc. It is primarily composed of dust and its composition is still debated between a clumpy or a smooth structure (or a combinations of the two);

- **Narrow Line Regions (NLR):** they occupy a farther region from the center with respect to BLR, reaching distances $\geq$ 100 pc. They are composed of low-density clouds ($10^3 - 10^4 cm^{-3}$) which emit narrow lines in the optical spectrum.

1.1 The Unified Model of AGN

AGNs emit over the entire electromagnetic spectrum. As a consequence, they were discovered and classified separately at different wavelenghts. Therefore the classification of AGNs is complex and based on many different methods (Tadhunter 2008) such as the presence/absence of broad emission lines in the optical spectra, the optical morphology, the radio morphology, the variability, the luminosity or the spectral shape.

An important property of AGN is the *radio loudness*. An AGN is defined Radio-Loud (RL) if the ratio between the radio emission at 5 GHz and the optical flux in the B band (centered at 4400 Å) is equal or higher than 10 [Kellermann et al., 1989]:

$$R = \frac{F_{5GHz}}{F_B} \geq 10 \tag{1.1}$$

This definition was introduced in the framework of a study of 114 sources belonging to Palomar Bright Quasar Survey (BQS) with VLA observations.
A more recent definition of radio loudness was given by Terashima & Wilson in 2003:

$$log(R_X) = \frac{\nu L_\nu(5GHz)}{L_X} \leq -4.5 \tag{1.2}$$

where L_X is the X-ray luminosity in 2-10 keV band. Since X-rays are less affected by extinction than the optical band the latter definition is more appropriate to take into account heavily obscured nuclei ($N_H \geq 10^{23}$ cm^{-2}, $A_V > 50$ mag). Only a small fraction ($\sim$10%) of AGNs is RL (Urry & Padovani 1995), and are hosted in ellitpical galaxies. Antonucci (2011) shows that, in the low–z Universe, there is a near–perfect correspondence between RL objects and elliptical hosts. Instead, Radio-Quiet (RQ) AGNs generally lie in spiral galaxies [Floyd et al., 2004].

1.1.1 AGN optical classification

The first classification of AGN comes from the optical band and is based on the presence and relative strength of emission lines. This classification can be adopted for both RL and RQ sources:

- **Type 1** (face-on): they are characterized by both broad and narrow emission lines above a strong continuum emission. The broad lines Full Width Half Maximum (FWHM) is about 10^{3-4} km s^{-1}. They are permitted lines produced by dense clouds in the sub-parsec scale near the SMBH, in the BLR. Conversely, the narrow lines (FWHM$\approx 10^2$ km s^{-1}) are essentially forbidden lines produced in the NLR. Both radio quiet (Seyfert 1, QSO) and radio loud (Broad Lines Radio Galaxies-High Excitation Radio Galaxies, Quasars) AGN belong to this category;

- **Type 2** (edge-on): they show a weak continuum and only narrow lines emission with FWHM$\approx 10^2$ km s^{-1}. In this group we can find: radio quiet AGN (Seyfert 2) and radio loud AGN (Narrow Lines Radio Galaxies-High Excitation Radio Galaxies, which will be explained in details in a following section);

- **Type 3:** they present low-ionization emission lines and low optical continuum emission. Low-Ionization Nuclear Emission Region galaxies (LINERs) and the Low Excitation Radio Galaxies (LERGs) belong to this group: the former are RQ AGN thought to represent the conjunction point between starburst galaxies and AGN, with a low bolometric luminosity $L_{\rm bol} \approx 10^{41-42}$ erg s^{-1}; LERGs are RL AGN that will be discussed extensively in the next Section.

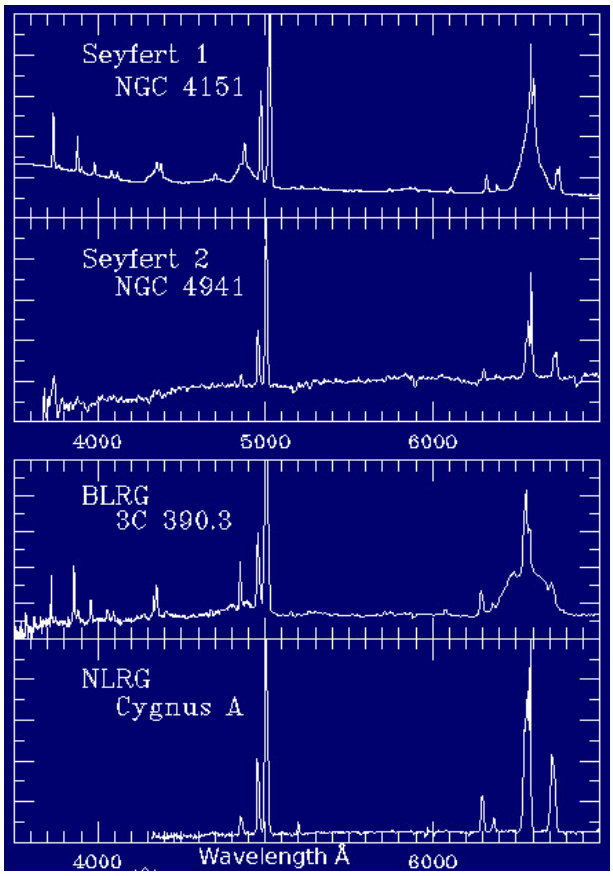

Figure 1.3: Optical spectra of four different AGN classes. From top to bottom panel: Seyfert 1, Seyfert 2, BLRG and NLRG spectrum. The Seyfert 1 and BLRG spectra have both narrow and broad lines, while Seyfert 2 and NLRG present only narrow lines. Credit: William C. Keel.

In Figure 1.3 different AGN optical spectra are shown, both types 1 and 2, RQ and RL AGN. One of the main differences concerns the presence or absence of broad lines. For example, all spectra have the hydrogen emission line of the Balmer series (H_α) at 6563 Å. Its profile is narrow for both Seyfert 2 and NLRG spectra, while for Seyfert 1 and BLRG, it consists of a narrow and a

broad component it applies not only to H_α but also to all the others permitted lines).

In the context of the unified model Antonucci [1993], Urry and Padovani [1995], the central engine of both types 1 and 2 is exactly the same. Their different behavior is caused by anisotropy effects (Tadhunter 2008). For RQ AGN the main cause of anisotropy is the obscuring torus, as shown in Figure 1.4. In Seyfert 1 the continuum is unobscured and broad emission lines are detected, while in Seyfert 2 the BLR emission is obscured by the torus, which intercepts the observer line of sight.

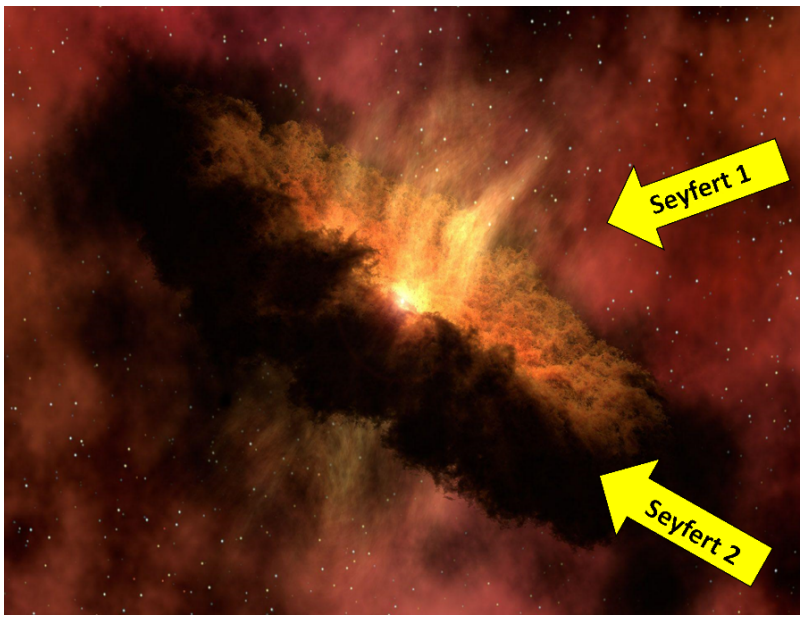

Figure 1.4: Schematic view of the unified model of Seyferts: types 2 are seen through the torus, while types 1 are the unobscured counterparts. Credit: Takuma Izumi.

For RL AGNs, another cause of anisotropy besides the dusty torus is the effect of beaming in relativistic jets. Indeed, blazars are radio sources observed close to the jet axis (low inclination angle, $\theta < 10^\circ$) and, consequently, the jet emission is strongly beamed. For larger angles of view (higher inclination angle $\theta > 10^\circ$), the source is seen as a radio galaxy (see next Section). As pointed out by Tadhunter (2008), the orientation–based unified models (see Figure 1.5) are successful in explaining some aspects of the RL AGN classification, particularly the relationship between narrow and broad line AGNs.

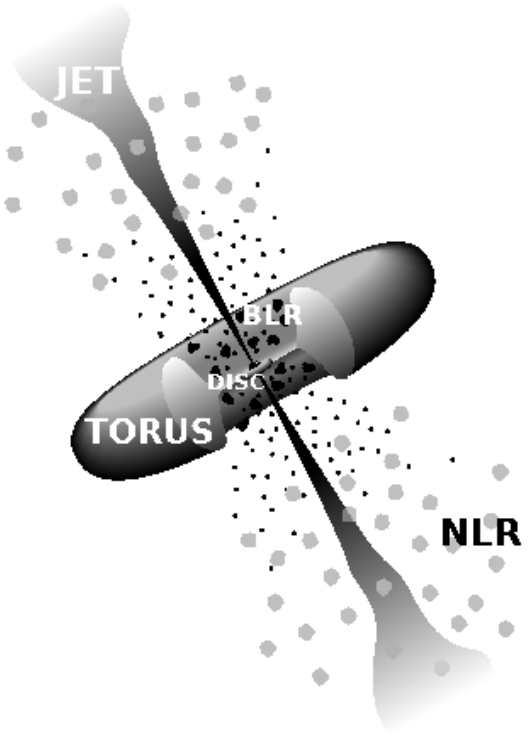

Figure 1.5: A sketch of the unified model of a RL AGN with main features represented: the SMBH, the accretion disc, the torus, the BLRs, the NLRs and the jets. The disc is the innermost structure that surrounds the central BH. It is co-axial with the torus. The BLRs occupy are near to the central engine and can be obscured by the torus (depending on the AGN orientation). Instead, the NLRs occupy are far away from the center and then, if they are present, they are always visible (not orientation-dependent). The jet can reach distances from the center up to hundreds of kpc. Credit: Urry and Padovani [1995].

However, much is still unexplained in the context of the RL/RQ dichotomy. Why RL sources contain relativistic jets which are missing (or are very weak) in RQ objects, is yet an unanswered question.

1.2 Radio-Loud AGN

On the basis of the jet inclination angle with respect to the observer's l.o.s. a Radio-Loud AGN can be a *Blazar* or a *Radio Galaxy*. *Blazars*, i.e. BL Lacs and Flat Spectrum Radio Quasars (FSRQ), are viewed nearly along the jet axis, therefore the non–thermal jet radiation is amplified by relativistic effects giving rise to flat radio spectra, large polarization and strong variability. For example, in Figure 1.6 six spectra of the FSRQ 3C 273 acquired in six different observations from 30 January to 4 April 2011 are shown [Patiño-Álvarez et al., 2013]. It is visually appreciable the variability in terms of emission. Generally, FSRQs show strong emission lines above a continuum (exactly like FSRQ 3C273), while BL Lacs' optical spectra are characterized by the lack of strong emission lines (EW<5 Å).

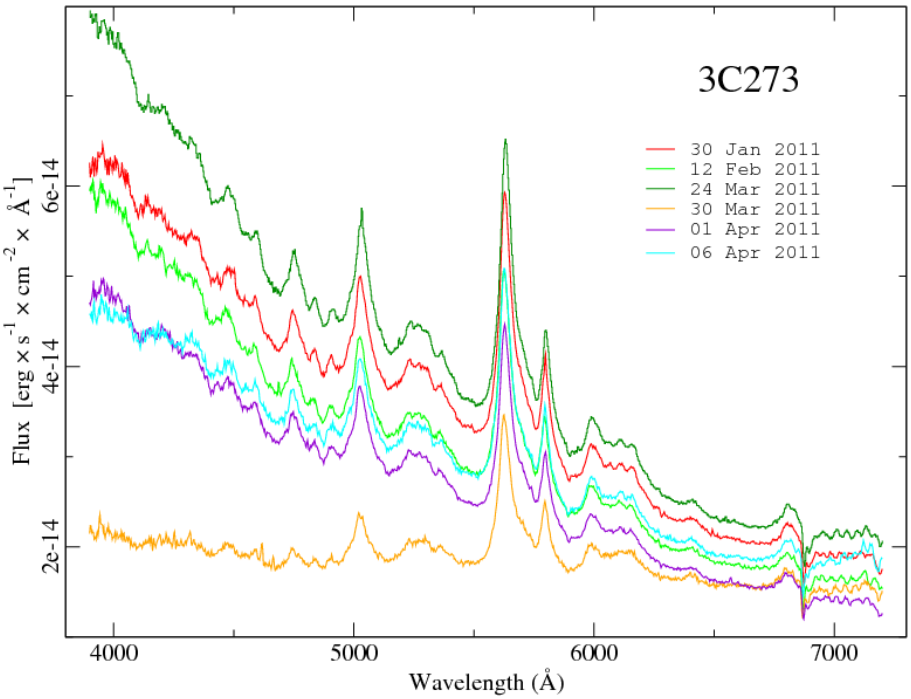

Figure 1.6: Optical spectral variability of the blazar 3C 273 from January to April 2011. Observations were carried out at Observatorio Astrofisico Guillermo Haro (OAGH) in Mexico. The spectral resolution is about 15 Å. Credit: Patiño-Álvarez et al. [2013].

Blazars generally show two-peaked broadband spectral energy distributions (SED) from radio to γ-rays. Synchrotron radiation forms the lower-energy part of the SED from radio to optical/UV. Sometimes it can extends up to the X-ray band. The Compton processes make the X-ray/γ-ray radiation. Blazars are the largest population of AGNs observed in the γ-ray sky [Hartman et al., 1999, Abdo et al., 2010].

1.2.1 Radio galaxies

In the context of the Unified Model, radio galaxies are considered the parent population of blazars, i.e. their misaligned counterparts (Urry & Padovani 1995).
At first, radio galaxies were classified by Fanaroff and Riley [1974], following morphological criteria. They divided sources in Fanaroff-Riley (FR) I, which have bright jets and nucleus (so called edge-darkened), and Fanaroff-Riley II, with their powerful hot-spots and the absence of twin jets (therefore called edge-brightened). In Figure 1.6 the image of a FR II radio galaxy is shown.

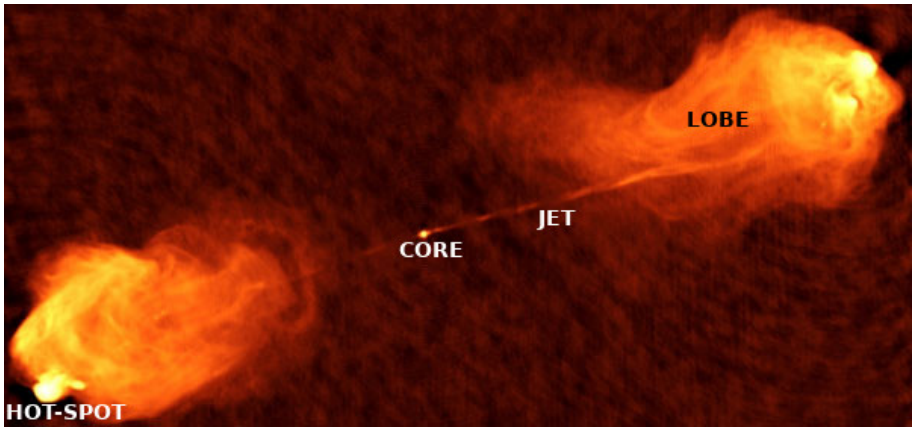

Figure 1.7: Radio image at 6 cm of Cygnus A, one of the most famous FRII radio galaxies. The main components are labeled. Its total extension is about one hundred of kpc.

Fanaroff and Riley used the R_{FR} parameter to classify 57 radio loud AGN of the 3CR catalog. This parameter represents the ratio between the distance from the center of the brightest regions of the source at both sides and the total dimension of the source. For FRI $R_{FR} < 0.5$ while for FRII $R_{FR} > 0.5$. Another relevant distinction factor is represented by the 178 MHz luminosity: sources with $L_{178} < 10^{26}\, WHz^{-1}$[Tadhunter, 2016] are generally FRI, while more luminous sources belong to FRII class. In some cases the threshold between the two classes is very subtle and some objects are characterized by intermediate radio structure, such as hybrid double sources (one side FRI-like and the other FRII-like; Gopal-Krishna and Wiita [2000b]).

The main structural components of a radio galaxy are (see Fig. 1.7):

Core: it is a very compact region with a flat ($\alpha \approx 0$) spectrum in the radio band. Generally is is an unresolved region, even at VLBI sensitivity;

Jets: they are very collimated structures of relativistic plasma, that originate in the central regions of the AGN and can reach distances of several kpc up to Mpc. In the radio and optical band jets emit synchrotron radiation, the resultant spectrum is a power law $S \propto \nu^{-\alpha}$ with $\alpha \sim 0.7$. Jets are visible also in the X–ray band, however the emission process is not completely understood. One possibility is the IC process. If the same electrons producing synchrotron are scattered the resultant mechanism is Synchrotron Self Compton (SSC), while it is External Compton (EC) if Cosmic Microwave Background (CMB) photons are scattered;

Lobes: they are extended sources. They are composed by plasma transported by the jet after shocking with the ISM. The radiation emitted by lobes has non–thermal origin. In the radio band lobes emit synchrotron radiation, while in the X–ray band the emission process can be EC [Kataoka and Stawarz, 2005, Migliori et al., 2007]. Extended lobes can be also the emission site of γ-ray photons as discovered by the Fermi satellite in the radio galaxy Centaurus A and Fornax A [Abdo et al., 2010, Ackermann et al., 2016];

Hot-spots: they are very bright and compact sources produced by the impact of jet on the InterStellar Medium (ISM). When this happens, the jet structure is destroyed and a shock is produced (because the high speed jet impacts against stationary ISM). Then the relativistic

particles are re-accelerated by the shock waves. The radio spectrum has a spectral index of $\sim$0.5 because of the re-acceleration of particles, while the hot-spot X-ray emission can be ascribed to an SSC model with a magnetic field close to equipartition [Wilson et al., 2001] even if there some cases, e.g. Pictor A, in which it is necessary to relax the equipartition condition [Wilson et al., 2001].

In 1994, Laing et al. proposed a different optical classification of radio galaxies, based on the excitation modes in the NLR . They divided RL AGN in High Excitation Radio Galaxies (HERG) and Low Excitation Radio Galaxies (LERG) on the basis of the [OIII] and Hα emission lines. Indeed, they classified as HERGs the RGs with $\frac{[OIII]}{H\alpha} < 0.2$ and [OIII] Equivalent Width[2] (EW)>3 Å. More recently, Buttiglione et al. (2009, 2010, 2011) proposed a new spectroscopic classification scheme on the basis of the Excitation Index (EI), defined as:

$$EI = log(\frac{[OIII]}{H_\beta}) - \frac{1}{3}\left[(\frac{[NII]}{H_\alpha}) + log(\frac{[SII]}{H_\alpha}) + log(\frac{[OI]}{H_\alpha})\right] \tag{1.3}$$

in which $\frac{1}{3}(\frac{[NII]}{H_\alpha}) + log(\frac{[SII]}{H_\alpha}) + log(\frac{[OI]}{H_\alpha})$ is defined Line Ration Index (LRI). The EI represents the overall ratio of high and low excitation emission lines in each source. Buttiglione et al. defined a threshold ($EI = 0.95$) which separate LERGs ($EI < 0.95$) from HERGs ($EI > 0.95$). A clear example is visible in Figure 1.8, in which the EI of about a hundred of RL AGN belonging to 3CR catalog is measured (a detailed description of this catalog and its properties will be made in Section 3.1).

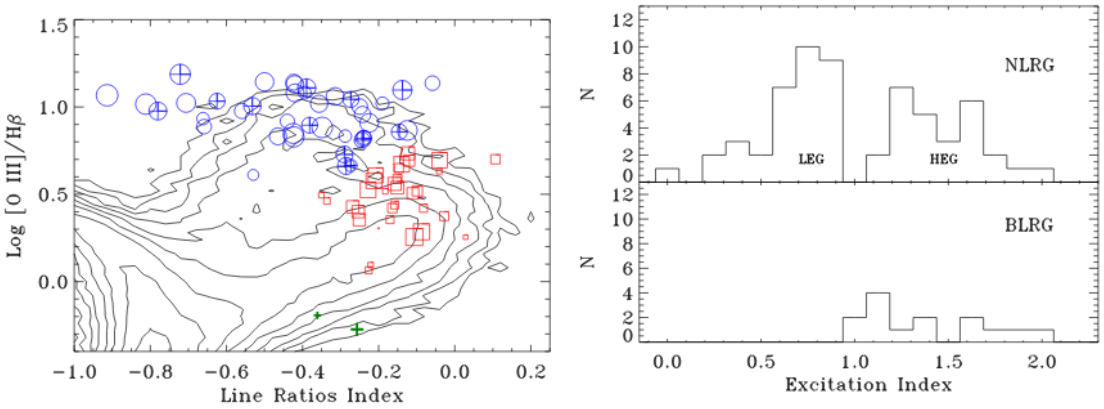

Figure 1.8: *Left panel:* LRI vs log([O III]/Hβ). HERGs are represented by circles, LERGs by squares and Broad Line Radio Galaxies (BLRG) by crossed circles. The contour lines indicate the distribution of the SDSS emission line galaxies [Kewley et al., 2006]. *Right panel:* Excitation Index distribution for NLRGs (*upper panel*) and BLRGs (*lower panel*). Credits: Buttiglione et al. [2010].

Diagnostic diagrams are extremely useful to classify the dominant energy source in emission-line galaxies [Kewley et al., 2006]. They are based on emission lines ratios and were proposed by

[2]The equivalent width is defined as the width of the rectangle with the same area of the observed emission/absorption line area, but with a fixed height.

Baldwin et al. [1981], therefore commonly known as Baldwin-Philips-Terlevich (BPT) diagrams. They are, in the updated version, based on four optical line ratios: $\frac{[OIII]}{H_\beta}$, $\frac{[NII]}{H_\alpha}$, $\frac{[SII]}{H_\alpha}$ and $\frac{[OI]}{H_\alpha}$. They can be used to separate celestial objects according to the principal excitation mechanisms: e.g., star forming galaxies, Seyferts, LINERS, etc.

The origin of the FRI/FRII dichotomy is still unknown: external agents such as the interaction of the radio jet with the environment, see e.g. Bicknell [1995], the host galaxy, merging history, etc. or intrinsic factors like the accretion power of the AGN, see Ghisellini and Celotti [2001], have been invoked as possible explanations. On the contrary, the HERG/LERG classification reflects the accretion regime of the AGN central engine, since different excitation modes of the NLR are associated to different accretion rates [Gendre et al., 2013]. In particular, HERGs accrete efficiently (quasar-mode), i.e. the potential energy of the gas accreted by the SMBH is efficiently converted into radiation. Conversely, LERGs are characterized by low accretion rates, typical of radiatively inefficient hot accretion flows (jet-mode) where the jet represents the bulk of the AGN's energetic output [Heckman and Best, 2014]. This model is schematically represented in figure 1.9 and discussed in detail in the next Section.

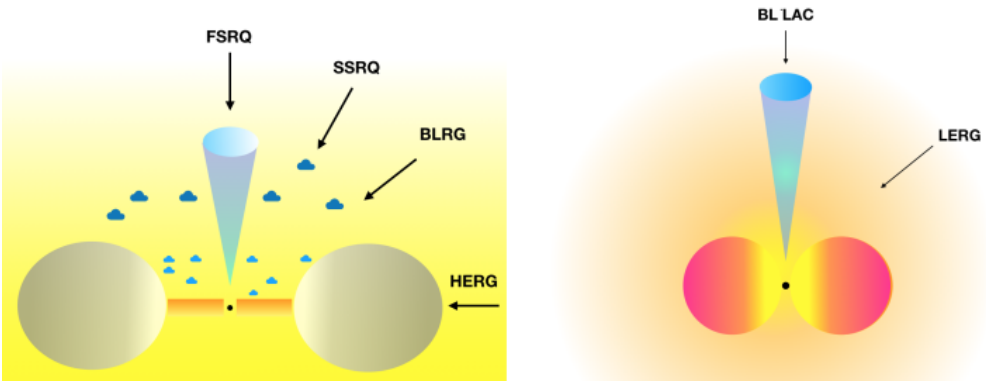

Figure 1.9: *Left panel:* Schematic view of an efficiently accreting RL AGN. It is possible to distinguish between BH, accretion disc, torus and jet. Ranging from 90° to 0°, the AGN behavior changes, passing from HERG to BLRG and then quasar. *Right panel:* Schematic view of an inefficiently accreting RL AGN. The accretion material structure turns into an almost spherical shape, forming an "Advection-dominated accretion flow" (ADAF) which will be discussed in the section 1.3. The LERG becomes a BL Lac moving from high to low jet inclination angles.

1.3 Radiative processes: accretion and ejection

1.3.1 Accretion

A common characteristic shared by all radio–loud AGNs is the presence of two competitive components: the disk and the jet, which are usually mixed when reaching the observer. Although in some cases one component dominates over the other one (e.g., in blazars the jet radiation is dominant), generally the resultant spectrum is a combination of both and the challenge is to distinguish between them.

Accretion is the physical process by which a black hole aggregates matter from its surroundings. The efficiency of accretion can be measured in terms of released luminosity:

$$L_{acc} = \eta \dot{M} c^2 \tag{1.4}$$

in which $\dot{M}$ is the accretion rate (in terms of $M_{\odot} yr^{-1}$) and η is the efficiency of the process ($\propto$M/R), where M and R are referred respectively to the accretor mass and radius.

The luminosity involved in the accretion increases by increasing the accretion rate. When the luminosity at which the outward force of the radiation pressure is balanced by the inward gravitational force, the Eddington luminosity is obtained:

$$L_E = \frac{4\pi G m_p c}{\sigma_T} M \tag{1.5}$$

where $G = 6.67 \times 10^{-8}$ cm^3 g^{-1} s^{-2} is the gravitational constant, $m_p = 1.67 \times 10^{-24}$ g is the proton mass and $\sigma_T = 6.65 \times 10^{-25}$ cm^2 is the Thomson scattering cross-section for the electron. For luminosity values greater than L_E, radiative pressure dominates over the gravitational force and matter is moved away from accretor. For this reason, the ratio between the accretion luminosity and the Eddington luminosity is considered an estimator of the accretion rate of a source.

Accretion processes involve rotating gas flow. The determination of the accretion flow structure is the solution of four equations, each of them being the conservation of a physical property:

1. *mass*
2. *energy*
3. *angular momentum*
4. *vertical momentum*

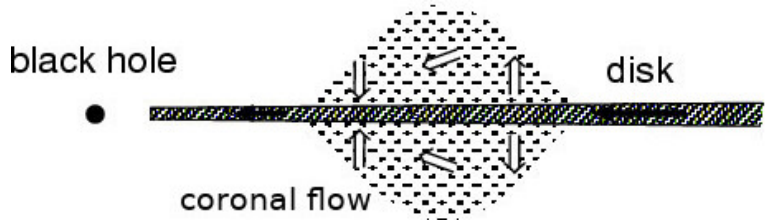

Figure 1.10: Schematic representation of Shakura and Sunyaev accretion disc (Credits: Meyer et al. 2007).

The most famous solutions are the Shakura & Sunyaev disk or the Advection-Dominated accretion flow (ADAF) model. In both cases viscosity acts as a source of heat that is radiated outward transporting angualr momentum away.

The Shakura & Sunyaev geometrically thin optically thick disk was proposed by Shakura and Sunyaev [1973] and it is schematically represented in Figure 1.10. In this model the disk is geometrically

thin and optically *thick*, since each element of the disk can be approximated as a blackbody (BB) emission. The effective temperature of the photosphere is:

$$T(r) \approx 6.3 \times 10^5 \left(\frac{\dot{M}}{\dot{M}_E}\right)^{1/4} M_8^{-1/4} \left(\frac{r}{R_S}\right)^{-3/4} [K] \tag{1.6}$$

where $\dot{M}$ is the effective mass accretion rate, $\dot{M}_E$ is the mass accretion rate at Eddington regime, M_8 is the BH mass in units of $10^8 M_\odot$ and R_S is the Schwarzschild radius. Therefore, the disc emission can be considered as a sum of BB, whose temperatures vary with radius. In a typical AGN (BH mass around $10^8 M_\odot$) the peak is located in the UV band (corresponding to the Big Blue Bump) and the disc effective temperature ranges from $\approx 10^4 K$ to $10^6 K$.

It is possible to define the Innermost Stable Circular Orbit (ISCO), whose value depends on BH spin with respect to disc rotation. In case of non-spinning BH, the gravitational field is expressed with the Schwarzschild metric, then r_{ISCO} is:

$$r_{ISCO} = 3R_S \tag{1.7}$$

in which $R_S = \frac{2GM}{c^2}$ is the Schwarzschild radius. The position of ISCO ranges from $0.5R_S$ (in case of maximally rotating BH) to $6R_S$ [Czerny and You, 2016] (in case of maximally counter-rotating BH).

This model assumption breaks down in radiatively inefficient cases.

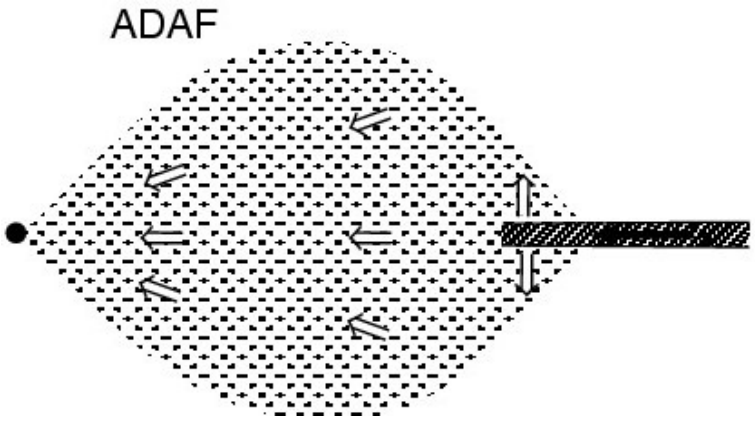

Figure 1.11: Schematic representation of the Advection-Dominated Accretion Flow (ADAF) model (Meyer et al. 2007).

One of the best models for radiatively inefficient accretion is Advection-Dominated Accretion Flow (ADAF; Narayan and Yi [1994], Abramowicz et al. [1995]) represented in Figure 1.11. This solution requires smaller accretion rates and angular momentum than the Shakura & Sunyaev disc. It involves a geometrically thick and optically thin structure since the material has a low density and is unable to efficiently cool down becoming a dense disc. The heat produced by viscosity is not efficiently emitted via radiation, but is stored in the gas until it falls onto BH. Ions and electrons are thermally de-coupled: close to the BH it was recognized the presence of a two-temperatures plasma, with a ion temperature of around $10^{12} \frac{R_S}{R}$ K and electron temperature ranging from 10^9 K to 10^{11} K.

1.3.2 Jets

Jets are giant plasma outflows through which the black hole transfers to the environment huge amount of energy, momentum and angular momentum at very large distances (kpc to Mpc). A key parameter in the study of relativistic jets is the Doppler factor. It relates the observed flux to intrinsic flux of a source, which is moving at a relativistic speed:

$$\delta = [\gamma(1 - \beta \cos\theta)]^{-1} \tag{1.8}$$

where $\beta = \frac{v}{c}$ is the ratio between object and light speed, γ is the Lorentz factor and can be expressed in terms of β ($\gamma = \frac{1}{\sqrt{1-\beta^2}}$). θ is the angle between the Line Of Sight (LOS) and the jet axis. The Doppler factor strongly depends on θ:

when $\theta = 0°$, then $\delta = \sqrt{\frac{1+\frac{v}{c}}{1-\frac{v}{c}}} = \delta_{max}$;

when $\theta = 90°$, then $\delta = \sqrt{1-(\frac{v}{c})^2} = \delta_{min}$.

Depending on the value of θ the observed flux can be either strongly amplified or de-amplified (see Figure 1.12).

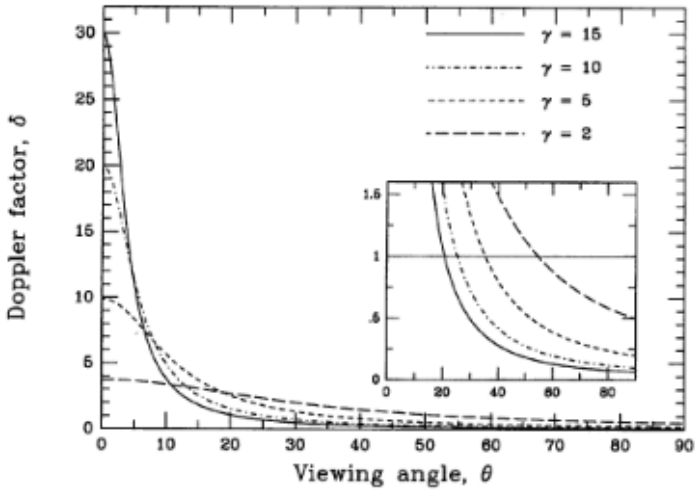

Figure 1.12: The dependence of the Doppler factor on the AGN orientation. Different curves correspond to different Lorentz factors, from $\gamma = 15$ (the solid line) to $\gamma = 2$ (the dashed one). The angles for which $\delta = 1$ are represented in the right inset. Credit: Urry and Padovani [1995].

Jets emit non–thermal radiation principally through synchrotron and Inverse Compton physical processes. Synchrotron radiation is produced by relativistic electrons spiraling in a magnetic field. There are different models to explain the presence of a magnetic field. One of these involves a hot and geometrically thick flow, which is thought to be present in both efficient or inefficient accretion modes (ADAF or coronal flow) in the proximity of the BH. The hot flow provides the

dragging and accumulation of the magnetic field close to the BH horizon. Strong magnetic fields are necessary to the jet formation but are not a sufficient condition. It is also necessary a source of energy to generate an outflow of relativistic particles [Czerny and You, 2016]. It is thought that two mechanisms are responsible:

1. the ram pressure, due to matter accumulated in the BH vicinity as a consequence of magnetic field dragging;

2. the extraction of rotational energy from the BH through a decay of particles. For this process strong magnetic field and high BH spin are required.

As for the synchrotron radiation, assuming a power law energy distribution of the electrons energies, the emissivity, i.e. the power per unit solid angle produced within 1 cm^3, can be formalized as:

$$\varepsilon_{sin}(\nu) \propto KB^{\alpha+1}\nu^{-\alpha} \text{ [erg cm}^{-3} \text{ s}^{-1} \text{ sr}^{-1}\text{]} \tag{1.9}$$

Inverse Compton (IC) generates when the electron energy is greater than the photon one, and a transfer of energy from the electron to the photon can occurs (Figure 1.16). There is a strong link between the scattered frequency ν_c and the electron energy producing it:

$$\nu_c = \frac{4}{3}\gamma^2\nu_0 \tag{1.10}$$

The IC emissivity (ε_c) can be deduced in the same way of the synchrotron emissivity (ε_{sin}) assuming a power law distribution for the relativistic electrons:

$$\varepsilon_c(\nu_c) \propto K\nu_c^{-\alpha} \int \frac{U_r(\nu)\nu^{\alpha}}{\nu} d\nu \text{ [erg cm}^{-3} \text{ s}^{-1} \text{ sr}^{-1}\text{]} \tag{1.11}$$

where $U_r(\nu)$ is the specific radiation energy density describing the upscattered photon field. When the same electrons producing synchrotron radiation are scattered, the resultant process is called Synchrotron–Self Compton (SSC), while when the scattered ($U_r\nu \propto \nu^{-\alpha}$) photons come from external regions like the disk or the BLR, the torus, the NLR, the process is called External Compton (EC). The Cosmic Microwave Background (CMB) can be also the seed photons for the IC in jets or lobes.

1.4 AGN Spectral Energy Distribution

The Spectral Energy Distribution (SED) of a source is fundamental to understand the emission processes in the whole electromagnetic spectrum. It is defined as the product between the flux density and the frequency as function of the frequency itself. An example of a typical AGN SED is shown in Figure 1.13.

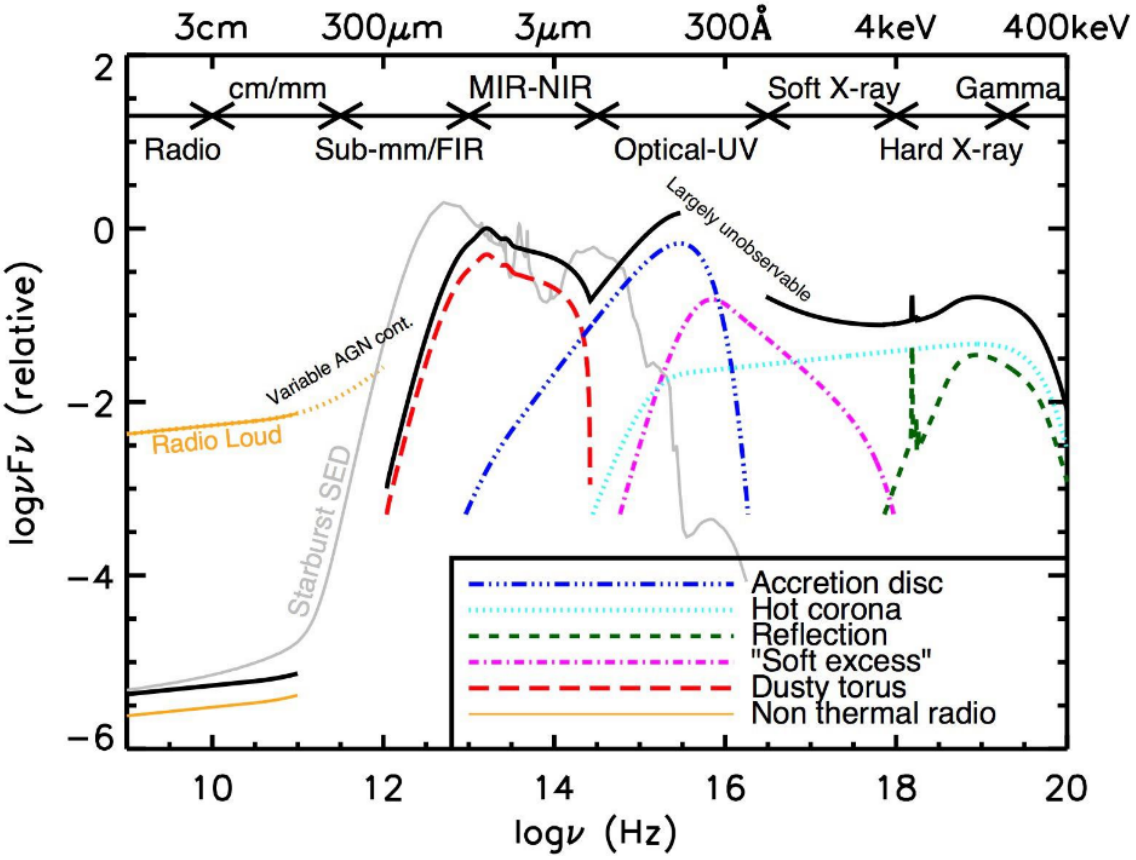

Figure 1.13: AGN Spectral Energy Distribution from radio to γ-rays band (Frequency (Hz) vs product of frequency and flux in logarithmic scale). Different colors represent different AGN components. The black line is the sum of all components. Credit: *Chandra* webpage.

The flux in the interval between ν_1 and ν_2 is defined as:

$$F = \int_{\nu_1}^{\nu_2} F_\nu d\nu = \int_{\nu_1}^{\nu_2} \nu F_\nu d(log\nu) \tag{1.12}$$

Therefore, the same areas under the SED curve correspond to the same energies.
Figure 1.14 shows the SED of AGN characterized by efficient and inefficient accretion regimes.
In a SED, every emission feature can be ascribed to a specific component (as listed in Section 1):

Radio: radio emission is produced through synchrotron radiation (Figure 1.15) by relativistic electrons spiraling around magnetic field lines. Electrons are accelerated from the continuous change in the direction of electrons motion, caused by the magnetic field. Therefore, according to Larmor formula, any charged particle accelerated radiates energy. The frequency of the single emission depends on the electron energy and magnetic field strength. The sum of the whole electron population shapes the radio spectrum.

Infrared: this emission is of thermal origin. The dust reprocesses radiation from the optical/UV bands and partially re-emits it in the IR band. The effect of dust grains on incoming radiation is double: absorption and scattering. The combination of these two effects can be

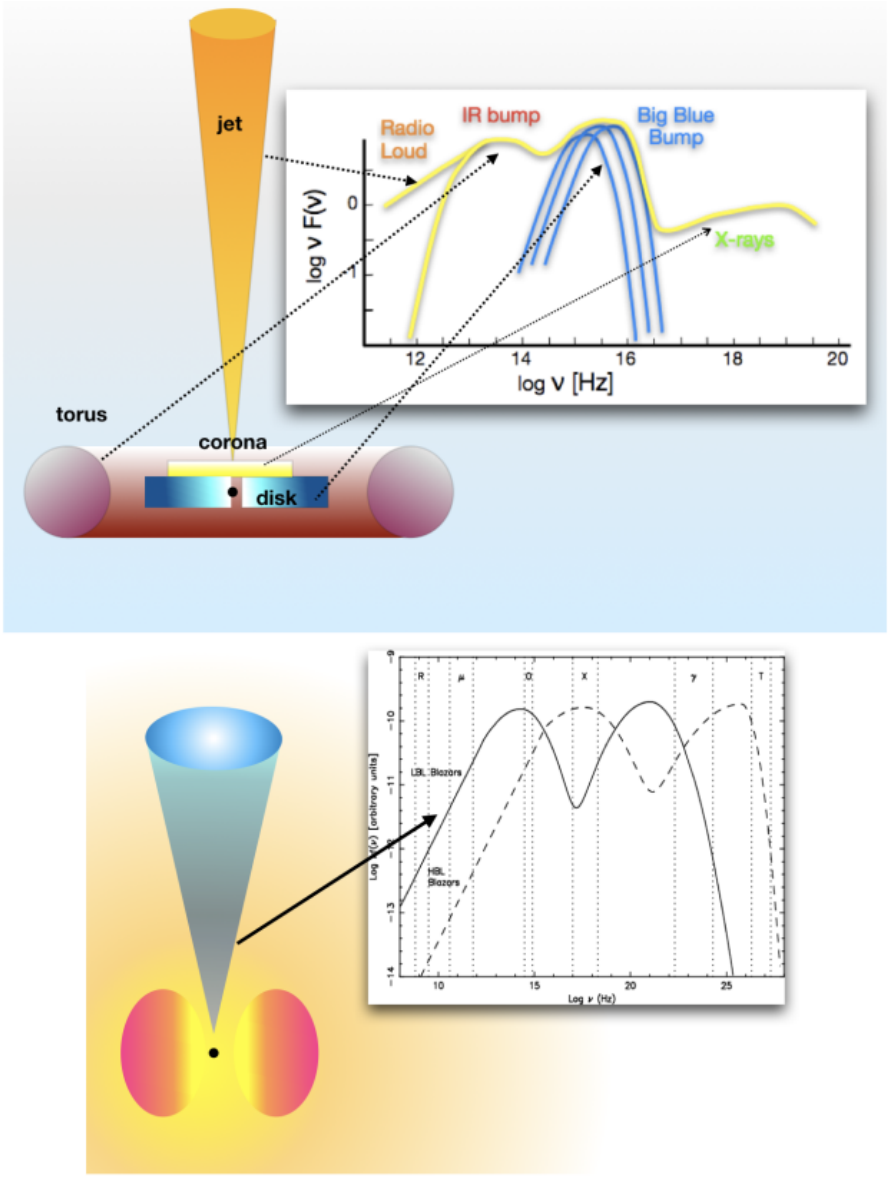

Figure 1.14: *Upper panel*: Type 1 AGN SED. Each spectral range is related to an AGN emission region. The radio flux is due to the jet, the infrared bump is due to the dusty torus that reprocesses the accretion disk photons, the blue bump is due to accretion disk and the power law in the X-ray range is due to the corona of hot electrons above the disc. *Bottom panel:* BL Lac SED with the typical double peak due to non-thermal jet emission. The radiation due to the accretion flow is negligible compared to the jet radiation. The position of the peaks is different between BL Lacs and FSRQ: the synchrotron peak in FSRQ is generally located in the IR band, while BL Lacs sources can reach optical-UV bands. Fossati et al. [1998].

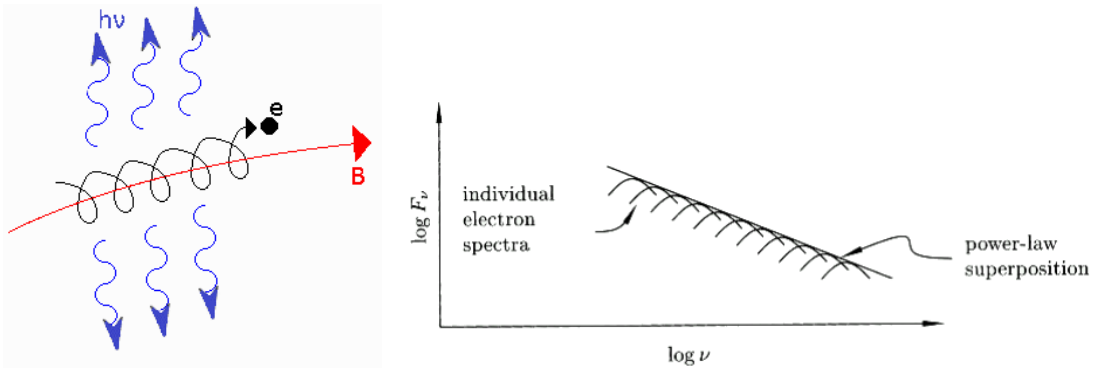

Figure 1.15: On the left panel: schematic representation of the single synchrotron emission. The magnetic field line is in red, the electron spiraling around them in black and the emitted photons in blue. On the right panel: superposition of individual synchrotron emissions which shape the power-law spectrum.

summarized in a phenomenon called *dust extinction*. For what concerns the absorption, a dust grain can be considered as a "grey" body that partially re-emits the absorbed radiation increasing its own temperature.

Optical/UV: it is composed by a combination of emission lines and continuous emission. The first are emitted in the BLR and NLR, illuminated by radiation coming from the central engine. Instead, the accretion disc is responsible for the continuum emission that can be assumed as the overlap of blackbody spectra (Multiple Black Body emission).

X-rays: this band is fundamental to investigate the innermost regions of an AGN. The X-ray energy ranges between $\approx$ 0.1-200 keV consisting of about 10% of the AGN bolometric emission (see Figure 1.16).

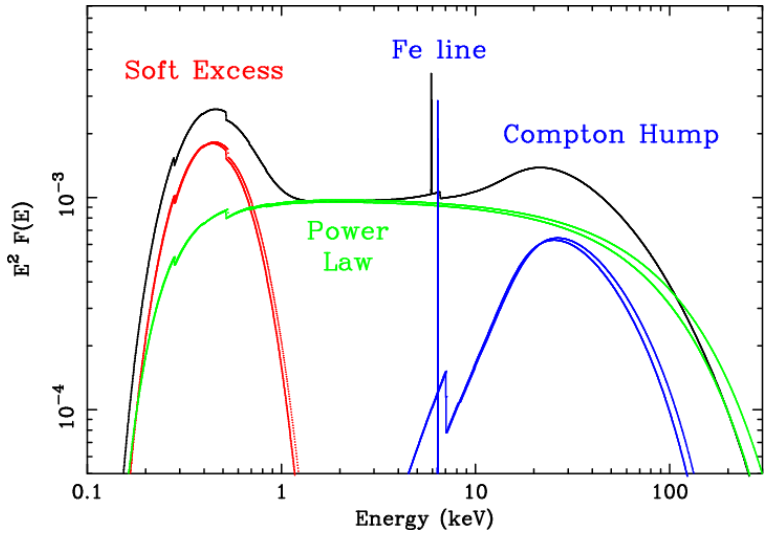

Figure 1.16: A typical X-ray emission of a type 1 (unobscured) AGN. Different features are emphasized by different colors. The sum of the emissions is represented by the black line (credit: Jovanović and Popović [2009]).

.

The primary emission is due to thermal Comptonization of the optical/UV photons, coming from the accretion disc, by the hot corona electrons ($T \approx 10^9 K$). The corona is composed by highly energetic thermal electrons and is located very close to the accretion disc. The energy distribution of the photons is described by a power-law:

$$N(E) = N_0 E^{-\Gamma} \tag{1.13}$$

where Γ is the photon index, defined as $\alpha + 1$ (with $\alpha = -\frac{\ln \tau}{\ln A}$ being the spectral index, τ the optical width, $A = e^y$ the mean energy gained from photons for single scattering and $y = \frac{4kT}{m_e c^2}\tau$ the Compton y-parameter). The power law is the overlap of many orders of scattering events, which can be single or multiple (the same photons can be scattered many times by coronal electrons). So, the spectrum is influenced by both accretion disc and hot corona properties. Photons can be upscattered until their energy equals the electron energy. In fact, as photons approach the electron thermal energy, their gain is gradually reduced, until becoming null when $E_{photon} \approx E_{electrons}$. This produces a cut-off in the power law spectrum, which gives information about the coronal temperature: $E_c \approx kT$. The resulting spectrum is:

$$F_E \propto E^{-\Gamma(kT,\tau)} \exp(-\frac{E}{E_c(kT,\tau)}) \tag{1.14}$$

In addition to the power-law continuum the spectrum of an AGN can present features such as:

1. **Soft excess:** its origin is still debated. Named after the extrapolation of the soft X-ray band to the hard X-ray band for various sources. The emission observed had always lower values with respect to the extrapolated one. The two main possibilities are: an extension of Big Blue Bump (BBB) at higher energy or a colder region of the corona. The temperature which well represents the soft excess is always the same, independently from BH mass. This suggests a different nature than BBB Fabian and Miniutti [2005];

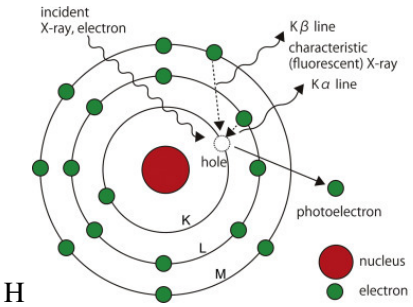

Figure 1.17: Sketch of Fe $K\alpha$ line emission mechanism. The green points are electrons orbiting around the nucleus (the red point)

.

2. **Warm absorber:** absorption feature observed below 2 keV. It is due to ionized gas observed in absorption ($T \approx 10^{4-5} K$). It is typically outflowing at velocities around hundreds or few thousands km s^{-1};

3. **Fe $K\alpha$ line:** it is produced by fluorescence effects in either the disc or torus (or both).

   The process starts with photo-ionization ($E > 7.1 keV$) of an electron from the K-shell of an iron atom, which becomes excited. Then another electron, from either the L or M shell, drops into K-shell, in order to reach a lower atomic energy state. If the electron comes from the L-shell, a photon with energy 6.4 keV will be emitted (producing the $K\alpha$ line). This mechanism is summarized in figure 1.17. If the electron comes from the M-shell, then the photon will have 7.05 keV (producing $K\beta$ line). When the $K\alpha$ line is produced very close to the central BH, it is shaped by both Doppler and gravitational effects. The $K\alpha$ EW, in type 2 AGN, is a fundamental to estimate intrinsic absorption [Ghisellini et al., 1994]. In fact, in heavily obscured sources ($N_H > 10^{24}\ cm^{-2}$) there is a prominent iron $K\alpha$ emission line with EW of about $1-3$ keV; while for $N_H < 10^{23}\ cm^{-2}$, EW values typical of type I AGN are observed [Risaliti and Elvis, 2004].

4. **Compton hump:** Comptonization between disc photons and Hot Corona electrons produces photons isotropically from corona. About half of them bump again into disc and can be reflected by Compton scattering, creating a hump between 20 and 50 keV on spectral emission.

Obscuration affects the X-ray spectrum by photoelectric absorption and Compton scattering. These effects can work simultaneously but in different bands. In fact, the former operates typically at energies lower than 10 keV and the latter at higher energies. The Compton scattering reduces the photon energy which, below a certain threshold, can be absorbed by metals via photoelectric effect. The result of this combined action is: as N_H (hydrogen column density[3]) and metallicity increase, than the spectrum is absorbed at higher energies. It is possible to distinguish absorbed AGN, according to the measured column density:

1. $N_H < 10^{21}$ cm^{-2}: unabsorbed;

[3]Metals are the main actors of this phenomenon but, since hydrogen is the most common element in the Universe, the absorption is reported in hydrogen-equivalent units assuming a given abundance.

2. $10^{21} < N_H < 10^{24}$ cm^{-2}: Compton thin;
3. $10^{24} < N_H < 10^{25}$ cm^{-2}: mildly Compton thick;
4. $N_H > 10^{25}$ cm^{-2}: heavily Compton thick.

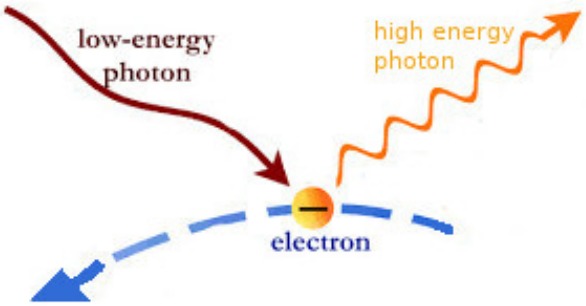

Figure 1.18: Sketch of an Inverse Compton (IC) scattering. The low photon hits again the relativistic electron and then, a high-energy photon is emitted.

γ-rays: photons have energies E>100 MeV. In this regime non–thermal processes dominate and it is possible to study the behaviour of some of the most energetic and extreme objects in the Universe. Several important mechanisms can produce γ-rays in astrophysical objects. Among them there is the IC scattering (1.18) and the Synchrotron-Self Compton (SSC). In both cases the photons are scattered to high energy by relativistic electrons, but the difference is in the nature of the seed photons. The seed photons of SSC are produced in the same region of scattering by the relativistic electrons themselves, via synchrotron emission. In case of single scattering, the final frequency of scattered photon is: $\nu_f \propto \gamma^2 \nu_i$, in which γ is the Lorentz factor: $\gamma = \sqrt{1-\beta^2}$, with $\beta = \frac{v}{c}$.

Chapter 2

X-ray telescopes

2.1 The *Chandra* X-ray observatory

X-ray photons are sufficiently energetic to go across every kind of material. The only mechanism that allows to reflect high-energy radiation and reconstruct an image on a focal plane, is the grazing-incidence reflection. The high-energy photons are reflected when their incidence angle with respect to the mirror plane (θ) is lower than a critical angle (θ_{crit}). It is defined as: $\theta_{crit} \propto \frac{\sqrt{\rho}}{E}$, where ρ is the density of the reflecting mirror and E is the energy of incoming photon. From the last definition it is easy to understand that, once determined the mirror density ρ, θ_{crit} and then the number of photons reflected (i.e. those with angle of incidence $0 < \theta < \theta_{crit}$) decreases with the increasing energy.
Since the telescope must be mounted in a spacecraft and must be part of an orbiting station, two grazing-incidence mirrors are generally coupled, in order to reduce the telescope focal length. The most used grazing-incidence optics are the *Wolter* configurations, which are shown in figure 2.1.

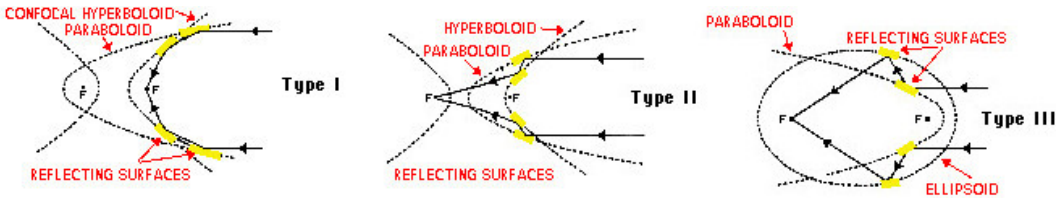

Figure 2.1: Wolter telescope configurations, respectively type 1, 2 and 3. The figure is taken from: "The *Chandra* Proposers' Observatory Guide".

In particular, the most used is the Wolter type 1.

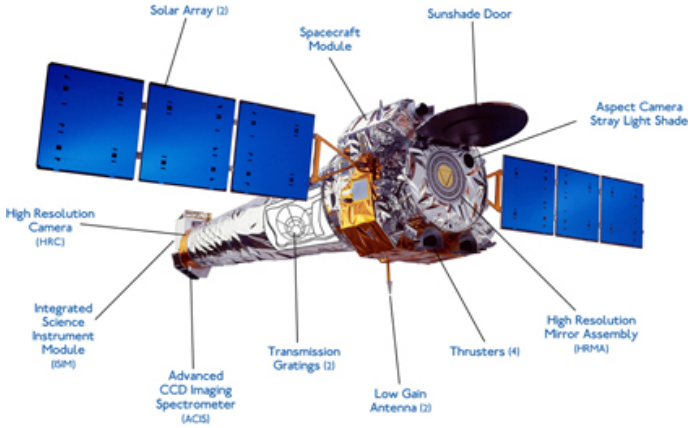

Figure 2.2: Schematic view of *Chandra* satellite (figure from: "The *Chandra* Proposers' Observatory Guide".

The *Chandra* satellite (Fig. 2.2) was launched in 1999 by NASA. Onboard there is a single focusing telescope Wolter 1 type, consisting of 4 paraboloid mirror shells associated to 4 hyperboloid ones, as shown in figure 2.3.

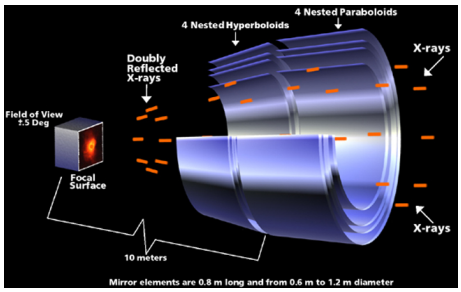

Figure 2.3: Reconstruction of *Chandra* grazing-incidence optic. X-rays are reflected by paraboloid and hyperboloid shells and then are directed to the focal surface. The figure is taken from: "The *Chandra* Proposers' Observatory Guide".

Its four couples of mirrors were built to ensure the best angular resolution ever in the X-ray band. The structure composed by the mirrors is called High Resolution Mirror Assembly (HRMA). Its properties are:

Mirror coating	Iridium
Mirror outer diameters	0.65 m 0.87 m 0.99 m 1.23 m
Unobscured aperture	1145 cm^2
HRMA mass	1484 kg

The mirrors direct photons to four instruments, which work one at a time (conversely, XMM-*Newton* focal-plane instruments can work simultaneously, see next section):

- The HRC (*High Resolution Camera*) is composed by two Micro-Channel Plates (MCP) and produces images in the range of 0.1-10 keV, with a time resolution of 16 microseconds. Every MCP contains 69 million tiny tubes. When an X-ray strikes a tube, electrons are released and accelerated down the tube thanks to a high voltage. Then, a grid of wires, which is located at the end of tubes and is able to measure the electron signal, allows to determine the X-ray incoming position with high precision.

- The ACIS (*Advanced CCD Imaging Spectrometer*) consists of 10 CCDs and can be used both for imaging and for spectral extraction (since it measures also the energy of each incoming photon), in the range of 0.2-10 keV. Every CCD has a 1024×1024 pixels. The Point Spread Function (PSF), which measures the distribution on the detector of photons coming from a point-like source, has a FWHM on-axis of about $0.5''$. There are two possible configurations, as shown in figure 2.4

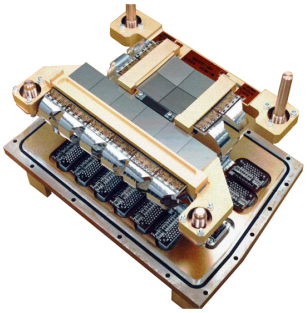

Figure 2.4: View of ACIS. At the top the four ACIS-I CCDs, at the bottom the six of ACIS-S configuration (figure from: "The *Chandra* Proposers' Observatory Guide".

  1. ACIS-I: a 2×2 array of 4 CCDs (called: I0, I1, I2, I3)
  2. ACIS-S: a 1×6 array of 6 CCDs (called: S0, S1, S2, S3, S4, S5)

  Every CCD covers a fraction of sky of $8.4' \times 8.4'$ and is front-illuminated (except for S1 and S3 that are back-illuminated). In general ACIS-S configuration is preferred for single objects, while ACIS-I is preferred for surveys. This is because the ACIS-I configuration guarantees a larger field of view with a good angular resolution.

- The LETG (*Low Energy Transmission Grating*) Spectrometer array, a single line grating, working on 0.08-2 keV range.

- The HETG (*High Energy Transmission Grating*) Spectrometer array, working on 0.4-10 keV range.

Since ACIS data allow to obtain a good counts statistics and a moderate-resolution spectroscopic analysis (with an energy resolution of about 90 eV at 1.49 keV), this detector is the most suitable instrument for the study described in my Master thesis. In the next section ACIS-I and ACIS-S will be explained in more details.

2.1.1 ACIS main properties

The HRMA-ACIS combination (exactly like any other telescope-detector coupling) has a specific capability to collect photons, defined as *Effective Area* (Fig. 2.5):

$$A_{eff}(E,\theta,x,y) = A_{geometric} \times R(E) \times V(E,\theta) \times QE(E,x,y) \tag{2.1}$$

where:

$\boldsymbol{A_{geometric}}$ (geometric area) is the telescope collecting area;

$\boldsymbol{R(E)}$ (reflectivity) is the capability of the mirrors to reflect photons;

$\boldsymbol{V(E,\theta)}$ (vignetting) is defined as the ratio between off-axis and on-axis effective area. The photons loss increases with angular distance with respect to the optical axis and with increasing energy. In the left panel of figure 2.6 this effect is showed;

$\boldsymbol{QE(E,x,y)}$ (quantum efficiency) represents the fraction of photons counted by the detector with respect to the incidents ones. The peak of QE for ACIS CCDs, as we can see in the right panel of figure 2.6, is about 4 keV for Back-illuminated CCDs and 5 keV for Front-Illuminated ones. In fact, the BI CCDs have a higher sensitivity to lower energies.

The nominal on-axis effective area of the FI CCDs at 1.5 keV, integrated over the PSF to >99 % encircled energy, is 600 cm^2. Actually, this value belongs to several cycles ago, since a deterioration occurred over the last years. In fact, to date, especially in the soft-X-ray band (E<2 keV), the EA is substantially reduced (see: `http://cxc.harvard.edu/ciao/why/acisqecontamN0011.html`).

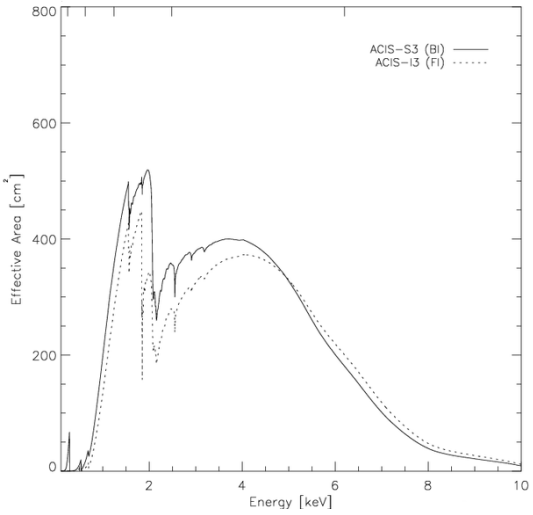

Figure 2.5: *Chandra* Effective Area versus energy. The solid line is for Back-Illuminated S3 CCD, and the dashed line for Front-Illuminated I3 CCD (figure from: "The *Chandra* Proposers' Observatory Guide".

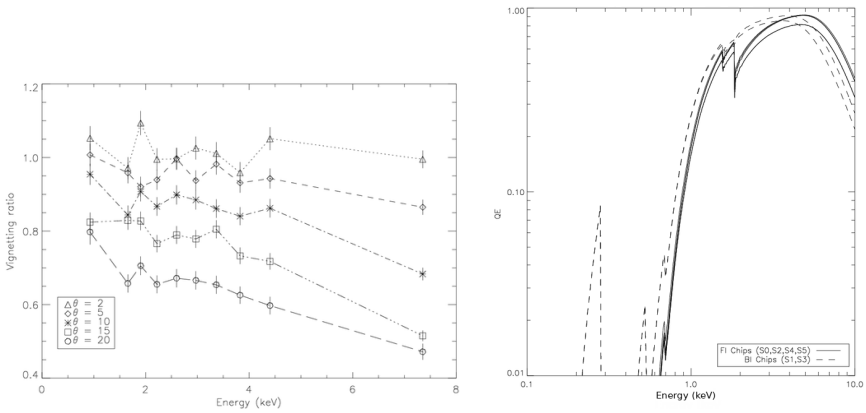

Figure 2.6: Left panel: effect of vignetting in *Chandra*, as a function of energy, for different off-axis angles in arcmin. Right panel: QE of ACIS CCDs as a function of energy; the solid line refers to Front-Illuminated CCDs and the dashed line to Back-Illuminated ones (figure from: "The *Chandra* Proposers' Observatory Guide".

At last, for what concerns the ACIS spatial resolution, it is useful to introduce the Encircled Energy Fraction distribution (EEF). This is defined as the two-dimensional integral of the PSF. The EEF is a function of energy and angular distance from the optical axis. The EEF is the fraction of energy (i.e., photons) comprised within a certain radius with respect to the total amount of signal from a point-like source. The on-axis *Chandra* EEF at different energy is shown in figure A.7. To reach the same level of EEF, if energy increases, it is necessary a larger radius: as we can see in figure 2.7, $EEF = 0.8$ is reached within 0.6 arcsec for $E = 1.5$ keV and within 1 arcsec at $E = 6.4$ keV. At fixed energy, as the angle with respect to the optical axes increases, the EEF becomes lower than the on-axis one.

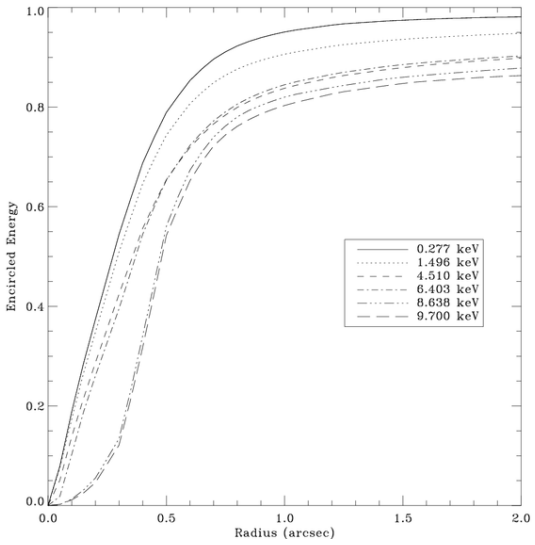

Figure 2.7: *Chandra* on-axis EEF of a point-like source at several energies: from 0.277 keV to 9.7 keV (respectively from the top to the bottom line). The figure is taken from: "The *Chandra* Proposers' Observatory Guide".

The ACIS energy resolution, as shown in figure 2.8, has a strongly dependence on energy: for Front-Illuminates CCDs, for example, it spans from 80 eV of FWHM at 1 keV to about 140 eV at 6.5 keV. It also weakly depends on pixel position in the array.

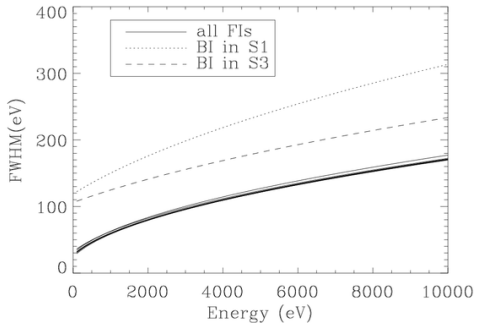

Figure 2.8: Energy resolution in terms of FWHM for front-illuminated (FI) and back-illuminated (BI) CCDs. The solid lines represent all the FI CCDs, the dashed and dotted lines represent the BI CCDs S3 and S1 respectively (figure from: "The *Chandra* Proposers' Observatory Guide".

2.2 The XMM-*Newton* observatory

The XMM-*Newton* satellite (Fig. 2.9) was launched in 1999 by ESA.

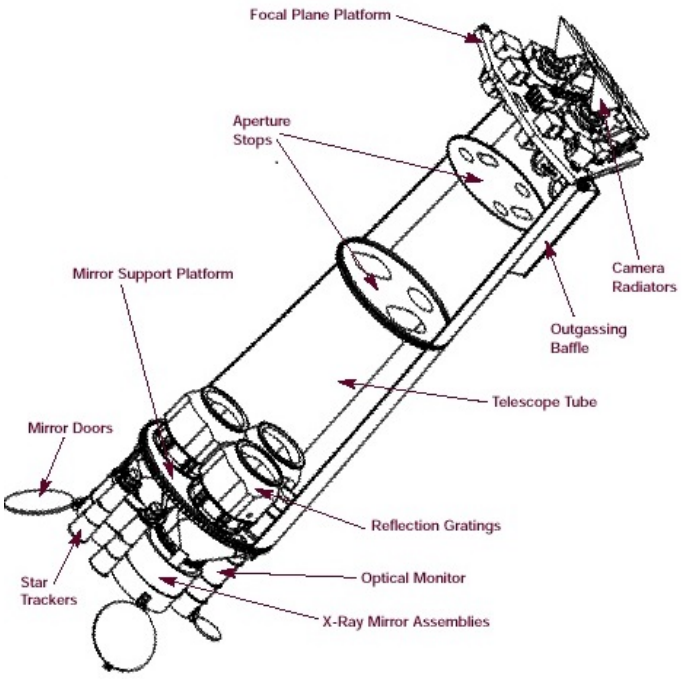

Figure 2.9: Schematic reconstruction of the XMM-*Newton* satellite (figure from: "XMM-*Newton* Users Handbook".

It carries three Wolter 1 X-ray telescopes, each of these with 58 mirror shells. The large

number of shells guarantees the primacy to XMM-*Newton* in terms of Effective Area. In fact, with 4650 cm^2 at 1.5 keV and 3000 cm^2 at 6 keV, it has the highest values ever in the X-ray band below 10 keV, for what concerns satellites with focusing optics. It is characterized by a PSF with a FWHM of about $6''$. Another relevant fact is that the 6 scientific instruments, mounted on XMM-*Newton* satellite can work simultaneously. They are:

- The EPIC (European Photon Imaging Cameras) composed of three CCD cameras at the foci of the three telescopes: one pn camera and two MOS (Metal Oxide Semiconductor).
- The RGS (Reflection Grating Spectrometers), two spectrometers which direct the photons in a secondary focus (about 60% of the incoming photons go to the primary focus where there are the MOS and 40% to the secondary thanks to dispersion gratings), shown in figure 2.10. They are used for high resolution X-ray spectroscopy in 0.33-2.5 keV band.

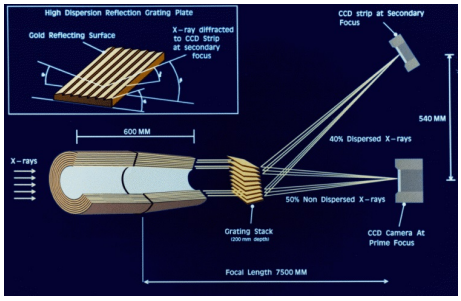

Figure 2.10: Schematic view of the photons optical path. About 60 % of them are sent to the MOS detectors, while the rest to RGS. (figure from: "XMM-*Newton* Users Handbook".

- The OM (Optical Monitor), which is an optical/UV telescope with an aperture of about 30 cm

INSTRUMENT	**EPIC pn**	**EPIC MOS**	**RGS**	**OM**
FOV	30'	30'	5'	17'
Bandwidth	0.15-15 keV	0.15-12 keV	0.35-2.5 keV	180-600 nm
Spectral resolution	80 eV (at 1 keV)	70 eV (at 1 keV)	3.2 eV (at 1 keV)	$\frac{\lambda}{\Delta\lambda} \approx 180$ (UV/optical grism)

Since it offers the highest effective area, the EPIC pn detector is the most suitable instrument for the kind of analysis carried out in this thesis project.

2.2.1 EPIC pn camera

There are not spectrometers in the pn line of sight, then it receives the entire signal. This allows EPIC pn to have the highest effective area among XMM-*Newton* instruments, as shown in figure 2.11.

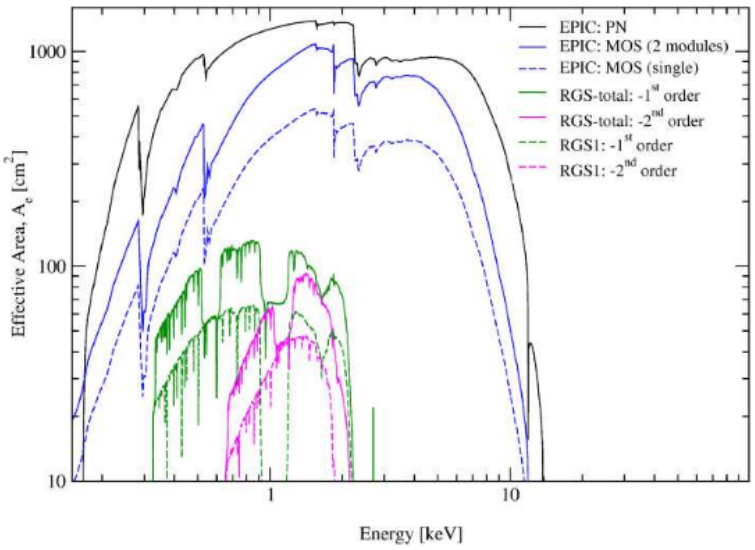

Figure 2.11: Comparison between the effective areas of instruments on board of XMM-*Newton*. The black line represents the EPIC pn Effective Area, while EPIC MOS are represented by blue lines: solid line for the combination of both modules and dashed line for a single MOS.

The pn detector is composed of 12 CCDs, arranged as shown in the left panel of figure 2.12, which can acquire data in different modes as function of the readout time (in which the detector acquires the charges) and FoV:

- *full frame:* all pixels are read, full FoV coverage;
- *partial window:* which is divided into large (half FoV is read) and small (only a CCD part is read);
- *timing:* an arbitrary area of the image is collapsed into a row, so the two-dimensions information becomes one-dimension.

When two or more photons falls into the same pixel in the same reading cycle then the *pile-up* phenomenon occurs. The result is that the detector measures the incoming photons as a single photon with higher energy (being the sum of the energies of the two or more original photons). The loss of information about the incoming photons makes the resulting spectrum compromised. This happens frequently for bright sources and can be avoided or reduced by reducing the readout time, using the *partial window* reading mode.

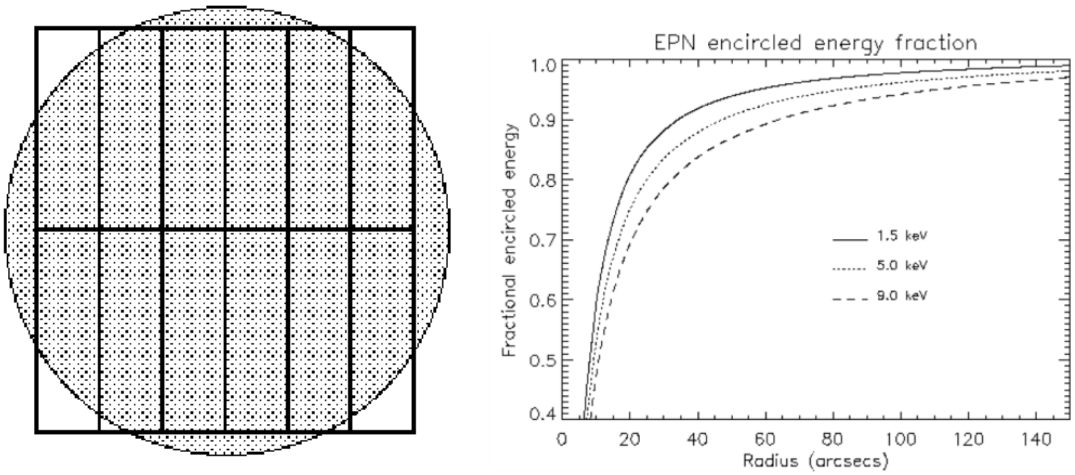

Figure 2.12: EPIC pn properties. On the left panel: EPIC pn FoV and CCDs arrangement. Twelve 3×1 *cm* CCDs, six per row, creating an imaging area of 6×6 *cm*, about 97 % of the FOV. On the right panel: pn encircled energy fraction at different energies as a function of the radius (in arcsecs units). Credit: "XMM-*Newton* Users Handbook".

Chapter 3

The X-ray analyzed 3CR sample

3.1 The 3CR sample: an overview

The 3CR catalog is one of the best studied samples of radio galaxies in the northern sky, thus a large amount of information is available in the whole electromagnetic spectrum. It was built up by Bennett in 1962 and consists of all sources with a flux density higher than 9 Jy at a frequency of 178 MHz and declination higher than -5°. It includes 328 sources and represents a revision of the Third Cambridge Catalog (3C) [Edge et al., 1959]. Some of the 3C sources was excluded, having a flux density lower than the 9 Jy-threshold, while others, blended in the original catalog, were resolved and added to the 3CR catalog, with a decimal extension. Successively, Spinrad et al. [1985] identified 298 optical counterpart and measured the redshifts for 269 of them. The sample covers the range $0 < z \leq 2.5$ in redshift, spanning between 8-24 in visual magnitude and between $10^{30.5}$-10^{37} erg s^{-1} Hz^{-1} in radio luminosity @ 178 MHz. Over the years, the 3CR sample has been studied by almost all the ground-based and space facilities operating from radio to γ-rays.

3.2 The X-ray sample

A complete subsample of 113 3CR sources at $z < 0.3$ is studied in this thesis. The selected objects span four orders of magnitude in radio luminosity (see figure 3.1). Buttiglione and collaborators classified them both in the optical and radio bands. The optical classification was based on the Excitation Index (EI) (see section 1.1.1). In the radio band, the sources were classified based on the morphological properties in FRII (when clear hot-spots were visible in the radio map) and FRI (when well defined twin-jets were visible). The sources with a specific classification in both radio and optical bands are 79, divided as follows: **30 FRII-HERG, 19 FRII-LERG, 17 FRII-BLRG**[1] and **13 FRI-LERG**. For these objects, X-ray observations from *Chandra* and/or XMM-*Newton* satellites were available in the public archives. These telescopes are the most appropriate to pursue this kind of study, since they provide high-quality images and spectra, thanks to the high-angular resolution and large effective area, respectively (see Section 2.1 and 2.2). Both telescopes operate in the $\sim$0.3-10 keV band, the most suitable to estimate the intrinsic absorption in unabsorbed ($N_H < 10^{21}$ cm^{-2}), Compton thin ($10^{21} < N_H < 10^{24}$ cm^{-2}) and mildly Compton

[1]These sources have EI values comparable to HERG, as shown in figure 1.8, therefore, they can be considered members of the HERG class from the point of view of the NLR emission.

thick ($10^{24} < N_H < 10^{25}$ cm^{-2}) AGN, as explained in Section 1.4.

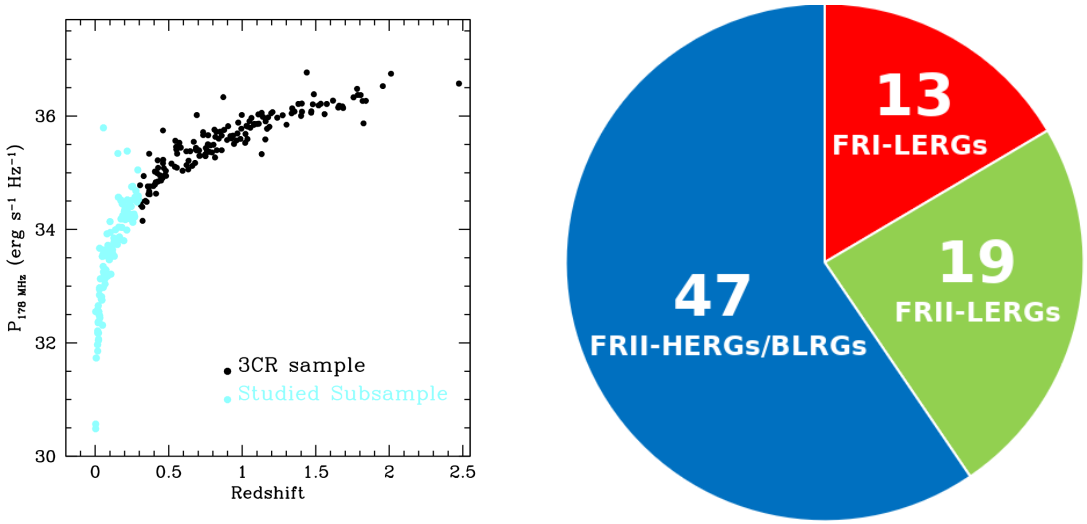

Figure 3.1: Classification of the sample presented in this work. *Left panel*: Redshift distribution vs radio power ($P_{178\ MHz}$) of the 3CR sample. My subsample is in cyan. *Right panel*: distribution of the 79 sources of the sample in different subclasses: 13 FRI-LERGs, 19 FRII-LERGs and 47 FRII-HERGs/BLRGs.

.

This sample is listed in table 3.1. For each source, the redshift, radio classification, optical classification and [OIII] luminosity (the most important diagnostic of NLR high excitation) are reported.

Table 3.1: Radio and optical classified Sources

Name	z	radio class	optical class	$L_{[OIII]}$	$P_{178\ MHz}$
3C17	0.2198	2	BLRG	41.99	34.44
3C18	0.188	2	BLRG	42.55	34.27
3C20	0.174	2	HERG	41.54	34.55
3C29	0.0448	1	LERG	40.09	32.84
3C31	0.0167	1	LERG	39.46	32.01
3C33	0.0596	2	HERG	42.18	33.65
3C33.1	0.1809	2	BLRG	42.30	34.07
3C40	0.0185	1	LERG	39.22	32.29
3C61.1	0.184	2	HERG	42.47	34.47
3C66B	0.0215	1	LERG	40.05	32.4
3C78	0.0286	1	LERG	39.41	32.51
3C79	0.2559	2	HERG	42.86	34.78
3C88	0.0302	2	LERG	40.14	32.49
3C98	0.0304	2	HERG	41.00	32.99
3C105	0.089	2	HERG	41.45	33.54
3C111	0.0485	2	BLRG	42.44	33.54
3C132	0.214	2	LERG	41.46	34.25
3C133	0.2775	2	HERG	42.76	34.72
3C135	0.1253	2	HERG	42.05	33.84
3C136.1	0.064	2	HERG	41.44	33.13
3C153	0.2769	2	LERG	41.63	34.56
3C165	0.2957	2	LERG	41.67	34.57
3C166	0.2449	2	LERG	41.66	34.42
3C171	0.2384	2	HERG	42.89	34.51
3C173.1	0.2921	2	LERG	40.85	34.61
3C180	0.22	2	HERG	42.34	34.32
3C184.1	0.1182	2	BLRG	42.23	33.66
3C192	0.0598	2	HERG	41.34	33.25
3C196.1	0.198	2	LERG	41.52	34.31
3C197.1	0.1301	2	BLRG	40.92	33.55
3C213.1	0.194	2	LERG	41.06	33.84
3C219	0.1744	2	BLRG	41.77	34.53
3C223	0.1368	2	HERG	42.17	33.85
3C223.1	0.107	2	HERG	41.58	33.23
3C227	0.0861	2	BLRG	41.75	33.74
3C234	0.1848	2	HERG	43.11	34.47
3C236	0.1005	2	LERG	40.89	33.56
3C264	0.0217	1	LERG	39.20	32.43
3C270	0.0075	1	LERG	38.96	31.79
3C272.1	0.0035	1	LERG	38.2	30.72
3C274	0.0044	1	LERG	38.99	32.63
3C277.3	0.0857	2	HERG	40.94	33.21
3C284	0.2394	2	HERG	41.59	34.28
3C285	0.0794	2	HERG	40.55	33.23
3C287.1	0.2159	2	BLRG	41.73	34.04
3C288	0.246	2	LERG	40.65	34.53
3C296	0.024	1	LERG	39.78	32.22
3C300	0.27	2	HERG	42.01	34.6
3C303	0.141	2	BLRG	41.74	33.77
3C303.1	0.267	2	HERG	42.42	34.25
3C305	0.0416	2	HERG	41.03	32.79
3C310	0.0535	2	LERG	40.05	33.56
3C321	0.096	2	HERG	40.91	33.49
3C323.1	0.264	2	BLRG	42.80	34.31
3C326	0.0895	2	LERG	40.40	33.60
3C327	0.1041	2	HERG	42.24	33.98
3C332	0.1517	2	BLRG	41.81	33.77
3C338	0.0303	1	LERG	39.57	32.99
3C349	0.205	2	LERG	41.69	34.2
3C353	0.0304	2	LERG	40.14	33.69
3C357	0.1662	2	LERG	40.95	33.86
3C379.1	0.256	2	HERG	41.86	34.16
3C381	0.1605	2	HERG	42.37	34.06
3C382	0.0578	2	BLRG	41.78	33.19
3C388	0.091	2	LERG	40.7	33.7
3C390.3	0.0561	2	BLRG	42.08	33.54
3C401	0.201	2	LERG	41.05	34.38
3C403	0.059	2	HERG	41.75	33.16
3C410	0.249	2	BLRG	42.02	34.8
3C430	0.0541	2	LERG	40.33	33.36
3C436	0.2145	2	HERG	41.56	34.37
3C445	0.0562	2	BLRG	42.50	33.26
3C449	0.0171	1	LERG	39.19	31.87
3C452	0.0811	2	HERG	41.34	33.94
3C456	0.233	2	HERG	42.81	34.23
3C458	0.289	2	HERG	42.03	34.58
3C459	0.2199	2	BLRG	42.03	34.55
3C460	0.268	2	LERG	41.78	34.25
3C465	0.0303	1	LERG	39.81	32.89

Column description: 3CR name; redshift from Spinrad et al. [1985]; morphological radio classification in FRI and FRII; spectroscopic classification in High Excitation Radio Galaxies (HERG), Low Excitation Radio Galaxies (LERG) and Broad Line Radio Galaxies (BLRG); logarithm of [OIII] λ5007 luminosity in units [erg s^{-1}] from Buttiglione et al. [2009]; logarithm of radio power @ 178 MHz in units [erg s^{-1} Hz^{-1}]. The typical errors on the [OIII] lines are a few percent of the reported value; throughout this work, the cosmological values adopted are: $H_0 = 71$ km s^{-1} Mpc^{-1}, $\Lambda_\Omega = 0.73$, $\Lambda_m = 0.27$.

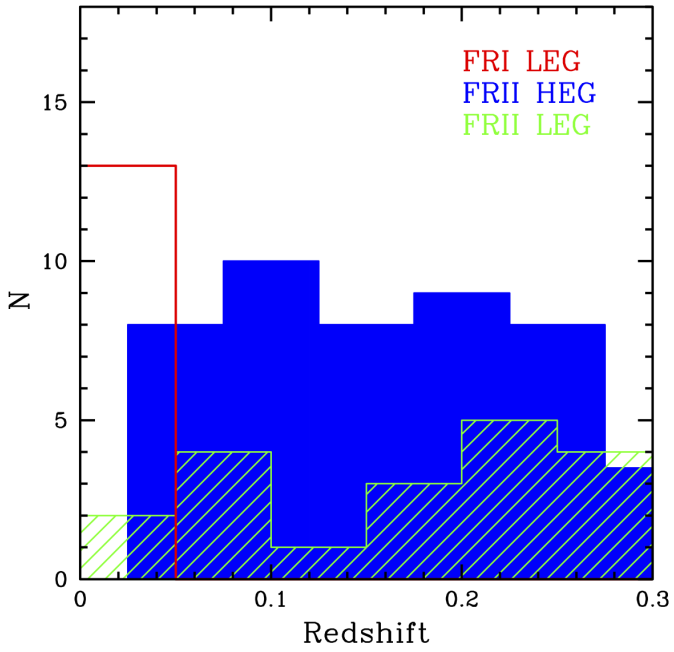

Figure 3.2: Distribution in redshift of the sample: the FRII-HERG/BLRG are in blue, FRII-LERG are in green and FRI-LERG are in red.

.

From the radio point of view, the majority of the sources are powerful FRIIs (76). FRIs (13) represent a small fraction of the total ($\sim$ 16%). However, if only the local Universe is considered, FRIs are the dominant population. No FRIs can be found at z>0.05, while FRIIs are distributed over the entire redshift (see Figure 3.2). This is not a surprising result as low-power RGs are known to be mainly observed at lower redshift [Laing et al., 1983, Spinrad et al., 1985, Wall and Peacock, 1985, Morganti et al., 1993b, Burgess and Hunstead, 2006a,b].

However, from the optical point of view, the number of HERGs (47) and LERGs (32) is not very different, although a slight predominance of the former class is observed. Indeed, 19 powerful radio galaxies (FRII) are classified as LERGs. As shown in Figure 3.3, there is a clear separation in radio power between FRI-LERGs and FRII-LERGs (signature of a different mean power of the jet over the time) in spite of their optical classification (that, in turn, implies similar accretion efficiency). In fact, the probability that these two populations are drawn from the same distribution, measured through a Kolmogorov-Smirnov test, is 4×10^{-6}. Conversely, the FRII-LERGs and FRII-BLRGs seems to span similar values.

This is a first indication that jet power and accretion mechanisms cannot be simply related, as generally assumed (see section 1.3), but other ingredients should be considered, such as, for example, the environment.

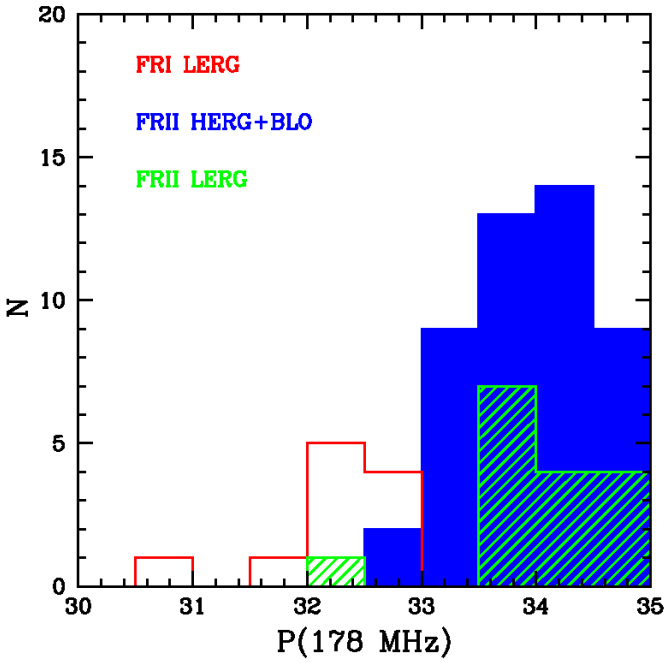

Figure 3.3: Distribution in redshift of the sample: the FRII-HERGs/BLRGs are in blue, FRII-LERGs are in green and FRI-LERGs are in red. A Kolmogorov-Smirnov test indicates that the probability that FRII-LERGs and FRI-LERGs are drawn from the same population is less than 4×10^{-6}, while the FRII-LERGs and FRII-HERGs distributions are clearly overlapping

.

Chapter 4

X-ray analysis and Results

In order to explore the jet-accretion connection and the role of the environment in determining the radio morphology in sources of different FR-type, I performed a systematic X-ray study of all the FRII sources (66) of the above sample. In particular, I focused on FRII-LERGs that are the key targets of my study. They show a radio morphology typical of powerful radio galaxies but their optical spectra suggest inefficient accretion regimes. FRII-HERGs/BLRGs are used as control samples: although most of them have been already published, I re-analyzed all the data in a systematic and homogeneous way.

4.1 Data Reduction

The total number of analyzed sources is 66: 19 FRII-LERGs and 47 FRII-HERGs/BLRGs, as shown in the observation logs (see Tables 4.1, 4.2 and 4.3).

For all the FRII-LERG radio galaxies at least one *Chandra* observation was available. In three cases, i.e. 3C 349, 3C 353 and 3C 460, the spectral signal-to-noise ratio was very low and therefore XMM-*Newton* data were preferred. For the 47 FRII-HERGs/BLRGs only the *Chandra* data were considered, in order to maintain the sample as uniform as possible. This obviously disadvantaged the BLRGs that are usually very bright and therefore affected by strong pile-up ($\geq$10%, see Table 4.3). The only exceptions are 3C 184.1 and 3C 459, for which the pile-up is limited (<10%)

For each satellite, when more than one observation was available, the one with the longest integration was chosen.

Name (1)	**telescope** (2)	**obsID** (3)	**date** (4)	**source CCD** (5)	**exposure** (6)	**Environment** (7)
3C88	C	11977	2009-10-06	ACIS-S	50280	GG
3C132	C	9329	2008-03-26	ACIS-S	7790	-
3C153	C	9302	2007-12-07	ACIS-S	8170	-
3C165	C	9303	2008-02-02	ACIS-S	7770	-
3C166	C	12727	2010-11-29	ACIS-S	8050	-
3C173.1	C	3053	2002-11-06	ACIS-S	24310	-
3C196.1	C	12729	2011-02-11	ACIS-S	8050	GC
3C213.1	C	9307	2008-04-14	ACIS-S	8170	-
3C236	C	10249	2009-01-14	ACIS-I	41040	-
3C288	C	9275	2008-04-13	ACIS-S	40150	GC
3C310	C	11845	2010-04-09	ACIS-S	58320	GC
3C326	C	10908	2009-05-10	ACIS-I	27880	-
3C349	X	0501621601	2007-10-03	EPIC/pn	15113	-
3C353	X	0400930101	2006-08-25	EPIC/pn	44264	-
3C357	C	12738	2010-10-31	ACIS-S	8050	
3C388	C	5295	2004-01-29	ACIS-I	31120	GC
3C401	C	4370	2002-09-21	ACIS-S	25170	GC
3C430	C	12744	2011-11-14	ACIS-S	8050	-
3C460	X	0675400101	2011-12-24	EPIC/pn	48744	-

Table 4.1: Log of the observations of **FRII-LERGs**. Column description: (1) 3CR name; (2) Telescope: C=*Chandra* and X=XMM-*Newton*; (3) Observation ID; (4) Start date of the observation; (5) Instrument that collected the data: ACIS-I/ACIS-S for *Chandra* and EPIC/pn camera for XMM-*Newton*; (6) Total exposure time, in seconds as reported in the public archive; (7) Type of environment: Galaxy Cluster (GC) or Galaxy Group (GG). All the sources are the target of the observation.

Name (1)	**telescope** (2)	**obsID** (3)	**date** (4)	**source CCD** (5)	**exposure** (6)
3C20	C	9294	2007-12-31	ACIS-S	8040
3C33	C	7200	2005-11-12	ACIS-S	20180
3C61.1	C	9297	2008-12-05	ACIS-S	8160
3C79	C	12723	2010-11-01	ACIS-S	7790
3C98	C	10234	2008-12-24	ACIS-I	32130
3C105	C	9299	2007-12-17	ACIS-S	8180
3C133	C	9300	2008-04-07	ACIS-S	8140
3C135	C	9301	2008-01-10	ACIS-S	8040
3C136.1	C	9326	2008-01-10	ACIS-S	10040
3C171	C	10303	2009-01-08	ACIS-S	60220
3C180	C	12728	2010-12-24	ACIS-S	8060
3C192	C	19496	2017-12-18	ACIS-S	70110
3C223	C	12731	2012-01-07	ACIS-S	8050
3C223.1	C	9308	2008-01-16	ACIS-S	8030
3C234	C	12732	2011-01-19	ACIS-S	8050
3C277.3	C	16600	2014-03-11	ACIS-I	98080
3C284	C	12735	2010-11-17	ACIS-S	8050
3C285	C	6911	2006-03-18	ACIS-S	40150
3C300	C	9311	2008-03-21	ACIS-S	8040
3C303.1	C	9312	2008-02-21	ACIS-S	7770
3C305	C	13211	2011-01-06	ACIS-S	29040
3C321	C	3138	2002-04-30	ACIS-S	47730
3C327	C	6841	2006-04-26	ACIS-S	40180
3C379.1	C	12739	2011-04-04	ACIS-S	8050
3C381	C	9317	2008-02-21	ACIS-S	8170
3C403	C	2968	2002-12-07	ACIS-S	50130
3C436	C	12745	2011-05-27	ACIS-S	8060
3C452	C	2195	2001-08-21	ACIS-S	80950
3C456	C	12746	2011-01-17	ACIS-S	8050

Table 4.2: Log of the observations of **FRII-HERGs**. Column description: (1) 3CR name; (2) Telescope: C=*Chandra* and X=XMM-*Newton*; (3) Observation ID; (4) Start date of the observation; (5) Instrument that collected the data: ACIS-I or ACIS-S; (6) Total exposure time, in seconds as reported in the public archive. Notes: all data come from the *Chandra* archive and all the sources are the target of the pointing.

Name (1)	**telescope** (2)	**obsID** (3)	**date** (4)	**source CCD** (5)	**exposure** (6)	**pile-up** (7)
3C17	C	9292	2008-02-02	ACIS-S	8040	22%
3C18	C	9293	2008-06-01	ACIS-S	8050	23%
3c33.1	C	9295	2008-04-01	ACIS-S	8170	11%
3C111	C	9279	2008-12-08	ACIS-S	10140	21%
3C184.1	C	9305	2008-03-27	ACIS-S	8130	7%
3C197.1	C	9306	2007-12-16	ACIS-S	8070	14%
3C219	C	827	2000-10-11	ACIS-S	19240	14%
3C227	C	6842	2006-01-15	ACIS-S	30170	20%
3C287.1	C	9309	2008-03-23	ACIS-S	8120	22%
3C303	C	1623	2001-03-23	ACIS-S	15100	22%
3C323.1	C	9314	2008-06-01	ACIS-S	8040	19%
3C332	C	9315	2007-12-10	ACIS-S	8030	20%
3C390.3	C	830	2000-04-17	ACIS-S	34410	10%
3C410	C	12742	2011-09-24	ACIS-S	8060	21%
3C445	C	7869	2007-10-18	ACIS-S	46200	16%
3C459	C	16044	2014-10-12	ACIS-S	59960	1%

Table 4.3: Log of the observations of **FRII-BLRGs**. Column description: (1) 3CR name; (2) Telescope: C=*Chandra* and X=XMM-*Newton*; (3) Observation ID; (4) Start date of the observation; (5) Instrument that collected the data: ACIS-I or ACIS-S; (6) Total exposure time, in seconds as reported in the public archive; (7) Estimated pile-up percentage evaluated from the Chandra Proposal Planning Toolkit (PIMMS). The pile-up percentage is defined as the percentage of the ratio of the number of frames with two or more events to the number of frames with one or more events. Notes: all data come from the *Chandra* archive, and all the sources were the target of the pointing.

Before starting the X-ray analysis, I briefly checked for possible observational biases. The exposure time and the count distribution for the key and the control samples are shown in Figure 4.1. for the *Chandra* satellite in Figure 4.1, left panel. As only three radio galaxies out of 50 were pointed by XMM-*Newton*, they were not considered in this comparison. The exposure times were similarly distributed. Considering that the analyzed sources were the target of the observation, that span a similar redshift range (see Figure 3.2) and that the satellite configuration was similar, important biases due to the observational set-up are excluded. The differences between counts distribution is therefore intrinsic. This will be discussed later in details.

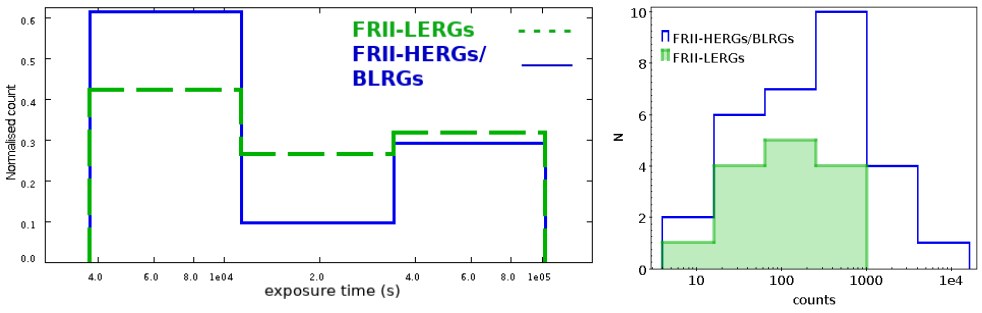

Figure 4.1: *Left Panel*– Effective exposure times (in seconds) of FRII-LERGs (in green) and FRII-HERGs/BLRGs (in blue) observations vs. percentage of observations per population. The exposure time distributions are similar in the two subsamples. *Right Panel*– Counts distribution for the different samples. Color codes are as in the previous histogram. The shift in counts of FRII-HERGs/BLRGs to higher values is real and due to intrinsic different luminosities.

4.1.1 Chandra

All *Chandra* pointings were performed using CCD, ACIS-I and ACIS-S. Data were reprocessed using the software *CIAO* (Chandra Interactive Analysis of Observations), version 4.10 with calibration database CALDB version 4.8.1 and the following standard procedures.

At first, the *chandra_repro* script was run on raw data to create:

- the new bad pixel file that describes a pixel or column as "bad". Events flagged as *bad* are related either to hot-pixels (the focal plane temperature is monitored during all observations) or cosmic ray afterglows (defined as an interaction between a cosmic ray and CCDs which produces a large amount of charge);
- the new event file (Level 2) which contains all the events collected during the observation but the bad pixel events. Periods in which data were not suitable for the analysis (e.g. South Atlantic Anomaly) were also rejected.

The new Level 2 event file is then filtered in the 0.3-7 keV energy range according to the *Chandra* Effective Area, and the image is visualized through the *DS9* software. When the source appeared extended, two images were produced: a soft one (0.3-4 keV) and a hard one (4-7 keV). This approach helps for better defining the pointlike emission from the core. Subsequently, radio contours at 1.4 GHz or 5 GHz were superimposed on both images to properly identify the peak of the emission (see Figure 4.2). For each source, nuclear and background spectra were extracted from circular regions with radius varying between 1.5" and 2.5". I preferred to consider a smaller radius when the presence of extended emission was ascertained, in order to reduce its contamination. In both cases the extraction regions collect at least 90% of the photons (see Figure 2.7). The background was selected in a region in the same CCD of the source, avoiding any contamination from field sources or from the source itself.
Finally, the task *specextract* creates the Redistribution Matrix File (RMF) and the Ancillary Response File (ARF)[1] and produces the final spectra of the source and the background, respectively.

[1]The RMF associates to each instrument channel the corresponding photon energy in keV, while the ARF includes information on the effective area, filter transmission and any additional energy-dependent efficiencies. The spectral analysis requires both response files.

Spectra were grouped to a minimum of 20 counts per bin in order to adopt the χ^2 statistics. When this was not possible, the C-statistics was applied (Cash 1979).

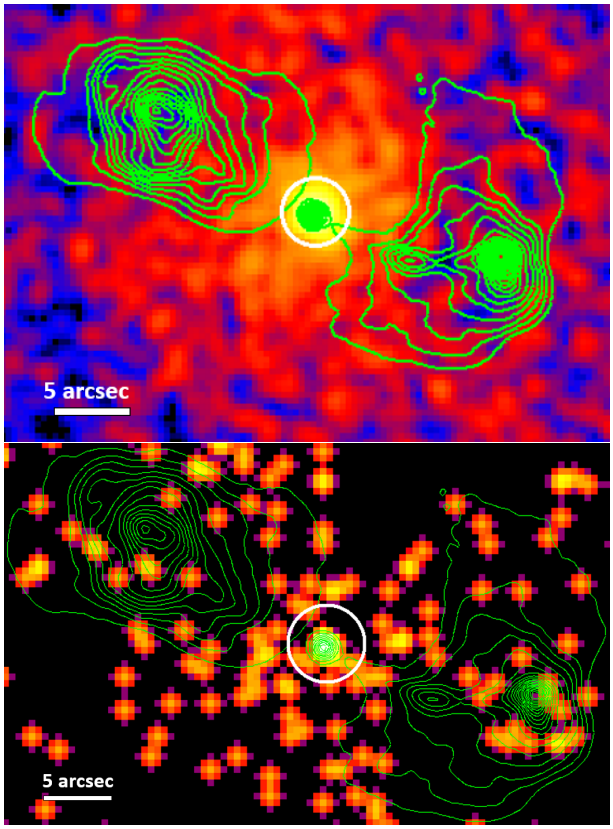

Figure 4.2: *Top panel:* 3C 388 X-ray image (0.3-7 keV) with superimposed radio contours at 1.4 GHz. 3C 388 resides in a galaxy cluster with a temperature of $\sim$ 3.5 keV [Kraft et al., 2006], and the extended emission related to the cluster is clearly visible in the X-ray image. *Bottom panel*: 4-7 keV image with superimposed radio contours (*green lines*). The white circle represents the region ($\sim 2.8''$) used to extract the source spectrum.

4.1.2 XMM-*Newton*

XMM-*Newton* data were reduced using the Scientific Analysis Software (SAS) version 16.1 together with the latest calibration files and following standard procedures. In this work only EPIC/pn data were considered because of the higher sensitivity of this detector with respect to MOS, as explained in the Section 2.2.
The first step was the extraction of a light curve above 10 keV to exclude intervals affected by *flaring* background. This background component is related to soft protons interacting with the detectors. The origin of these protons is thought to be solar: they are trapped in the Earth magnetosphere, causing high-energy flares that should be discarded from the data. On average, the net exposure time is reduced by $\sim$30%-40% with respect to the total.
As for *Chandra*, radio contours were superimposed to the X-ray images. However, it was not possible to disentangle nuclear and extended emission, if even present, because of the low resolution

power of XMM-*Newton*.
Source and background spectra were extracted from circular regions with radius varying between 20" and 30", depending on the sources, in order to maximize the S/N ratio. Given the chose extraction regions, in all cases at least 80% of photons fell within the extraction region (see Figure 2.12). The background was chosen in the same CCD of the source, avoiding any contamination from field sources or from the source itself.
RMF and ARF files were created through the tasks *RMFGEN* and *ARFGEN*, and finally spectra for the source and the background were extracted, respectively. As a final step, the source spectrum was grouped to a minimum of 20 counts per bin through the FTOOL *grppha* and the χ^2 statistics applied in the spectral analysis.

4.2 Spectral analysis

Before proceeding with the spectral analysis, a visual inspection of the *Chandra* images in the soft X-ray band was performed to investigate the presence and the extent of the emission. This information helped us in modeling the spectra of the more complex sources.
The spectral analysis was performed using the software *XSPEC* version 12.9.1 [Arnaud, 1996]. Errors are quoted at 90% confidence for one interesting parameter ($\Delta\chi^2$=2.71: Avni [1976]). Spectral fitting was performed in the energy range 0.5-7 keV (*Chandra*) and 0.5-10 keV (*XMM-Newton*).

Each source was initially fitted with a power law absorbed by Galactic column density [Kalberla et al., 2005]. This simple model worked well in a few number of cases. The majority of the sources required a more complex treatment. Depending on the residual deviations and the energy band in which they occurred, new models were considered. In particular:

- an intrinsic absorption (N_H) when residuals below a few keV were negative or the photon index assumed very low values. A uniform (ZPHABS) or a patchy (ZPCFABS) absorber was tested. As explained in Section 1.4, absorption by neutral gas is often observed in AGN. It is thought that the absorption is associated either with a toroidal structure at pc scales or with a galaxy gas distribution on kpc scales;

- a thermal emission model (MEKAL) and/or a second scattered power law when residuals below few keV were in excess. Thermal emission can be due to intra-cluster medium or hot corona typical of early-type galaxies [Fabbiano et al., 1992]. A MEKAL model can also mimic soft photo-ionized emission lines produced in the NLR and difficult to be resolved with the CCD spectral resolution [Grandi, 2007, Piconcelli et al., 2008].
  Instead, the second power law is probably due to the scattered component of the primary power law. The scattering occurs far away from the center, probably in a hot gas region above the torus;

- a Gaussian line and/or reflection component (PEXRAV) when positive residuals were observed in the region of the iron Kα line (5-7 keV). The iron line is a reprocessed fluorescence feature due to the presence of cold matter which is also responsible for the reflection, as discussed in Section 1.4. Once the line was detected, the presence of the reflection component was verified. In PEXRAV the cut-off energy was fixed to 100 keV and the inclination angle to 60°. The adopted energy cut-off is quite common in AGN (Grandi et al. 2006). This kind

of angle implies that the RG is almost an edge-on source. However, these parameters do not impact significantly the fit given to low statistics.

Each time a new component was added to the model, an F-test was performed (when the χ^2 statistics was adopted). I assumed that an F-probability larger than 95% implies a significative improvement in the fit.
For the sources 3C 136.1, 3C 153 and 3C 430 the small number of counts (about 10 counts in the whole spectrum) prevented any modeling. Fluxes and luminosities were estimated using the Chandra Proposal Planning Toolkit (PIMMS)[2] and assuming a simple power law model with $\Gamma = 1.7$.
In six cases the FRII-LERGs are in a cluster: in spite of the low statistics of the spectra, the nuclear component was clearly detected in four cases. For 3C 288 the result is ambiguous: both a power law and a MEKAL model can reproduce the data pretty well. For this reason I assumed the 2-10 keV estimated luminosity as an upper limit of the nuclear AGN emission. In one case, the FRII-LERG 3C 196.1, the source is completely overwhelmed by the cluster emission, thus precluding any nuclear study.
A summary of the best-fit spectral parameters is reported in Table 5.1. Examples of the fitted spectra both for FRII-LERGs and HERGs are shown in Figure 4.3.

[2] `http://cxc.harvard.edu/toolkit/pimms.jsp` .

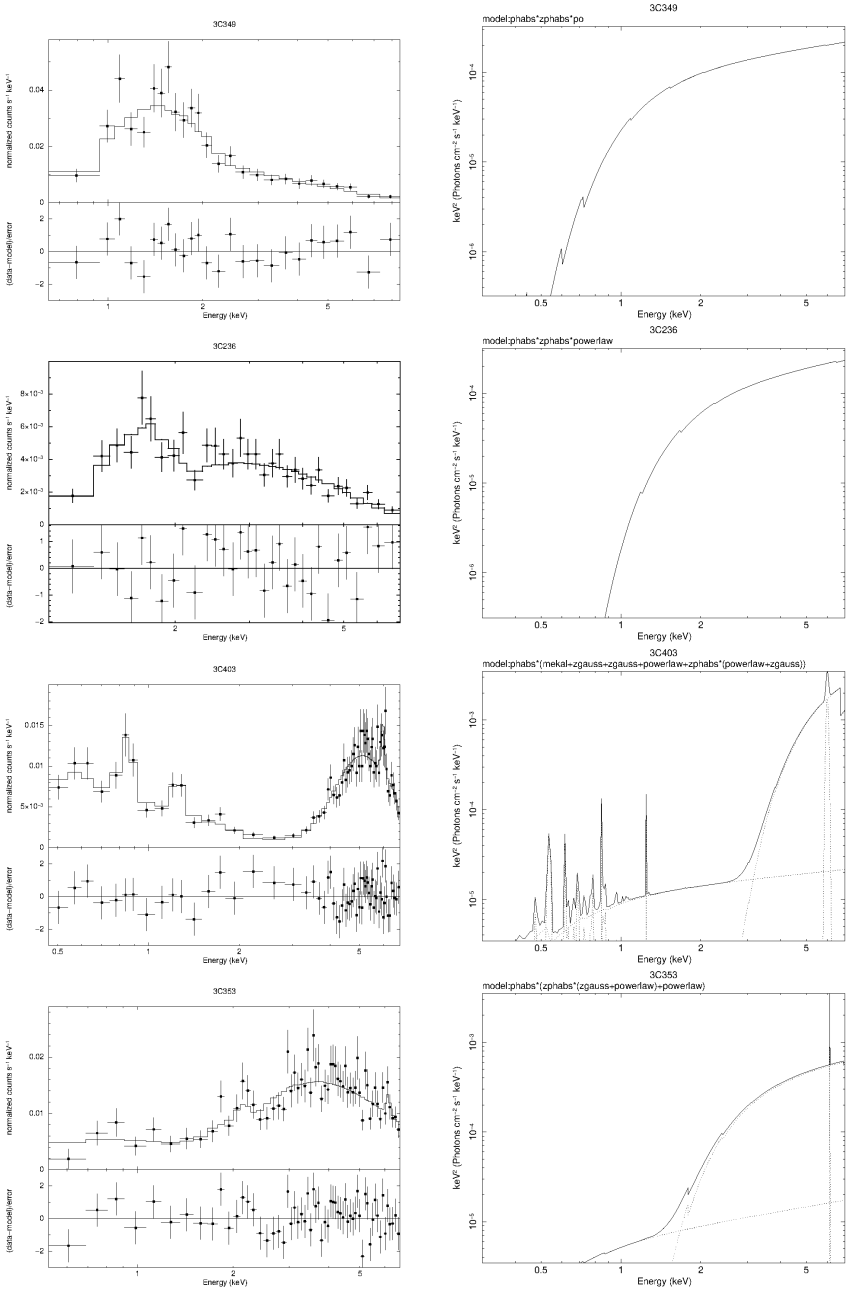

Figure 4.3: Examples of FRII-LERGs and FRII-HERGs X-ray spectra. On the left panels there are the spectral data, best-fitting models and residuals values ((data-model)/error), while on the right panels there are the adopted models. *Panel 1:* 3C 349 (FRII-LERG): the adopted model is a simple power law with photon index $\Gamma = 1.5$; *Panel 2:* 3C 236 (FRII-LERG): the best-fit model is a power law ($\Gamma = 1.9$) absorbed by intrinsic column density, $N_H \approx 1.9 \times 10^{22}$ cm^{-2}; *Panel 3:* 3C 403 (FRII-HERG): the source has a complex model with an absorbed power law in the hard band, a scattered power law in the soft band plus two photoionized emission lines and a thermal emission (see Section 4.3.1 for a detailed analysis); *Panel 4:* 3C 353 (FRII-LERG): the best-fit model is an absorbed power law ($N_H \approx 6 \times 10^{22}$ cm^{-2}) and a scattered power law.

Table 4.4: X-ray analysis

Name	Optical class	z	NH_{Gal}	Model	NH_{intr}	Γ_H	Γ_S	kT	other feat.	$L_{0.5-2}$	L_{2-10}	Statistics
(1)	(2)	(3)	(4)	(5)	(6)	(7)	(8)	(9)	(10)	(11)	(12)	(13)
							LERGs					
3C88	LERG	0.0302	8.3	[vii]	2.8 ± 0.9	1.9 ± 0.5	-	-	CF=$0.87^{+0.07}_{-0.01}$	-	$(5^{+5}_{-3})\times10^{41}$	19.2/26
3C132	LERG	0.2140	21.3	[ii]	5^{+4}_{-3}	1.7†	-	-	-	-	$(2.2^{+1.2}_{-0.8})\times10^{43}$	4.1/5 C
3C153	LERG	0.2769	16.2	[i]	-	1.7†	-	-	-	-	1.5×10^{42}	-
3C165	LERG	0.2957	19.4	[ii]	3 ± 2	1.7†	-	-	-	-	$(2.3^{+1.1}_{-0.8})\times10^{43}$	8.2/14 C
3C166	LERG	0.2449	17.1	[i]	<0.13	1.6 ± 0.1	-	-	-	-	$(9\pm1)\times10^{43}$	20/19
3C173.1	LERG	0.292	4.5	[vi]	30^{+200}_{-20}	1.7†	1.7†	-	$EQW_{Fe}=886^{+\infty}_{-789}$	$(3^{+3}_{-2})\times10^{41}$	$(2.7^{+18.2}_{-1.6})\times10^{43}$	35.3/25 C
3C196.1	LERG	0.1980	6.0	[viii]	-	-	-	$3.2^{+1.3}_{-0.8}$	-	$(9\pm1)\times10^{42}$	-	20.5/13 C
3C213.1	LERG	0.1939	2.4	[i]	<0.43	$1.9^{+0.5}_{-0.4}$	-	-	-	-	$(4\pm1)\times10^{42}$	15.4/9 C
3C236	LERG	0.1005	1.0	[ii]	$1.9^{+0.6}_{-0.5}$	1.4 ± 0.3	-	-	-	-	$(1.2^{+0.7}_{-0.4})\times10^{43}$	27.0/29
3C288	LERG	0.2460	0.8	[i]	<1.2	$2.1^{+0.4}_{-0.3}$	-	-	-	-	$(5\pm1)\times10^{42}$	6.0/6
				[viii]	-	-	-	-	$3.7^{+2.9}_{-1.2}$	$(3.6^{+0.6}_{-0.5})\times10^{42}$	-	6.4/6
3C310	LERG	0.0535	3.7	[ix]	<0.36	1.7†	-	$0.8^{+0.2}_{-0.1}$	-	$(7\pm2)\times10^{40}$	$(3\pm2)\times10^{40}$	22.6/27 C
3C326	LERG	0.0895	9.0	[ii]	$2.2^{+2.8}_{-1.7}$	1.7†	-	-	-	-	$(2^{+2}_{-1})\times10^{41}$	3.4/3 C
3C349	LERG	0.2050	1.9	[ii]	0.9 ± 0.2	1.5 ± 0.2	-	-	-	-	$(5^{+2}_{-1})\times10^{43}$	22.7/23
3C353	LERG	0.0304	9.3	[vi]	6 ± 1	1.5 ± 0.3	1.5=Γ_h	-	$EQW_{Fe}<78$	$(3.0\pm0.8)\times10^{40}$	$(3^{+2}_{-1})\times10^{42}$	58.2/56
3C357	LERG	0.1662	3.1	[vii]	$2.9^{+1.3}_{-0.9}$	1.7†	-	-	$CF=0.94^{+0.04}_{-0.06}$	-	$(2.4^{+0.6}_{-0.5})\times10^{43}$	21.9/20 C
3C388	LERG	0.0917	5.5	[ix]	<0.54	$2.3^{+0.5}_{-0.6}$	-	$1.3^{+0.4}_{-0.3}$	-	$(7\pm4)\times10^{41}$	$(8\pm4)\times10^{41}$	12.3/14
3C401	LERG	0.2011	5.9	[i]	<0.07	1.9 ± 0.2	-	-	-	-	$(5.3\pm0.7)\times10^{42}$	6.3/10
3C430	LERG	0.0541	33.1	[i]	-	-	-	-	-	-	$\approx5.3\times10^{40}$	-
3C460	LERG	0.2680	4.7	[iii]	18^{+15}_{-7}	1.7†	2.7 ± 0.6	-	-	$(3.0\pm0.5)\times10^{42}$	$(3.4^{+1.6}_{-0.9})\times10^{43}$	28.7/25

Name	Optical class	z	NH_{Gal}	Model	NH_{intr}	Γ_H	Γ_S	kT	other feat.	$L_{0.5-2}$	L_{2-10}	Statistics
(1)	(2)	(3)	(4)	(5)	(6)	(7)	(8)	(9)	(10)	(11)	(12)	(13)
						HERGs						
3C20	HERG	0.1740	18.0	[ii]	15^{+4}_{-3}	1.7†	-	-	-	-	$(1.1^{+0.3}_{-0.2})\times10^{44}$	24.1/25 C
3C33	HERG	0.0596	3.4	[v]	53^{+8}_{-7}	1.7†	1.7=Γ_h	-	$EQW_{Fe} = 139 \pm 89$ $R = 1.5^{+0.4}_{-0.6}$	$(1.0^{+0.3}_{-0.2})\times10^{42}$	$(1^{+0.3}_{-0.2})\times10^{44}$	32.5/40
3C61.1	HERG	0.1840	7.9	[iii]	29^{+23}_{-12}	1.7†	1.2±1.0	-	-	$(7\pm4)\times10^{41}$	$(4^{+4}_{-2})\times10^{43}$	30/18 C
3C79	HERG	0.2559	8.7	[vi]	31^{+12}_{-9}	1.7†	1.7†	-	$EQW_{Fe} < 157$	$(1.8^{+1.0}_{-0.7})\times10^{42}$	$(2.4^{+1.3}_{-0.8})\times10^{44}$	12.7/14 C
3C98	HERG	0.0304	10.0	[iv]	$9.4^{+1.0}_{-0.9}$	1.7†	-	-	$EQW_{Fe} = 277 \pm 135$	-	$(5.3^{+0.5}_{-0.3})\times10^{42}$	57.4/48
3C105	HERG	0.0890	12.0	[iv]	43^{+7}_{-6}	1.7†	-	-	$EQW = 178 \pm 132$	-	$(2.2^{+0.9}_{-0.5})\times10^{44}$	13.6/12
3C133	HERG	0.2775	25.0	[ii]	$0.8^{+0.4}_{-0.3}$	2±0.3	-	-	-	-	$(1.9^{+0.8}_{-0.5})\times10^{44}$	39.4/26
3C135	HERG	0.1253	8.7	[vi]	34^{+32}_{-19}	1.7†	2.2±1.0	-	$EQW_{Fe} = 916^{+1500}_{-717}$	$(5\pm2)\times10^{41}$	$(1.4^{+2.3}_{-0.8})\times10^{43}$	15.8/13 C
3C136.1	HERG	0.0640	32.0	[i]	-	1.7†	-	-	-	-	$\approx 5.9\times10^{40}$	-
3C171	HERG	0.2384	5.7	[ii]	10±3	2±0.5	-	-	-	-	$(1.7^{+2.0}_{-0.9})\times10^{44}$	16.1/19
3C180	HERG	0.2200	14.0	[iii]	70^{+160}_{-50}	1.7†	1.7†	-	-	$(1.0^{+0.6}_{-0.5})\times10^{42}$	$(9^{+182}_{-7})\times10^{43}$	8.2/7 C
3C192	HERG	0.0598	3.9	[iii]	34^{+10}_{-8}	$1.9^{+0.7}_{-0.6}$	1.9=Γ_h	-	-	$(6\pm2)\times10^{40}$	$(2.2^{+8}_{-2})\times10^{42}$	13.9/15 C
3C223	HERG	0.1368	1.0	[iii]	13^{+13}_{-7}	1.7†	1.7†	-	-	$(1.4\pm0.4)\times10^{42}$	$(2.0^{+1.6}_{-0.8})\times10^{43}$	10/10 C
3C223.1	HERG	0.1070	1.3	[ii]	28±6	1.7†	-	-	-	-	$(9^{+3}_{-2})\times10^{43}$	9.3/12 C
3C234	HERG	0.1848	1.8	[vi]	17^{+9}_{-6}	1.7†	2.3±0.5	-	$EQW_{Fe} = 939^{+391}_{-400}$	$(7\pm1)\times10^{42}$	$(1.5^{+0.7}_{-0.5})\times10^{44}$	6.6/8
3C277.3	HERG	0.0857	0.9	[iii]	25^{+5}_{-4}	1.7†	1.7†	-	-	$(1.8\pm0.3)\times10^{41}$	$(1.0\pm0.2)\times10^{43}$	26.2/22
3C284	HERG	0.2394	0.9	[i]	< 0.91	2.3±1.0	-	-	-	-	$(1.1^{+0.4}_{-0.5})\times10^{42}$	1.4/5 C
3C285	HERG	0.0794	1.3	[vi]	38^{+8}_{-6}	1.7†	1.7†	-	$EQW_{Fe} = 367^{+144}_{-47}$	$(1.4\pm1)\times10^{41}$	$(3.5^{+1.0}_{-0.7})\times10^{43}$	7.7/11
3C300	HERG	0.2700	2.5	[i]	< 0.19	1.4±0.3	-	-	-	-	$(1.3\pm0.2)\times10^{43}$	12.7/10 C
3C303.1	HERG	0.2670	3.0	[iii]	18^{+132}_{-16}	1.7†	4†	-	-	$(3^{+2}_{-1})\times10^{42}$	$(1.5^{+40.0}_{-1.1})\times10^{43}$	0.1/2 C
3C305	HERG	0.0416	1.3	[ix]	< 0.95	1.7†	-	0.9±0.3	-	$(2^{+2}_{-1})\times10^{40}$	$(5\pm2)\times10^{40}$	2.4/7 C

Name	Optical class	z	NH_{Gal}	Model	NH_{intr}	Γ_H	Γ_S	kT	other feat.	$L_{0.5-2}$	L_{2-10}	Statistics
(1)	(2)	(3)	(4)	(5)	(6)	(7)	(8)	(9)	(10)	(11)	(12)	(13)
3C321	HERG	0.0960	3.8	[x]	26^{+20}_{-13}	$1.7^{\dagger}$	2.8 ± 0.2	-	$EQW_{Fe} = 988^{+751}_{-474}$ photo-ionized lines Table 4.5	$(8.3^{+0.7}_{-0.6})\times10^{41}$	$(4^{+4}_{-2})\times10^{42}$	61.2/40 C
3C327	HERG	0.1041	5.9	[xi]	30^{+63}_{-18}	$1.7^{\dagger}$	$1.7^{\dagger}$	$0.20^{+0.04}_{-0.02}$	$EQW_{Fe} = 2000^{+3000}_{-742}$	$(1.9\pm0.1)\times10^{42}$	$(8^{+31}_{-4})\times10^{42}$	46.6/25
3C379.1	HERG	0.2560	5.4	[vi]	60^{+70}_{-30}	$1.7^{\dagger}$	$1.7^{\dagger}$	-	$EQW_{Fe} = 557^{+1900}_{-464}$	$(1.2^{+0.9}_{-0.7})\times10^{42}$	$(1.1^{+4.0}_{-0.7})\times10^{44}$	7.3/8 C
3C381	HERG	0.1605	9.9	[vi]	29^{+8}_{-7}	$1.7^{\dagger}$	$1.7^{\dagger}$	-	$EQW_{Fe} < 216$	$(1.8\pm0.5)\times10^{42}$	$(2.1^{+0.8}_{-0.6})\times10^{44}$	14.8/18
3C403	HERG	0.0590	12.1	[xii]	46 ± 3	$1.7^{\dagger}$	$1.7^{\dagger}$	0.2 ± 0.03	$EQW_{Fe} = 153^{+60}_{-15}$ photo-ionized lines Table 4.6	$(4.0\pm0.4)\times10^{41}$	$(7.8^{+1.0}_{-0.9})\times10^{43}$	51.5/57
3C436	HERG	0.2145	6.7	[iv]	37^{+22}_{-16}	$1.7^{\dagger}$	-	-	$EQW_{Fe} < 288$	-	$(9.3^{+9.0}_{-0.4})\times10^{43}$	17.3/15 C
3C452	HERG	0.0811	9.8	[v]	53^{+8}_{-7}	$1.7^{\dagger}$	$1.7^{\dagger}$	-	$EQW_{Fe} = 172^{+65}_{-65}$ $R = 2^{+0.4}_{-0.5}$	$(1.7^{+0.5}_{-0.3})\times10^{42}$	$(1.0^{+0.2}_{-0.2})\times10^{44}$	96.8/76
3C456	HERG	0.2330	3.7	[ii]	7 ± 1	$1.7^{\dagger}$	-	-	-	-	$(1.6\pm0.2)\times10^{44}$	63.6/59 C
							BLRGs					
3C184.1	BLRG	0.1182	3.2	[iii]	8 ± 1	$1.7^{\dagger}$	$1.7^{\dagger}$	-	-	$(7\pm3)\times10^{41}$	$(1.1\pm0.1)\times10^{44}$	19.8/24
3C459	BLRG	0.2199	5.2	[xiii]	6^{+5}_{-2}	$1.7^{\dagger}$	$1.7^{\dagger}$	$0.7^{+0.3}_{-0.6}$	-	$(4.8^{+0.9}_{-1.0})\times10^{42}$	$(1.6\pm0.4)\times10^{43}$	15.8/17

Table 4.4: Column description: (1) 3CR name; (2) optical classification; (3) redshift from Spinrad et al. [1985]; (4) Milky Way absorption in units of 10^{20}cm^{-2} from Kalberla et al. [2005]; (5) X-ray spectral model adopted: [i] phabs*po; [ii] phabs*zphabs*po; [iii] phabs*(zphabs*po+po); [iv] phabs*zphabs*(po+zgauss); [v] phabs*(zphabs*(po+zgauss)+po+pexrav); [vi] phabs*(zphabs*(po+zgauss)+po); [vii] phabs*zpcfabs*po; [viii] phabs*mekal; [ix] phabs*(mekal+po); [x] phabs*(zphabs*(po+zgauss)+po+2zgauss); [xi] phabs*(zphabs*(po+zgauss)+mekal+po); [xii] phabs*(zphabs*(po +zgauss)+po+2zgauss+mekal); [xiii] phabs*(mekal+po+(zphabs*po)) (models: po=power law, phabs=absorption at z=0, zphabs=absorption at z$\neq$ 0, zgauss= Gaussian feature at z$\neq$ 0, pexrav=Exponentially cut-off power law spectrum reflected from neutral material, mekal=thermal emission from hot gas, zpc-fabs=partial covering factor) (6) intrinsic absorption in units of 10^{22} cm^{-2}; (7) and (8) photon index of the principal and secondary power law (†=parameter locked); (9) thermal component (mekal) in units of *keV*; (10) other features: rest-frame equivalent width of the Fe line (at 6.4 keV) in eV , Covering Factor (CF), Reflection parameter (R) defined as: $R = \Omega/2\pi$, where Ω is the solid angle covered by the reprocessing medium; (11) soft-band luminosity (0.5-2 keV) in units of erg/s; (12) hard-band luminosity (2-10 keV) in units of erg/s; (13) fit statistic: it has been used χ^2-statistic for spectra with grouping at least 20 counts/bin and the Poissonian statistic (C-stat, C in the table) for very low grouping values (a few counts per bin).

4.3 X-ray results

In this Section the main results obtained from the spectral analysis are discussed and the comparison between the key sample (FRII-LERGs) and the control sample (FRII-HERGs) are presented. To further complement my study, the 3CR/FRI-LERGs with X-ray information available from the literature are also taken into account [Balmaverde et al., 2006, Torresi et al., 2018].

4.3.1 Nuclear X-ray continuum

For 15 out of 19 FRII-LERGs X-ray parameters could be constrained. These radio galaxies usually show very simple spectra, well represented by a power law. A moderate intrinsic absorption ($N_H \sim 2 \times 10^{22}$ cm^{-2}) was found in 69% (11/16) of the targets. The absorption is usually assumed to be uniform except for 3C 88 and 3C 357, where a patchy cold medium seems to be more appropriate (see Table 4.4).
In one case, i.e. 3C 173.1, the amount of absorbing gas is as high as $N_H \sim 3 \times 10^{23}$ cm^{-2}. Incidentally, this is the only source in the FRII-LERG sample with a detection of the iron fluorescent Kα line at 6.4 keV. The intensity of the line, within the large uncertainties, is compatible with beeing produced by the same matter obscuring the nuclear region [Matt, 1994]. As it will be discussed later in details, 3C 173.1 is the only FRII-LERG of the sample showing X-ray properties typical of FRII-HERGs.

In some cases, a soft X-ray component, in addition to the absorbed power law was required. For 3C 310 and 3C 388 this soft emission is clearly due to the cluster. Instead, in three cases the emission has a nuclear origin, i.e. produced by a scattered component due to electrons located far from the center (probably in the polar regions of the AGN). As expected, the normalization values of the scattered component is, in all 3 cases, a few percent of the absorbed one, spanning from 2% to 8%, consistent with results for obscured AGN (e.g. Lanzuisi et al. [2015], Bianchi and Guainazzi [2007];).

The control sample consists of 29 FRII-HERGs and 2 FRII-BLRGs. These are the only radio galaxies for which an X-ray analysis could be performed. In general, FRII-HERGs show very complex spectra. These results confirm the idea that FRII-HERGs are the Radio-Loud counterpart of Radio-Quiet Seyfert 2 galaxies (e.g. Dadina [2008]): also in the sources with strong jets pointing away from the observer, the X-ray continuum is mostly blocked by gas matter, while part of it is scattered far from the center. The nuclear continua are absorbed with column densities ranging from $\sim 10^{22}$ cm^{-2} to $\sim 10^{24}$ cm^{-2}. Intense iron lines are often detected (11 out 29) showing EW values spanning from 140 eV to more than 1 keV. In at least two cases, i.e. 3C 33 and 3C 452, a Compton reflection was also detected. In four cases a thermal emission, signature of the gas is present (this part will be discussed in the next Section).

Among the BLRGs observed by *Chandra*, only two BLRGs could be analyzed. They are moderately absorbed ($\sim 10^{22}$ cm^{-2}) and in one case (3C 459) thermal emission is also observed.

4.3.2 Soft diffuse X-ray emission

The X-ray imaging analysis indicates that 6 out of 19 FRII-LERGs are in clusters (see Table 4.1) or dense environments. All lie at the centre of the cluster but 3C 88 which resides in the center of a galaxy group. Conversely, no FRII-HERG/BLRG is found in clusters, in agreement with

the fact that generally these sources are isolated. Even a simple inspection of the X-ray images indicates that the extension of the soft emission in FRII-HERGs/BLRGs is significantly smaller than in FRII-LERGs, confirming that the nature of this is local (related to the galaxy rather than the environment) in radio galaxies with high-excitation emission lines.

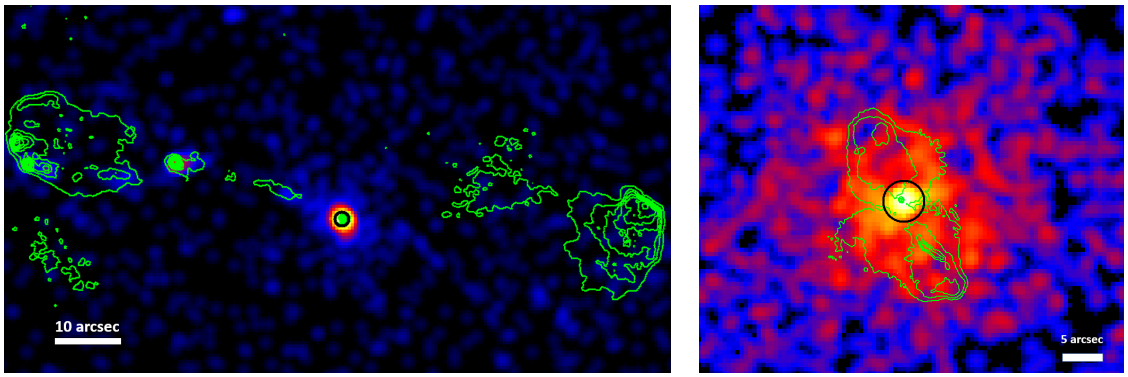

Figure 4.4: *Left panel*: FRII-HERG (3C403, z=0.059) *Chandra* X-ray image (0.3-7 keV) and VLA radio contours (5 GHz). *Right panel*: FRII-LERG (3C401, z=0.2011) *Chandra* X-ray image (0.3-7 keV) and VLA radio contours (1.5 GHz). The environment of FRII-HERGs/BLRGs and FRII-LERGs is different. In HERGs the soft emission is related to the NLR, while in LERGs it is produced by the intra-cluster medium.

While in FRII-LERGs the soft emission is reproduced by a collisional gas (MEKAL) in agreement with the presence of the cluster, in FRII-HERGs/BLRGs the picture is probably more complex. In the literature it has been ascertained that the extended X-ray emission is related to gas photoionized by the central engine and located in the NLR, similarly to Seyfert 2s [Grandi, 2007, Piconcelli et al., 2008, Torresi, 2009, Balmaverde et al., 2012]. Photoionized gas is different from collisional gas, in terms of temperature and density. Therefore, the use of the MEKAL model in the FRII-HERGs/BLRGs spectra is a rough modelization of the features given the limited energy resolution of CCD detectors. However, in a few cases it is possible to resolve the single photoionized lines. This was the case for 3C321 and 3C403, where strong emission associated to resolved lines produced by photoionized gas, could be detected (see Tables 4.5, 4.6).

Energy	Intensity	Statistics	EW	Tentative ID
$0.57^{+0.04}_{-0.03}$	$3.2^{+2.6}_{-2.3}$	61.3/40	0.043	O VII
$0.88^{+0.03}_{-0.04}$	$2.1^{+1.1}_{-1.0}$	69.9/40	0.092	Ne IX

Table 4.5: 3C321 Emission lines. Column description: Centroid of the emission line in keV; line flux in units of 10^{-6} photons cm^{-2} s^{-1}; fit statistics values excluding the line from best-fit model. CSTAT statistics was adopted. The best-fit model, including the lines, has value CSTAT=55.7 with 38 degree of freedom, hence the improvement produced by the inclusion of each line is $\Delta_{CSTAT} = 61.3 - 55.7$ and $\Delta_{CSTAT} = 69.9 - 55.7$; photoionized gas emission lines corresponding to those energies.

Energy	Intensity	Statistics	EW	Tentative ID
$0.90^{+0.02}_{-0.03}$	2.6 ± 1.3	4.3×10^{-3}	0.119	Ne IX
1.32 ± 0.04	1.1 ± 0.6	1.4×10^{-2}	0.123	Mg XI

Table 4.6: 3C403 Emission lines. Column description: Centroid of the emission line in keV; line flux in units of 10^{-6} photons cm^{-2} s^{-1}; significance of the fit improvement based on the F-test (Gaussian statistics was adopted) including the line in the model; photoionized gas emission lines corresponding to those energies.

Chapter 5

Discussion and conclusions

The aim of the present study is to investigate the nature of FRII-LERG sources and shed new light on the link between accretion onto SMBH and ejection of relativistic jets. In the classical picture, FRII sources harbour powerful nuclei producing high-excitation emission lines (HERGs/BLRGs), while FRI sources have less luminous nuclei and low-excitation emission lines. The peculiarity of FRII-LERGs, key sample of this project, is that they combine low-power optical nuclei with large-scale radio morphologies typical of strong FRII sources.
To characterize the properties of the innermost nuclear regions, I performed a detailed *Chandra* and XMM-*Newton* analysis of **50 FRII sources** belonging to the 3CR sample at z$<$ 0.3: 19 FRII-LERGs and 31 FRII-HERGs/BLRGs, used as a control sample. In addition, I considered archival data for 13 FRI-LERG objects. The results of the X-ray study are summarized as follows:

- FRII-LERGs are generally well modeled by a power law absorbed by a moderate intrinsic column density ($N_H \sim 10^{22}$ cm^{-2});
- conversely, the nuclei of FRII-HERGs nuclei are generally embedded in dense nuclear environments, as attested by high values of the intrinsic column densities ($N_H > 10^{23}$ cm^{-2}) and by the presence of reprocessed features, i.e. fluorescence iron line and, in at least two cases, a reflection component;
- soft X-ray emission is observed in most of the analyzed radio galaxies. In FRII-HERGs, that are generally found isolated, this emission can be due to both collisional gas of the galaxy hot corona and photoionized gas in the NLR. When extended emission is revealed in FRII-LERGs, in a minority of cases (6/18), this is related to the cluster in which the source is hosted, as directly observed in the X-ray images (see Appendix B).

In the following, I present a comparison of the fundamental observables in FRI-LERGs, FRII-LERGs, and FRII-HERGs/BLRGs. In light of this comparison, then I discuss three possible scenarios:

1. FRII-LERGs and FRII-HERGs are the same objects seen through different obscuring screens;
2. FRII-LERGs form FRII morphologies due to favorable environmental conditions;
3. FRII-LERGs were powerful HERGs in the past.

5.1 Comparing the main observables

5.1.1 $L_{[OIII]}$ as a proxy of the accretion rate

The optical classification of FRII radio galaxies is based on the emission lines. Among them, the [OIII]λ5007 line is particularly interesting, as it is considered a proxy of the accretion. The ionizing radiation L_{ion} (that depends on the accretion efficiency) is related to the [OIII] luminosity $L_{[OIII]}$ by the relation $Log\ L_{ion} \sim Log\ L_{[OIII]} + 2.83$ [Buttiglione et al., 2009]. Since FRII-LERGs have a lower oxygen luminosity, they should also accrete less efficiently. However, $L_{[OIII]}$ is not a valid indicator if dust screens intercept the photoionized photons produced in the NLR.

Using the Balmer decrement, it is possible to estimate the dust content. Adopting an extinction curve $\kappa(\lambda)$, the intrinsic color excess can be expressed as:

$$E(B-V)_i = \frac{2.5}{[\kappa(H_\beta) - \kappa(H_\alpha)]} \times \frac{(H_\alpha/H_\beta)_o}{1/2.86}$$

.

Details on the derivation of the above formula can be found in the Appendix of Momcheva et al. [2013]. The number 2.86 is the theoretical ($\frac{H_\alpha}{H_\beta}$) ratio expected if the temperature and the electron density of the NLR are T=10^4 K and N_e=10^3 cm^{-3}, respectively [Osterbrock, 1989]. Several functional forms for the attenuation curve are present in literature. The most used are: the Milky Way extinction curve [Cardelli et al., 1989], the Large and Small Magellanic Cloud extinction curves from [Gordon et al., 2003] and a general extra-galactic extinction curve from [Calzetti et al., 2000]. The reddening study was performed considering all the different extinction curves. As the results are similar, hereafter the discussion is based on the Milky Way extinction curve.

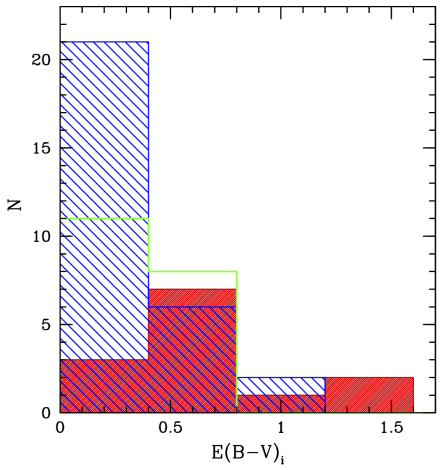

Figure 5.1: Distribution of the intrinsic excess of color E(B-V)$_i$ due to the dust in the key and control samples of radio galaxies. FRII-LERGs are shown in green and FRII-HERGs/BLRGs in blue. The intrinsic reddening of FRI-LERGs is also shown for comparison. While no difference is observed in the dust distribution of FRII sources (in and beyond the NLR), FRIs are significantly reddened, with a pronounced tail at values above 0.75

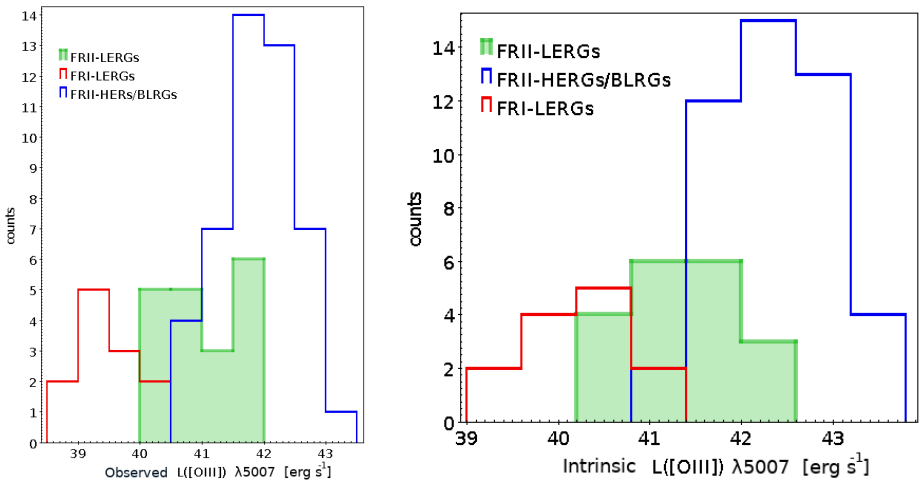

Figure 5.2: [OIII] luminosity for FRII-HERGs/BLRGs, FRII-LERGs and FRIs not corrected (*left panel*) and corrected (*right panel*) for dust extinction; see text for details.

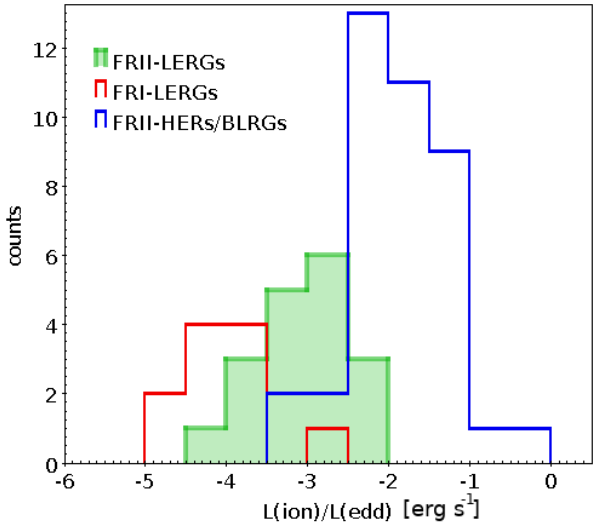

Figure 5.3: Histogram of the ratio between the ionizing luminosity (calculated from $L_{[OIII]}$) and Eddington luminosity (calculated using the M_{BH} estimate). The three populations appear to occupy different regions of the diagram, as confirmed by the statistics: see Table 5.1 and text for details.

In Figure 5.1 the E(B-V) distribution for the different classes is shown assuming a Milky Way extinction. There is no significant difference in dust distribution between FRII-HERGs/BLRGs and FRII-LERGs, as attested by a Kolmogorov Smirnov test. The probability that the two data sets are drawn from the same population is 12% ($P_{KS} = 0.12$). This definitively exclude that the optical classification of FRIIs is affected by the presence of dust. On the contrary, FRI-LERGs suffer more reddening than FRIIs. Indeed, the median value of $E(B\text{-}V)_i$ is 0.72 (mean value 0.67 and standard deviation (sdv) 0.40) for FRI-LERGs and only 0.20 (mean value 0.25 and sdv=0.25) and 0.33 (mean 0.36 and sdv=0.27) for FRII-LERGS and FRII-HERG/BLRG, respectively. A

Kolmogorov-Smirnov test confirms that the excess of color is significantly different in FRIs and FRIIs ($P_{KS} = 0.007$). This suggests a different spatial dust distribution in FRIs and FRIIs.

In Figure 5.2, the observed (*left panel*) and dust-corrected (*right panel*) [OIII] luminosities are compared. As expected, the distribution of the FRII classes does not change significantly. FRIs are still separated from FRIIs, in spite of their corrected [OIII] luminosities being shifted to higher values. In order to exclude any possible dust effect, the ionizing luminosities are derived from the corrected $L_{[OIII]}$ adopting a mean bolometric correction to the [OIII] luminosity of 600 [Kauffmann and Heckman, 2009].

The ionizing luminosity can be used to estimate the accretion rate in terms of L_{ion}/L_{Edd}. The Eddington luminosity $L_{Edd} = 1.3 \times 10^{38} M/M_{\odot}$ *erg* s^{-1} was calculated by exploiting the known relation between the H-band host galaxy magnitude M_H and the black hole mass M_{BH} [Marconi and Hunt, 2003]. The BH masses of the sample are very large, as expected in RL AGN, peaking around 10^9 $M_{\odot}$ with a small dispersion. As expected, there is a clear bimodality in the accretion rate between FRI-LERGs and FRII-HERGs/BLRGs. Quite surprisingly, on the other hand, FRII-LERGs are not as inefficient as classic low-power AGN. Their L_{ion}/L_{Edd} values lie instead in an intermediate range between FRI-LERGs and FRII-HERGs/BLRGs. This result is quantified in Table 5.1, where the Kolmogorv Smirnov test outputs are listed for different couples of subsamples.

SAMPLES	P_{KS}
FRII-LERGs vs FRII-HERGs/BLRGs	1.2×10^{-6}
FRII-LERGs vs FRI-LERGs	1.0×10^{-3}

Table 5.1: L_{ion}/L_{Edd} Kolmogorov-Smirnov test results.

5.1.2 L_X as a proxy of the accretion rate

X-ray radiation comes from very inner regions of the AGN and therefore is considered a powerful tracer of the AGN activity. When a histogram of the unabsorbed X-ray luminosity in the 2-10 keV band is produced for the three classes of studied radio galaxies (Figure 5.4), the same trend for $L_{[OIII]}$ is observed, corroborating the idea that the nuclear activity is inherently different in FRI-LERGs, FRII-LERGs and FRII-HERGs/BLRGs. FRII-LERGs are a factor of 10 fainter than the other FRIIs. The median values of their X-ray luminosities are 42.7 and 43.8 erg s^{-1}, respectively. A Kolmogorov-Smirnov test indicates a probability of 99.2% that the FRII classes are different. For instance, FRI-LERGs are the less luminous group with a L_X median value of 40.7 erg s^{-1}. A TWOST test applied to LERGs of different radio morphologies confirms the bimodal distribution of the two classes with a probability higher than 99.9%. Again FRII-LERGs seem to have intermediate properties between FRIs and FRIIs with high-excitation optical lines.

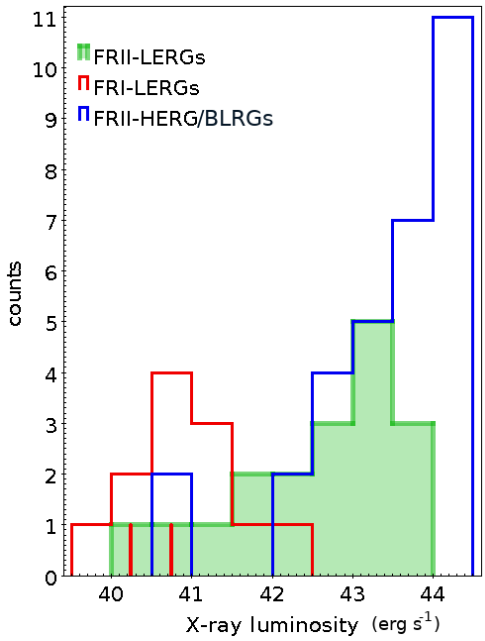

Figure 5.4: FRI-LERGs, FRII-LERGs and FRII-HERGs/BLRGs in the 2-10 keV band in units of erg s^{-1} vs. number of sources. Color-coding is the same applied to the previous. The three distributions appear to differ both in mean values and in range extension: the FRIs have luminosity values lower than $\approx 10^{42}$ erg s^{-1}, the FRII-HERGs/BLRGs range between 10^{42} and 10^{44} erg s^{-1} (with only two exceptions), and the FRII-LERGs occupy an intermediate vast range of values, spanning from 10^{40} to 10^{44} erg s^{-1}. Red vertical lines are upper-limits.

5.1.3 Dust and gas in the nuclear environment

Unlike the dust that is related either to the NLRs or obscuring structures in the galaxy, the gas column densities, estimated from the X-ray spectra, carry out information on the circumnuclear environment directly from the subparsec scales. In Table 5.2 the N_H values for each population are reported. Also this observable is in line with the previous ones discussed above.

Looking at the Figure 5.5, the difference between the FRII classes is evident: HERGs/BLRGs are clearly more obscured with a mean N_H value of $\sim 10^{23}$ cm^{-2}. Their N_H distributions differ significantly ($P_{TS} = 1 \times 10^{-4}$).

FRII-LERGs are partially overlapped to the FRIs that peaks at lower N_H values. A Kolmogorov-Smirnov test (without the upper limits) provides a probability of 95% that the distributions are different. If upper limits are considered, the TWOST test provides a probability of $P_{TWOST} = 6 \times 10^{-2}$, slightly above the threshold adopted in this work to reject the hypothesis that the two data sets come from the same distribution. There is a marginal indication that the quantity of obscuring matter (in form of gas) is decreasing from FRII-HERGs/BLRGs to FRI-LERGs, with FRII-LERGs in between.

In Figure 5.6, the dust and gas information, discussed in this Section, is summarized. The intrinsic absorption is plotted against the reddening (E(B-V)). This simply traces the gas and dust distributions in the studied samples of radio galaxies on different spatial scales. The curve plotted in Figure 5.6 shows the expected values assuming a typical dust-to-gas ratio N_H/E(B-V)=5 $\times$

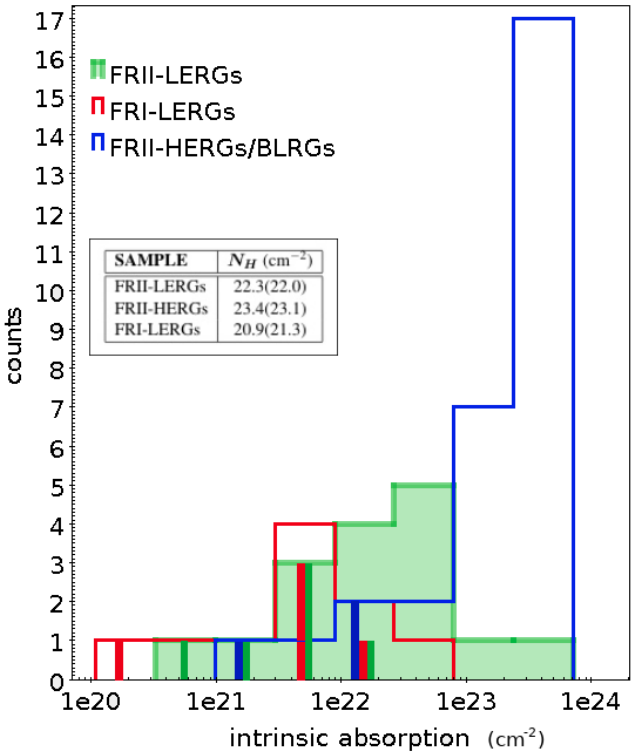

Figure 5.5: The three subsample distributions in terms of intrinsic absorption vs the percentage of objects per population. Also for this parameter FRII-LERGs (green sub-sample) are found to occupy intermediate values between FRI-LERGs (red sub-sample), which are located at lower values, and FRII-HERGs/BLRGs (blue subsample), whose distribution peaks above 10^{23} cm^{-2}. The inbox reports the mean and median values for every distribution. The vertical lines represent the upper-limits values of the samples: 5 for FRI-LERGs (in red), 6 for FRII-LERGs (in green) and 3 for FRII-HERGs/BLRGs (in blue).

10^{21} atoms cm^{-2} mag^{-1}.

Three considerations can be drawn:

- none of the FRI-LERGs has E(B-V) value lower than 0.2, and the majority of them are near or below the dust-to-gas ratio curve;
- FRII-HERG/BLRGs occupy the left upper corner of the diagram (i.e. they have high N_H and low E(B-V) values);
- FRII-LERGs are less affected by dust than FRIs and less obscured by gas than the other FRIIs.

FRIs are poor of gas but rich in dust in the NLR and beyond. This is in agreement with HST images that often show unobscured cores and dust lanes on galactic scales (Martel et al. [1999]). The dust in FRIIs, if present, should be within the NLR. If gas and dust are mixed, as expected, the observed large amount of gas indicates that the obscuring screen is mainly concentrated near the black hole.

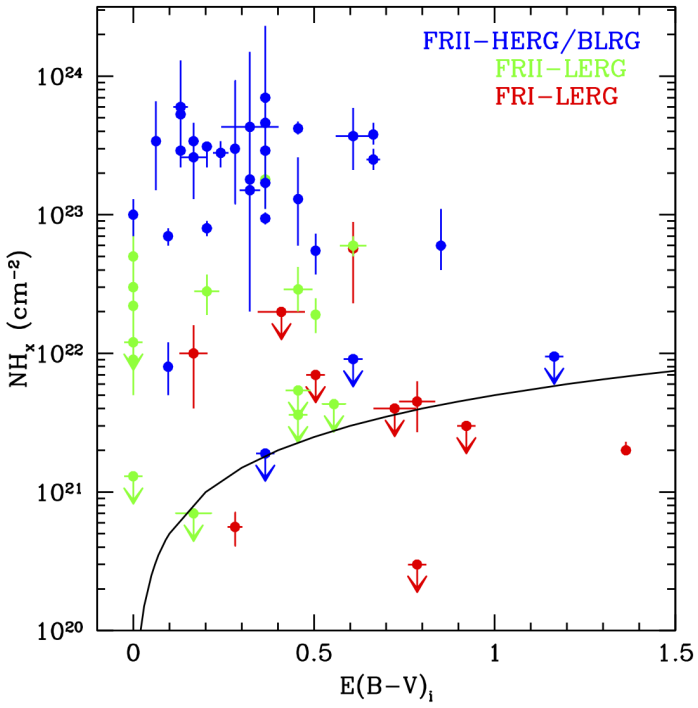

Figure 5.6: Column density (NH_x), as obtained by the X-ray analysis, plotted versus the intrinsic reddening, as measured by the optical Balmer decrement, for different classes of FRIIs and FRIs. The black curve represents the expected N_H value assuming a dust to gas ratio N_H/E(B-V)=5×10^{21} atoms cm^{-2} mag^{-1}.

5.2 Conclusions and future perspectives

The comparison of the luminosities, accretion rates, and intrinsic nuclear absorption between the three examined classes of sources (FRI-LERGs, FRII-LERGs, FRII-HERG/BLRGs) have solidly established that FRII-LERGs have intermediate properties. The measurement of moderate gas column densities in FRII-LERGs (with the exception of 3C 173.1, 3C 353 and 3C 460), combined with a modest dust reddening, enables us to **directly reject the first scenario** (see Section 5.1), in which FRII-LERGs are highly obscured versions of classical powerful FRIIs. At the same time, my X-ray analysis separates FRII-LERGs from classic low-power FRIs, which generally miss a cold-gas component in their nuclear regions, i.e the "torus" as defined in the unified scheme for AGN, and are thought to be fed mainly by hot gas. Moreover, and most interestingly, this moderate amount of cold gas seems to be associated with moderate luminosities and accretion rates in FRII/LERGs, with values which are again intermediate between classic FRIs and FRIIs. Then, the question to ask is: do FRII-LERGs form an entirely different class of sources or do they represent an evolutionary, intermediate stage between FRII-HERGs/BLRGs and FRI-LERGs?

One possibility is that the nuclei of FRII/LERGs, while not as powerful as in classic FRIIs, can still form FRII morphologies due, for instance, to **favorable environmental conditions**. Several

studies, in literature, identify the environment as the fundamental ingredient for the origin of the FRI/FRII dichotomy. On the one hand, Gendre et al. [2013], by considering the radio and optical properties of RGs, demonstrated that the relation between radio morphology and accretion mode is complex and the environment plays an important role. Miraghaei and Best [2017] explained the FR dichotomy in terms of 'extrinsic' parameters, i.e. jet disruption by interstellar medium and intergalactic medium; the very existence of sources with mixed morphologies [the so-called HYMORS, Gopal-Krishna and Wiita, 2000a], FRI in one side and FRII in the other, should be most likely explained by asymmetries in the ambient medium.

On the other hand, a link between the accretion properties and the power of the produced jets is certainly expected, based on both theoretical arguments [e.g., Blandford and Znajek, 1977, Sikora et al., 2007] and observational works [e.g., Allen et al., 2006, Ghisellini et al., 2014]. Since the FRII/LERGs in my sample accrete at lower rates than classic FRIIs, I would expect their jets to be correspondingly less powerful. Estimating the actual energy content of jets, which is mostly in the form of kinetic power, is a difficult task, and different results can be obtained depending on which method is adopted [see e.g., Pjanka et al., 2017]. If, as it is generally assumed, I consider the radio power as a valid predictor of the total jet power [e.g., Cavagnolo et al., 2010], then I do not expect the FRII-LERGs and FRII-HERGs in my sample to have a different distribution of jet powers. Indeed, as shown in Chapter 3, Fig. 3.3, the distributions of the extended radio luminosities in these two classes are substantially overlapping. This problem does not arise if I hypothesize that **the large-scale radio structures are the heritage of a past AGN activity with higher efficiency**. Since X-ray observations can penetrate the innermost nuclear regions of the AGN, the properties I infer describe the present activity of the AGN. If the nuclear power has recently decreased due, for instance, to a depletion of the cold gas reservoir, it is plausible to think that this information has not yet reached the large-scales radio structures, which are formed at kilo-parsec distances from the central engine. Indeed, a direct relation between the amount of cold gas and the accretion rate is exactly what I observe in my sample. This evolutionary scenario is supported by a recent analysis of a large sample of low-redshift and low-luminosity FRII objects [Capetti et al., 2017], which showed that the roughly one-to-one correspondence between FRII morphology and powerful nuclei is not verified for this large population in the local universe. On the contrary, most of the FRIIs in the catalog compiled by Capetti et al. [2017] are classified as LERGs. This could suggest that the local FRIIs are "starved", i.e., they now miss the fueling cold material that made them shine in the past. **In conclusion, my results are especially in agreement with the evolutionary scenario.**

To consolidate this conclusion, further analyses will be necessary in the future. For instance, it would be particularly instructive to extend this study to high redshift sources, exploring other catalogues, like the 3CRR, for which optical and radio classifications are available up to redshift 2.

Since the intrinsic gas column density is a fundamental parameter to test the evolutionary scenario, it would also be important to cross-check my results with those obtained through other satellites, like XMM-Newton and NuSTAR. The latter telescope is especially suited for the study of obscured sources given the larger energy band in which it operates (3-80 keV), so it can better constrain the N_H parameter.

To supplement my results, a study of the cold molecular gas (CO) content and properties will be relevant as well to verify that the nuclear regions in the different types of sources actually harbor different masses of cold gas.

Finally, a high resolution radio analysis of the FRII-LERG jets on parsec scales, combined with multi-frequency data, would be crucial to test the connection between accretion and jet production. Active nuclei accreting at intermediate rates should produce, at present, jets of intermediate power. Modeling of the spectral energy distribution of such jets should then place them between FRIs/BLLacs and FRIIs/FSRQs.

Appendix A

FRII-LERGs: radio properties

In the following, I report some notes on individual sources in the FRII-LERG subsample based on radio studies, and I present interferometric or single-telescope radio images found in literature. In some images, polarization vectors are also overlaid on the total intensity map.

- 3C88 - The source shows two symmetric lobes typical of FRII radio galaxies (Fig. A.1).
- 3C132 - This source has a clear FRII morphology with strongly edge-brightened lobes of similar luminosity and faint jet emission (Fig. A.2).
- 3C153 - This small radio galaxy (with size of $\sim$25 kpc) presents no visible nuclear component and two highly asymmetric lobes (Fig. A.3). It was classified as a Compact Steep Spectrum (CSS) by Akujor et al. [1991].
- 3C165 - This is a classical double source with FRII morphology (Fig. A.4).
- 3C166 - The double radio structure is characterized by remarkably dissimilar lobes (Fig. A.5), the southern one showing a much more prominent hotspot and being much more depolarized [Spangler and Bridle, 1982]. These elements may be indicative of asymmetries in the ambient medium. 3C166 presents a one-sided and polarized jet on parsec scales [e.g., Taylor et al., 2001], suggesting that the viewing angle of this radio galaxy is not very large.
- 3C173.1 - The source presents a prominent core, also detected on parsec scales with VLBI [Yuan et al., 2018], and edge-brightened lobes which are slightly misaligned with respect to the core (Fig. A.6).
- 3C196.1 - The source shows a compact one-sided radio structure lying within the host galaxy (Fig. A.7). The elliptical host galaxy as seen in the near-infrared and in the optical is strongly elongated along the axis of the radio emission [Madrid et al., 2006, and references therein].
- 3C213.1 - The double radio source is immersed in a large halo of diffuse emission (Fig. A.8). It is classified as a Compact Steep Spectrum [Akujor and Garrington, 1995].
- 3C236 - With an extend of $\sim$4.5 Mpc, this is the largest radio galaxy known (Fig. A.9). Observations at milli-arcseconds resolution of the central core provide evidence for restarted

activity, revealing the formation of a new small radio galaxy with size of $\sim$2 kpc [Fig. A.10 Schilizzi et al., 2001].

- 3C288 - While having the luminosity of an FRII, this source presents an edge-darkened radio structure more typical of FRI objects (Fig. A.11). The peculiarities of this radio galaxy were discussed by Bridle et al. [1989].

- 3C310 - As in the case of 3C288, also this source has a high power but the morphology of an FRI (Fig. A.12). A one-sided core-jet structure was detected on parsec scales by Giovannini et al. [2005].

- 3C326 - This large and powerful source has a peculiar morphology (Fig. A.13). The radio structure is produced in a system of two companion galaxies, and the location of the nuclear region is uncertain [see e.g., Rawlings et al., 1990].

- 3C349 - This is a symmetric double source with prominent hotspots (Fig. A.14).

- 3C353 - This is a well studied powerful source with FRII morphology (Fig. A.15). A detailed analysis of its relativistic jets was presented by Swain et al. [1998].

- 3C357 - This double radio source is characterized by bright hotspots which are misaligned with respect to the nuclear regions (Fig. A.16). This could be due to a deviation of the jet direction in both sides.

- 3C388 - This FRII source is characterized by an asymmetric radio structure, since it shows a bright jet-like feature in the western lobe but not in the eastern one (Fig. A.17). Burns et al. [1982] have interpreted this as an evidence for intermittent jet activity. A one-sided core-jet structure was detected on parsec scales by Giovannini et al. [2005].

- 3C401 - This double source shows a bright bending jet feature propagating through the south-western lobe (Fig. A.18). The radio core is resolved on parsec scales in a one-sided core-jet structure [Yuan et al., 2018]. Based on an infrared study, Chiaberge et al. [2005] suggested that the spectral properties of the jet in 3C401 are intermediate between FRI and FRII objects.

- 3C430 - This is classic powerful double source with bright hotspots (Fig. A.19).

- 3C460 - This FRII radio galaxy is not well studied in the radio. Based on unpublished results, McCarthy et al. [1995] define its double radio structure (Fig. A.20) highly asymmetric.

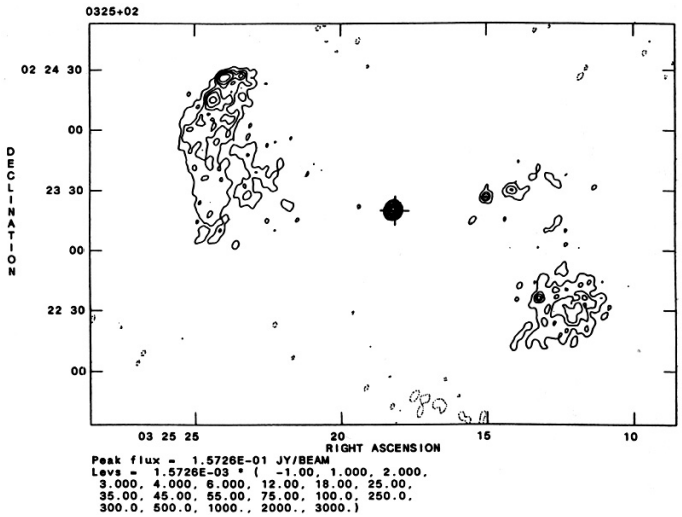

Figure A.1: VLA image of 3C88 at 5 GHz [Morganti et al., 1993a].

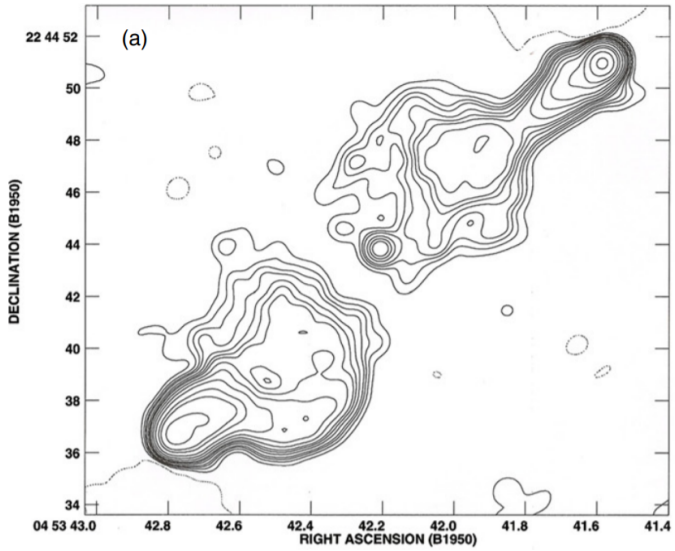

Figure A.2: VLA image of 3C132 at 8.4 GHz [Fernini, 2014].

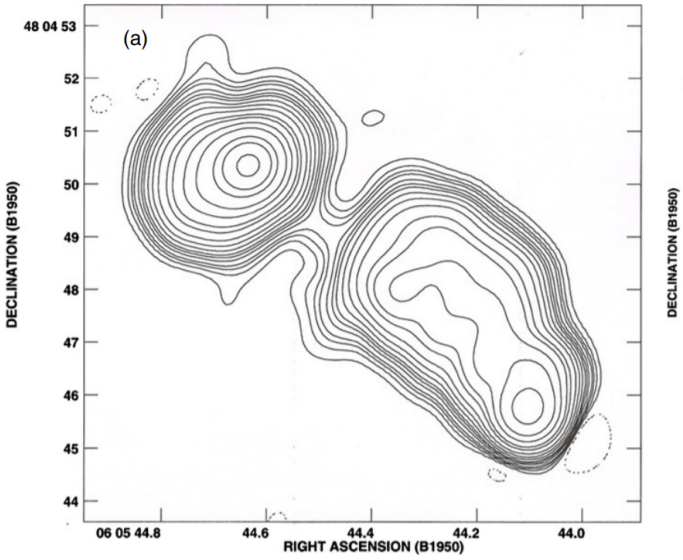

Figure A.3: VLA image of 3C153 at 8.4 GHz [Fernini, 2014]

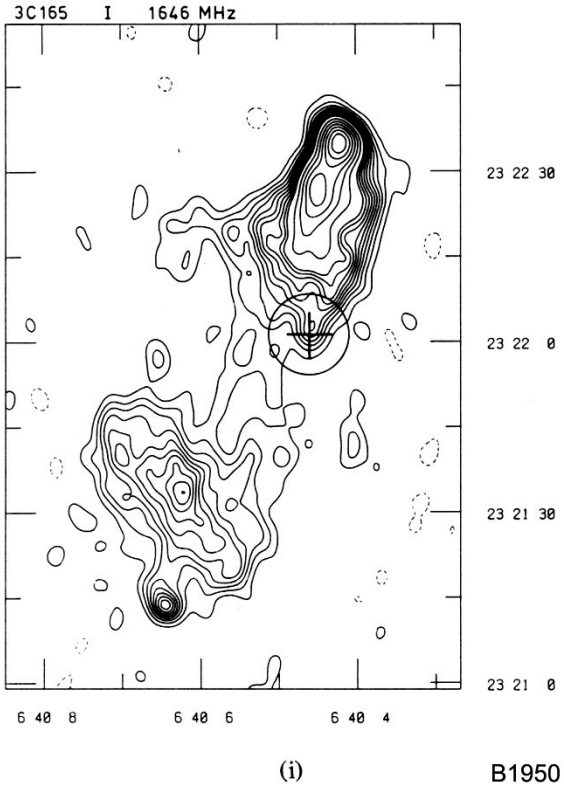

Figure A.4: VLA image of 3C165 at 1.6 GHz [Leahy and Williams, 1984].

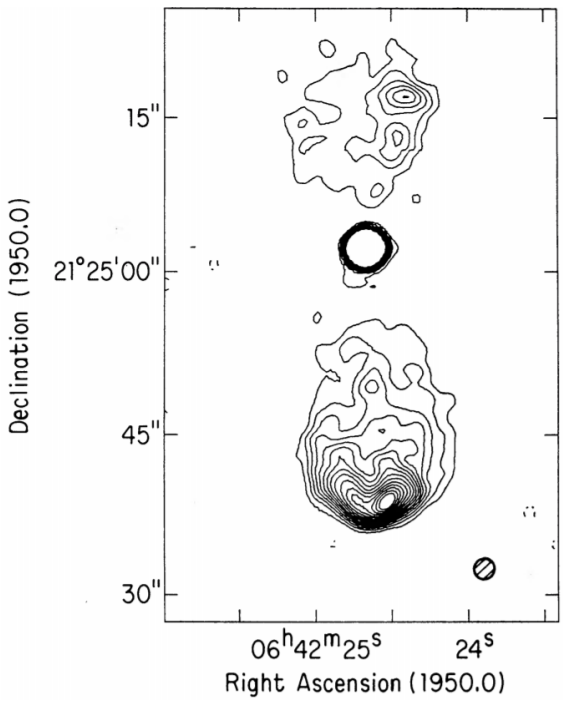

Figure A.5: VLA image of 3C166 at 5 GHz [Spangler and Bridle, 1982].

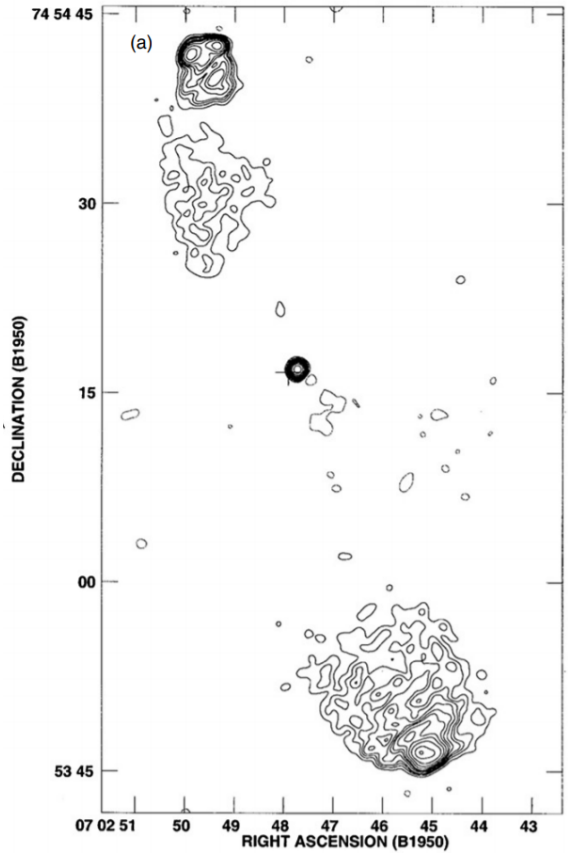

Figure A.6: VLA image of 3C173.1 at 8 GHz [Fernini, 2014].

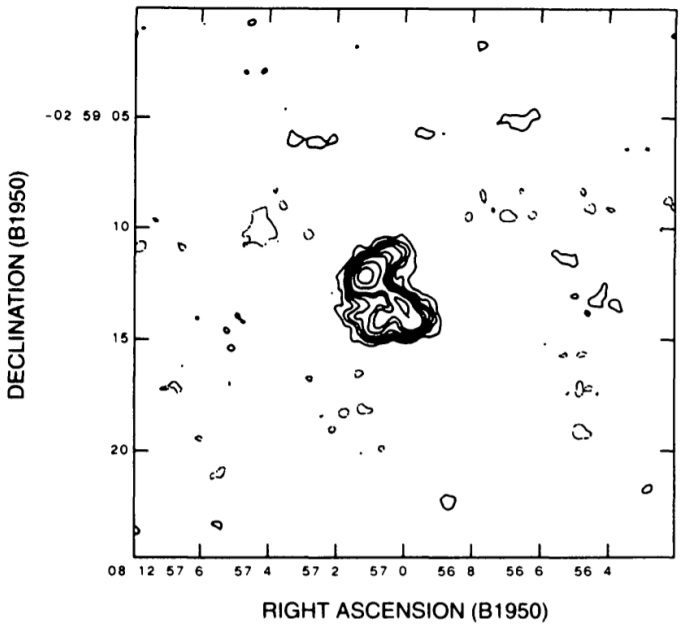

Figure A.7: VLA image of 3C196.1 at 5 GHz [Neff et al., 1995].

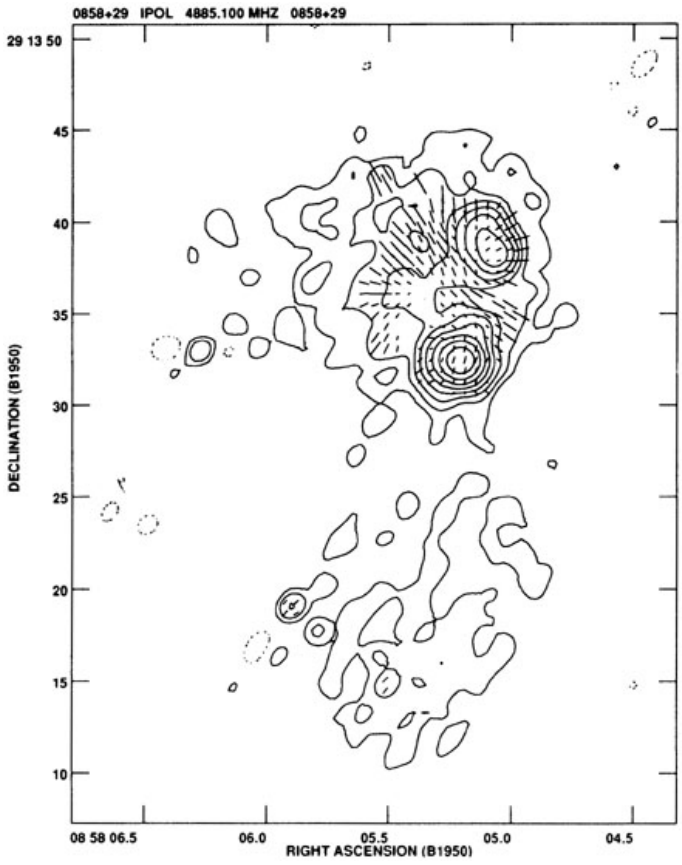

Figure A.8: VLA image of 3C213.1 at 5 GHz [Akujor and Garrington, 1995].

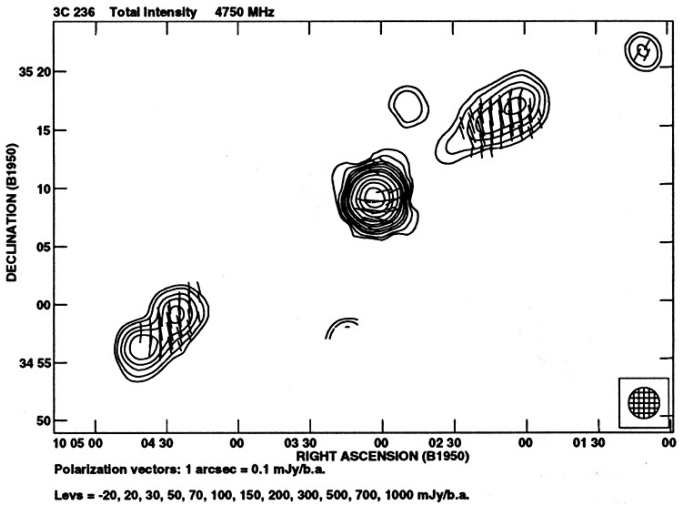

Figure A.9: Effelsberg image of 3C236 at 5 GHz [Mack et al., 1997].

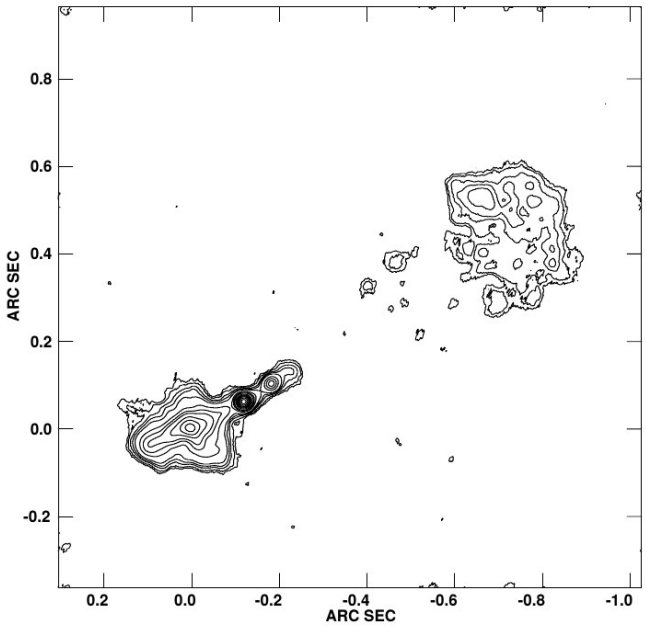

Figure A.10: VLBI image of 3C236 at 1.4 GHz [Schilizzi et al., 2001].

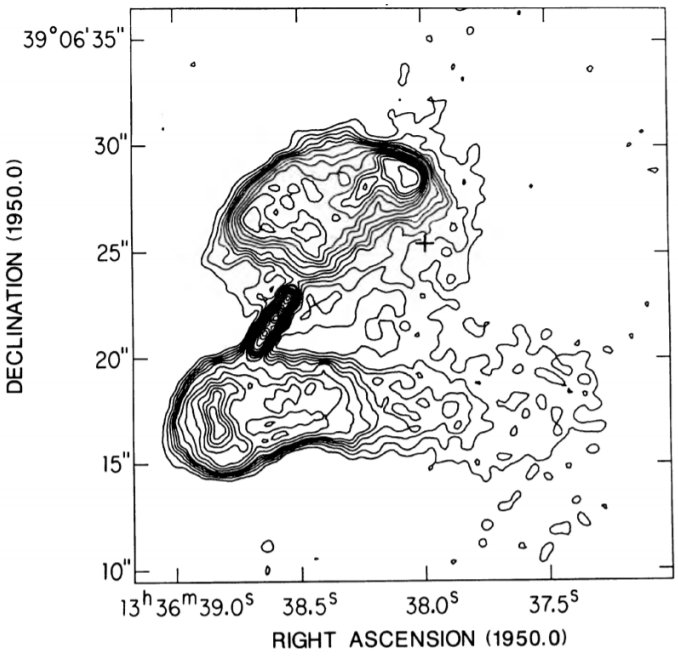

Figure A.11: VLA image of 3C288 at 5 GHz [Bridle et al., 1989].

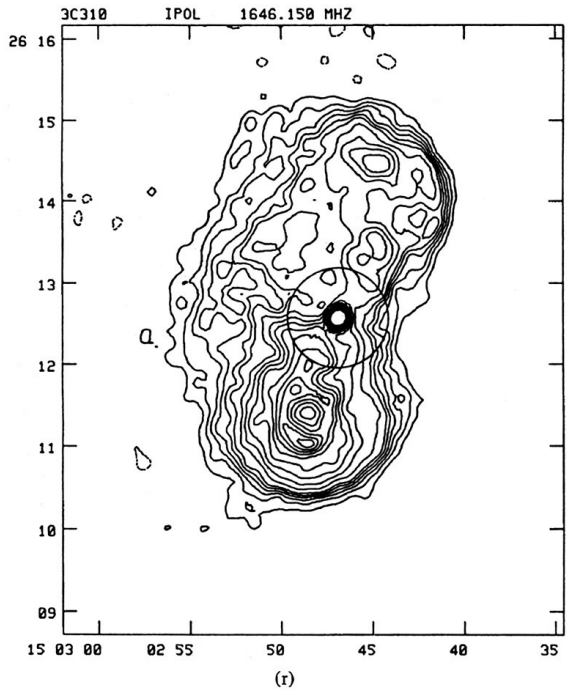

Figure A.12: VLA image of 3C310 at 1.6 GHz [Leahy and Williams, 1984].

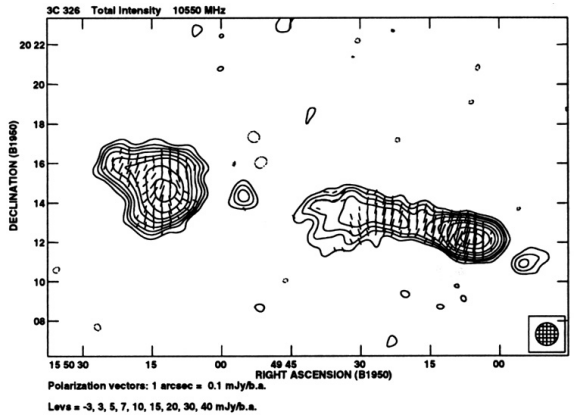

Figure A.13: Effelsberg image of 3C310 at 10 GHz [Mack et al., 1997].

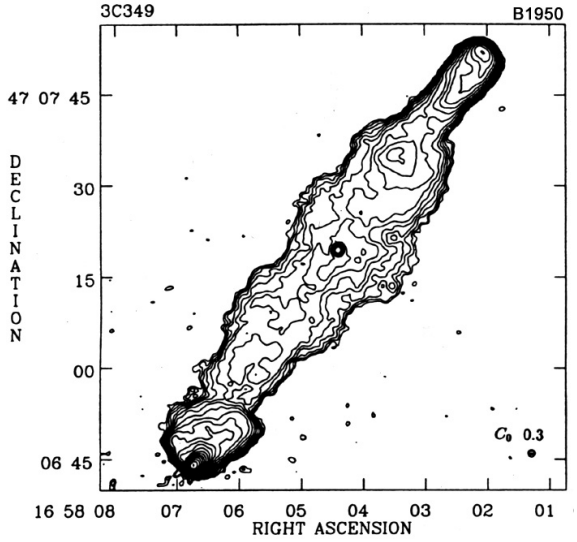

Figure A.14: VLA image of 3C349 at 1.6 GHz [Leahy and Perley, 1991].

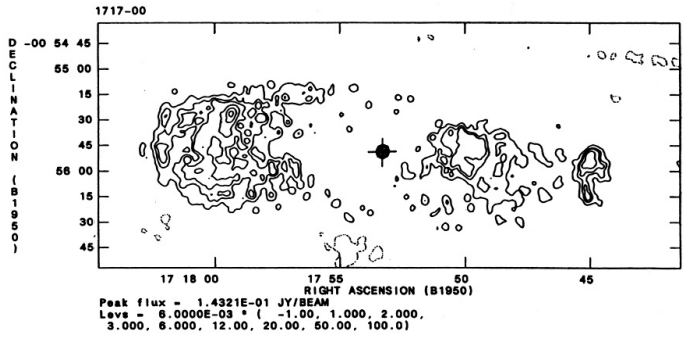

Figure A.15: VLA image of 3C353 at 5 GHz [Morganti et al., 1993a].

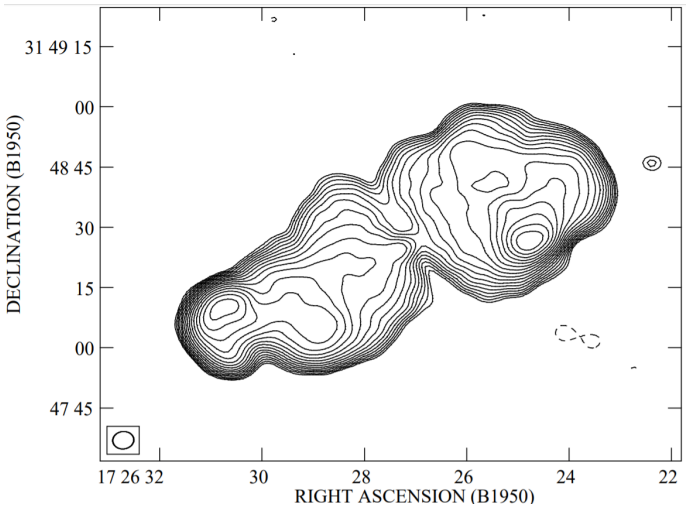

Figure A.16: VLA image of 3C357 at 1.4 GHz [Harvanek and Hardcastle, 1998].

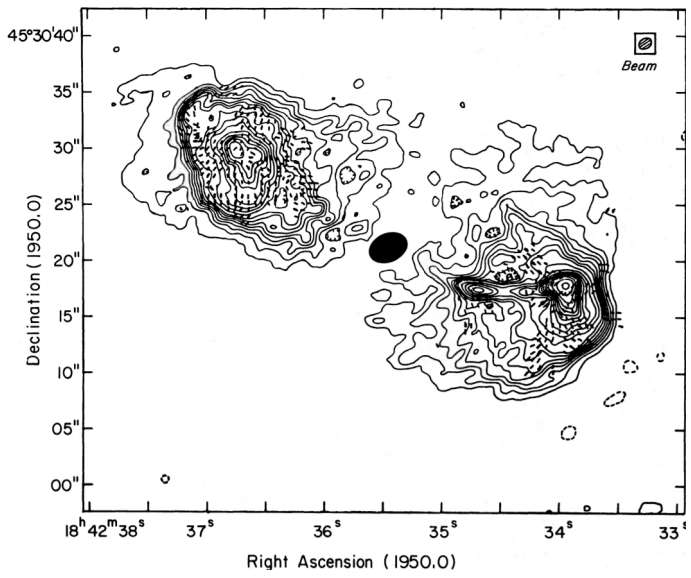

Figure A.17: VLA image of 3C388 at 5 GHz [Burns et al., 1982].

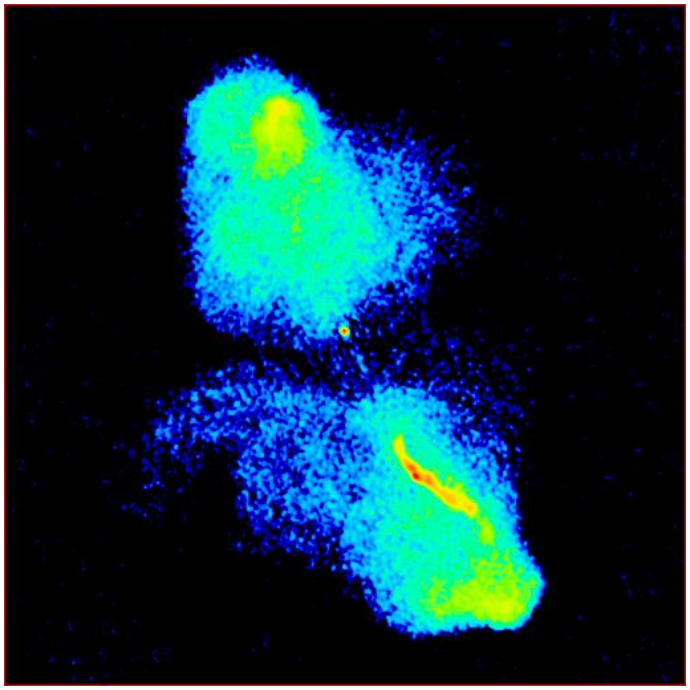

Figure A.18: VLA image of 3C401 at 1.4 GHz. Credits: R. A. Laing & J. P. Leahy, (unpublished).

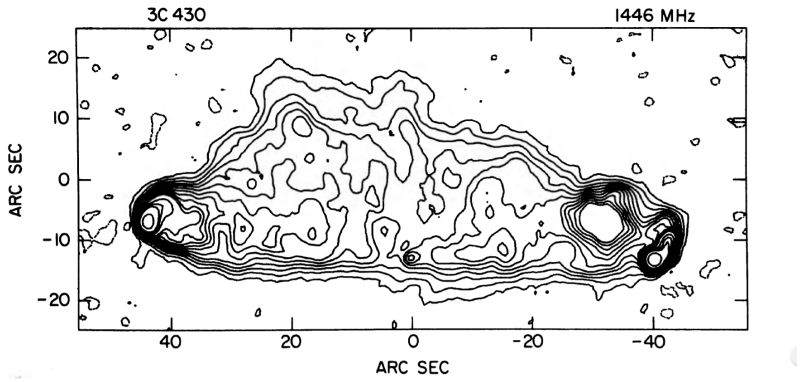

Figure A.19: VLA image of 3C430 at 1.4 GHz [Spangler et al., 1984].

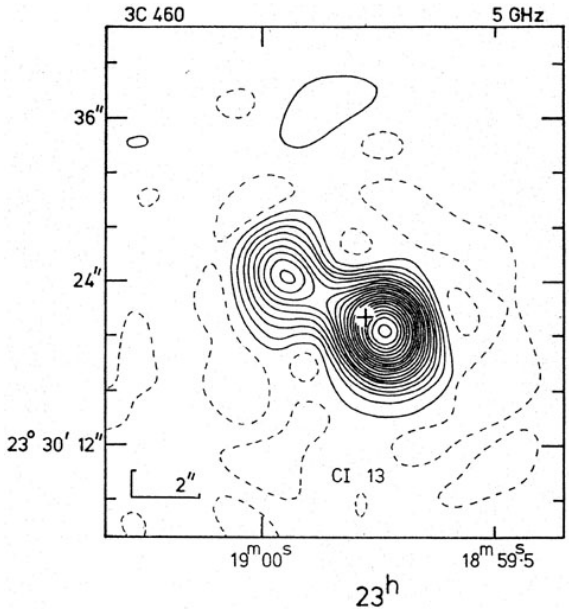

Figure A.20: Cambridge telescope image of 3C460 at 5 GHz [Pooley and Henbest, 1974].

Appendix B

FRII-LERGs: X-ray images of extended sources

Chandra images of extended FRII-LERGs in the 0.3-7 keV energy band are shown. When available, radio contours from VLA data at 1.4 GHz are also superimposed (in green) to the X-ray images (except 3C 288, for which the VLA radio contours are at 5 GHz).

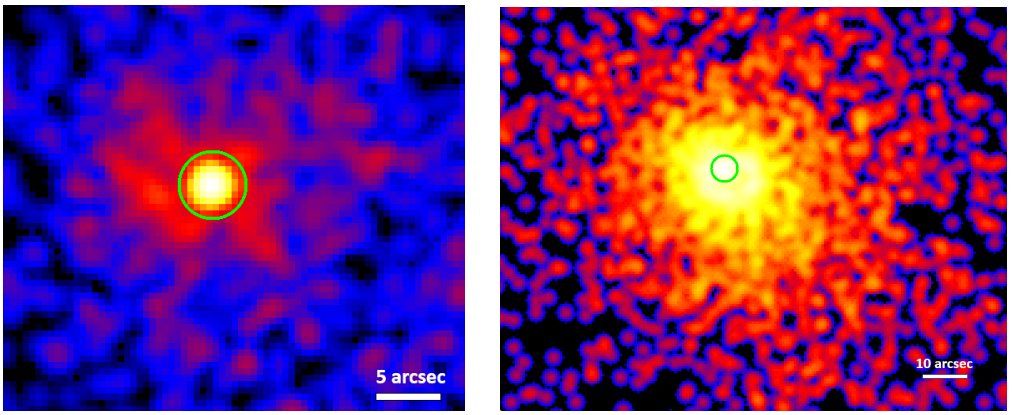

Figure B.1: *Left Panel* – **3C 88**. This radio galaxy inhabits the center of a galaxy group and produce the largest X-ray cavities ever found in a galaxy group Liu et al. 2019.The redshift is z=0.0302.
Right Panel– **3C 196.1**. It is the Brightest Cluster Galaxy (BCG) of a Cool Core Cluster (CCC) Ricci et al. 2018. They measures a core cluster temperature of about 3 keV, in agreement with my analysis (see Table 4.4). The redshift is z=0.1980.

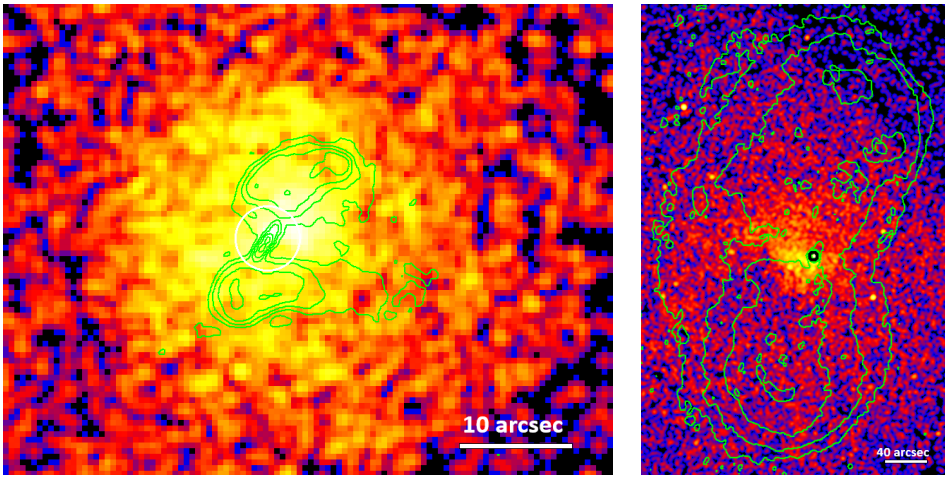

Figure B.2: *Left Panel* – **3C 288**. (z=0.2460) It was found by Lal et al. [2010] to reside in the center of a poor not-CC GC. They support the hypothesis that the AGN is strongly interacting with its environment (because of the lack of cool gas in the center, the lack of any evidence of recent merger both on small and large scales and the peculiar FRI/FRII radio morphology). They found an ICM gas temperature of about 3 keV extending to about 400 kpc . *Right Panel* – **3C 310**. (z=0.0535) It is the central galaxy of a pure cluster [Kraft et al., 2012], hosted by a BGC, with a temperature of about 3 keV at a distance between 100 and 180 kpc (at which a shock occurs) .

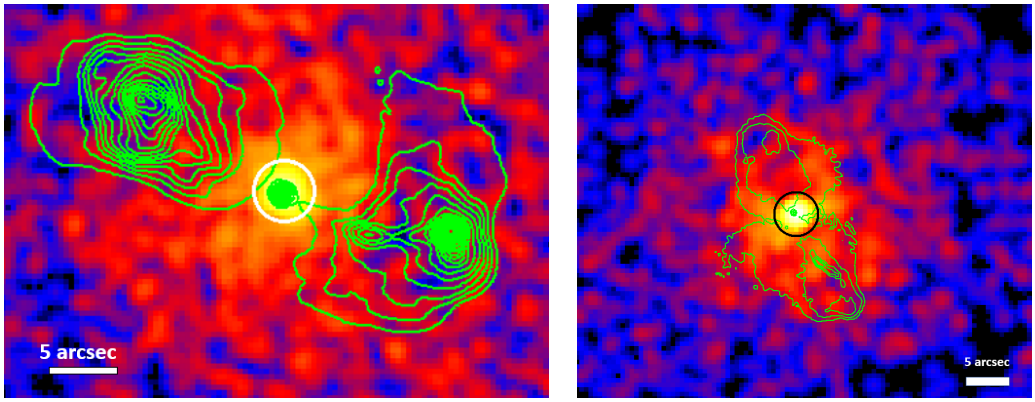

Figure B.3: *Left Panel* – **3C 388**. (z=0.0917) It resides in the center of a small cluster environment with an ICM temperature of about 3.5 keV and a cool core probably heated by a nuclear outburst. The host galaxy is the cD of the cluster Kraft et al. [2006] . *Right Panel* – **3C 401**. (z=0.2011) It is in the center of a GC with ICM mean temperature of 2.9 keV. Reynolds et al. [2005] proposed both a thermal hot core ($T \approx 4.9$ keV) and a simple power law model (which is the model assumed in this work) because statistically indistinguishable .

Appendix C

X-ray spectra

All the FRII-LERGs best-fit X-ray spectra are reported in this Section.

3C88 z=0.0302 model:phabs*zpcfabs*po

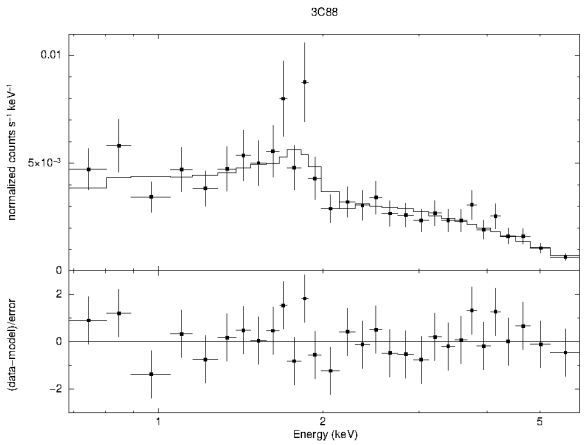

Figure C.1: The upper window shows data grouped in bins in units of counts s^{-1} keV^{-1} vs observed-frame energy in keV. In the bottom window the residuals (data-model/error) are shown.

3C132 z=0.2140 model:phabs*zphabs*po

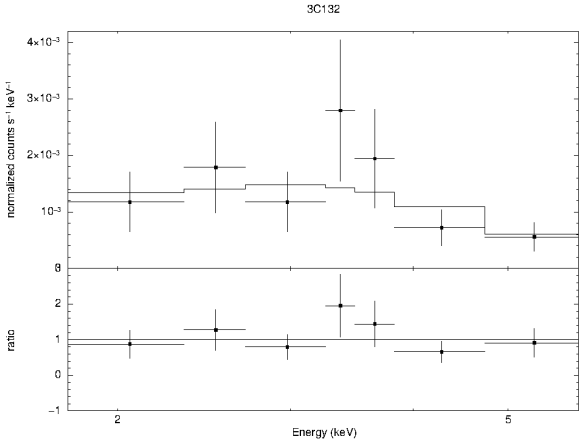

Figure C.2: The upper window shows data grouped in bins in units of counts s^{-1} keV^{-1} vs observed-frame energy in keV. In the bottom window the ratio between data and model is shown (Poissonian statistics).

3C165 z=0.2957 model:phabs*zphabs*po

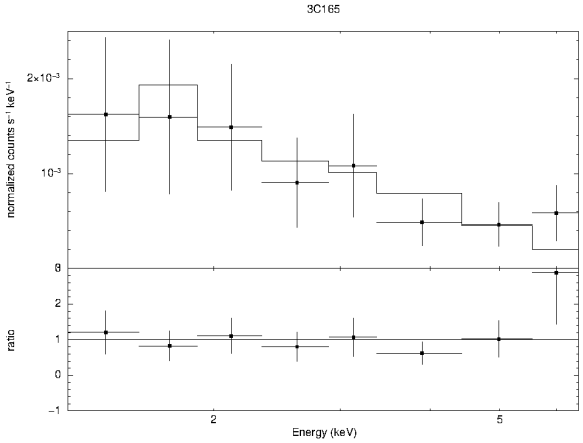

Figure C.3: The upper window shows data grouped in bins in units of counts s^{-1} keV^{-1} vs observed-frame energy in keV. In the bottom window the ratio between data and model is shown (Poissonian statistics).

3C166 z=0.2449 model:phabs*po

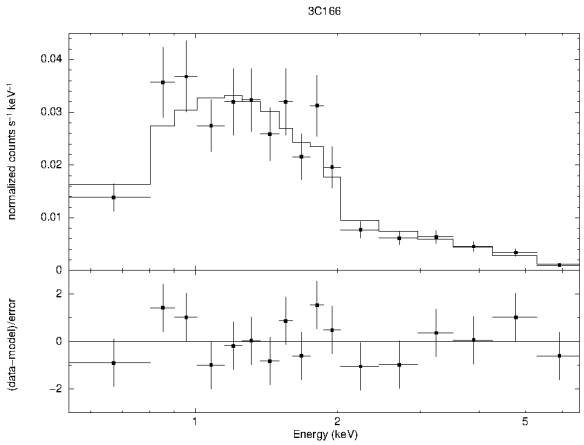

Figure C.4: The upper window shows data grouped in bins in units of counts s^{-1} keV^{-1} vs observed-frame energy in keV. In the bottom window the residuals (data-model/error) are shown.

3C173.1 z=0.2920 model:phabs*(zphabs*(po+zgauss)+po)

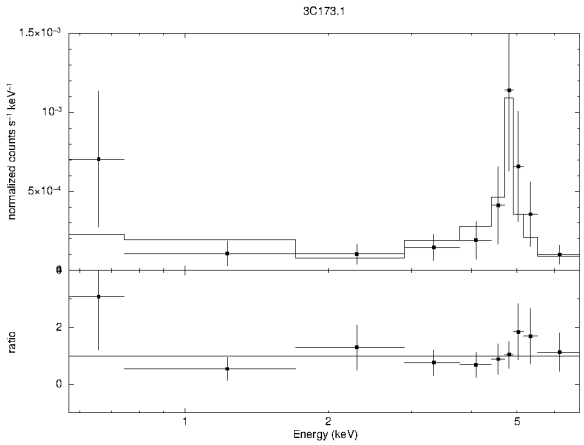

Figure C.5: The upper window shows data grouped in bins in units of counts s^{-1} keV^{-1} vs observed-frame energy in keV. In the bottom window the ratio between data and model is shown (Poissonian statistics).

3C196.1 z=0.1980 model:phabs*mekal

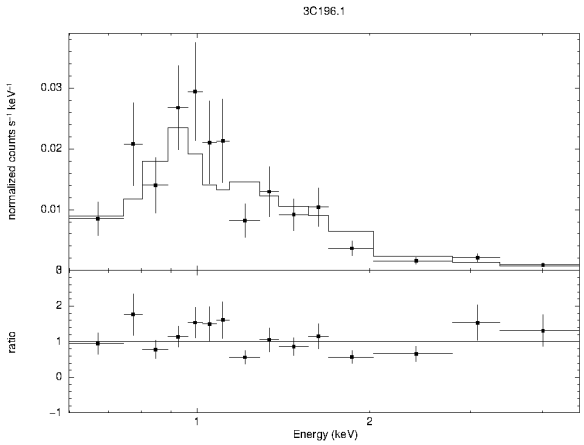

Figure C.6: The upper window shows data grouped in bins in units of counts s^{-1} keV^{-1} vs observed-frame energy in keV. In the bottom window the ratio between data and model is shown (Poissonian statistics).

3C213.1 z=0.1939 model:phabs*po

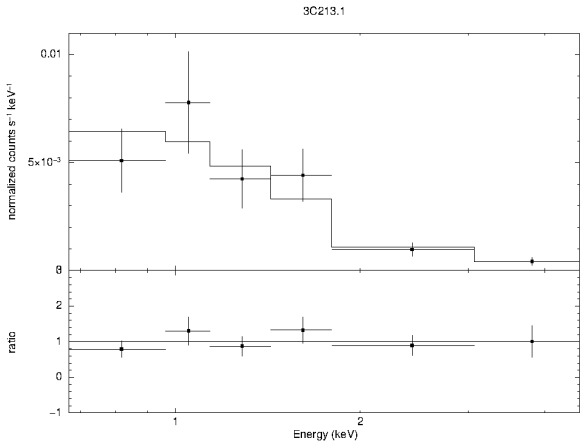

Figure C.7: The upper window shows data grouped in bins in units of counts s^{-1} keV^{-1} vs observed-frame energy in keV. In the bottom window the ratio between data and model is shown (Poissonian statistics).

3C236 z=0.1005 model:phabs*zphabs*po

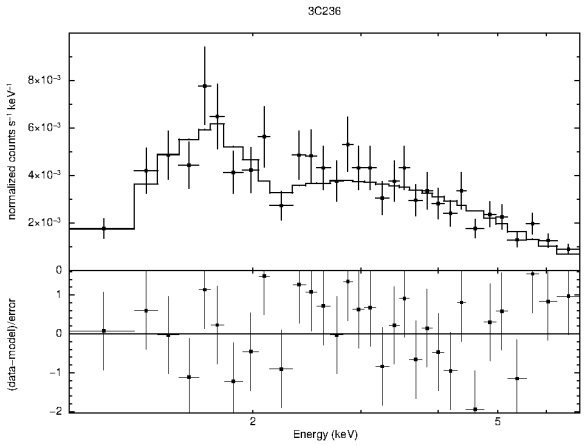

Figure C.8: The upper window shows data grouped in bins in units of counts s^{-1} keV^{-1} vs observed-frame energy in keV. In the bottom window the residuals (data-model/error) are shown.

3C288 z=0.2460 model:phabs*po

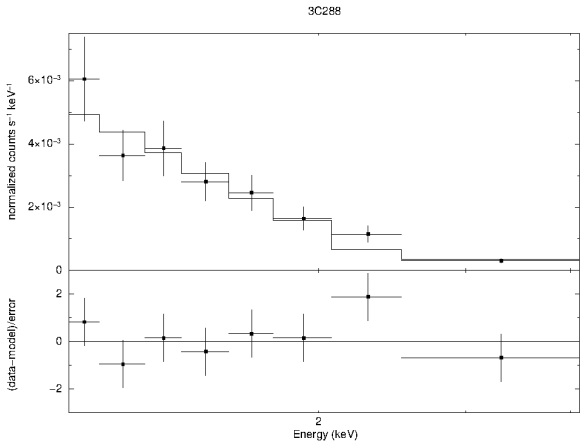

Figure C.9: The upper window shows data grouped in bins in units of counts s^{-1} keV^{-1} vs observed-frame energy in keV. In the bottom window the residuals (data-model/error) are shown.

3C310 z=0.0535 model:phabs*(mekal+po)

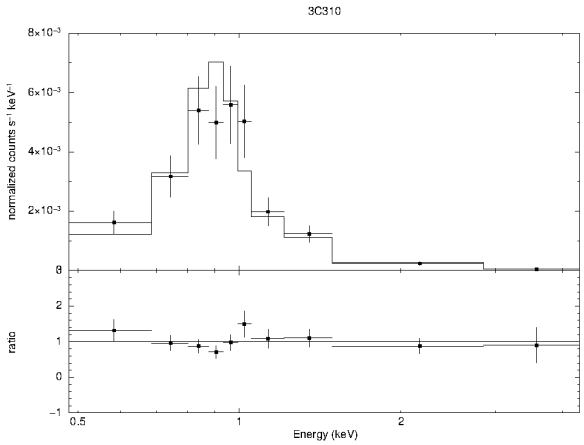

Figure C.10: The upper window shows data grouped in bins in units of counts s^{-1} keV^{-1} vs observed-frame energy in keV. In the bottom window the ratio between data and model is shown (Poissonian statistics).

3C326 z=0.0895 model:phabs*zphabs*po

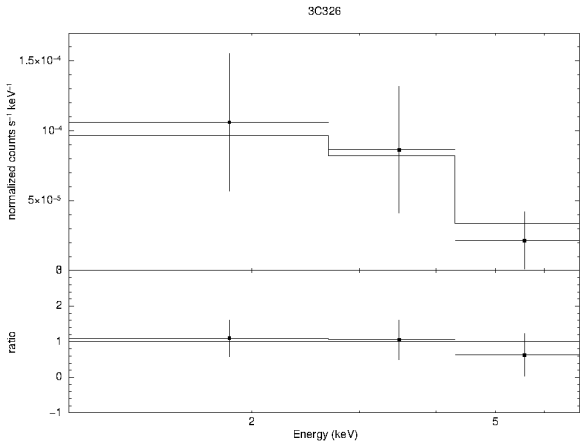

Figure C.11: The upper window shows data grouped in bins in units of counts s^{-1} keV^{-1} vs observed-frame energy in keV. In the bottom window the ratio between data and model is shown (Poissonian statistics).

3C349 z=0.2050 model:phabs*zphabs*po

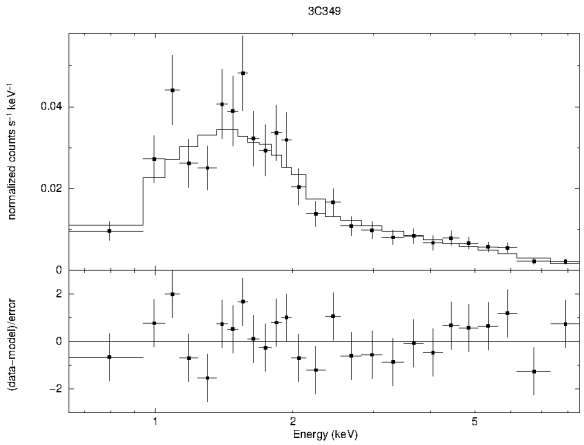

Figure C.12: The upper window shows data grouped in bins in units of counts s^{-1} keV^{-1} vs observed-frame energy in keV. In the bottom window the residuals (data-model/error) are shown.

3C353 z=0.0304 model:phabs*(zphabs*(po+zgauss)+po)

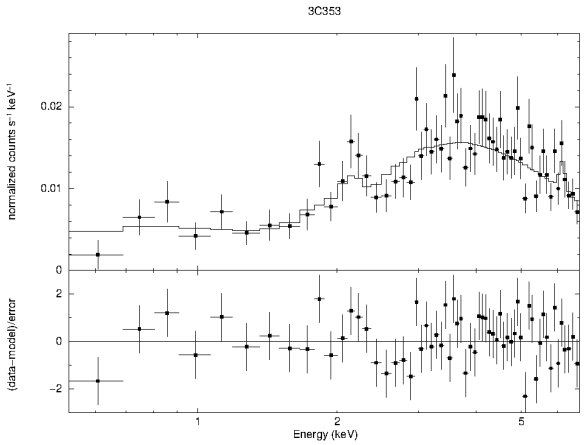

Figure C.13: The upper window shows data grouped in bins in units of counts s^{-1} keV^{-1} vs observed-frame energy in keV. In the bottom window the residuals (data-model/error) are shown.

3C357 z=0.1662 model:phabs*zpcfabs*po

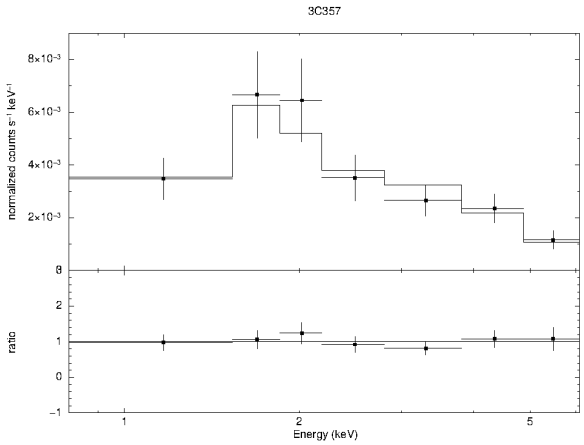

Figure C.14: The upper window shows data grouped in bins in units of counts s^{-1} keV^{-1} vs observed-frame energy in keV. In the bottom window the ratio between data and model is shown (Poissonian statistics).

3C388 z=0.0917 model:phabs*(mekal+po)

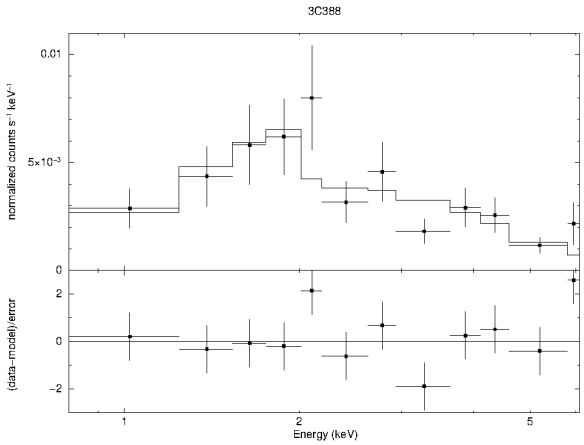

Figure C.15: The upper window shows data grouped in bins in units of counts s^{-1} keV^{-1} vs observed-frame energy in keV. In the bottom window the residuals (data-model/error) are shown.

3C401 z=0.2011 model:phabs*po

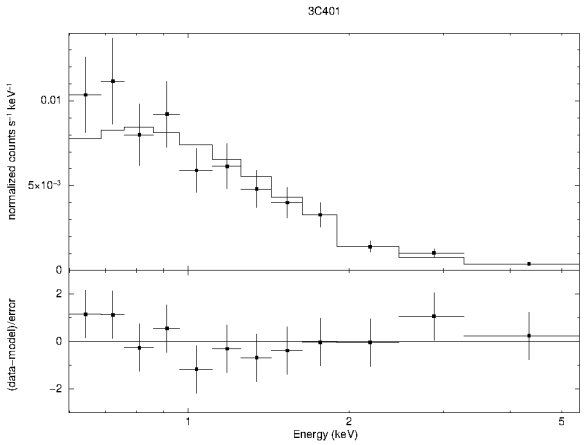

Figure C.16: The upper window shows data grouped in bins in units of counts s^{-1} keV^{-1} vs observed-frame energy in keV. In the bottom window the residuals (data-model/error) are shown.

3C460 z=0.2680 model:phabs*(zphabs*po+po)

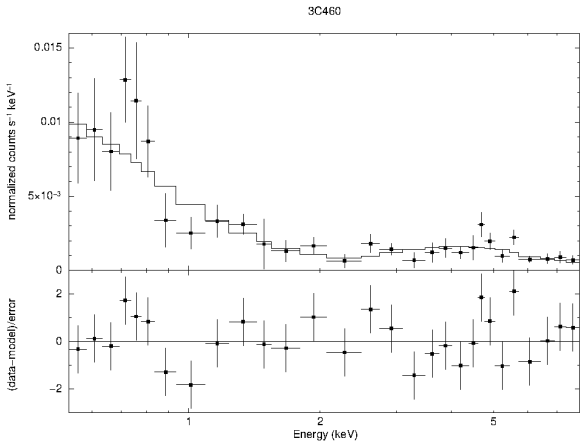

Figure C.17: The upper window shows data grouped in bins in units of counts s^{-1} keV^{-1} vs observed-frame energy in keV. In the bottom window the residuals (data-model/error) are shown.

The model abbreviations stand for:po=power law, phabs=absorption at z=0, zphabs=absorption at the source redshift, zgauss= Gaussian feature at in the source rest frame, mekal=thermal emission from hot gas and zpcfabs=partial covering factor.

List of Figures

Bibliography

A. A. Abdo, M. Ackermann, M. Ajello, W. B. Atwood, L. Baldini, J. Ballet, G. Barbiellini, D. Bastieri, B. M. Baughman, K. Bechtol, R. Bellazzini, B. Berenji, R. D. Blandford, Bloom ..., and Fermi LAT Collaboration. Fermi Gamma-Ray Imaging of a Radio Galaxy. *Science*, 328: 725, May 2010. doi: 10.1126/science.1184656.

Marek A. Abramowicz, Xingming Chen, Shoji Kato, Jean-Pierre Lasota, and Oded Regev. Thermal Equilibria of Accretion Disks. *ApJ*, 438:L37, January 1995. doi: 10.1086/187709.

M. Ackermann, M. Ajello, L. Baldini, J. Ballet, G. Barbiellini, D. Bastieri, R. Bellazzini, E. Bissaldi, R. D. Blandford, E. D. Bloom, R. Bonino, T. J. Brandt, J. Bregeon, P. Bruel, R. Buehler, S. Buson, G. A. Caliandro, R. A. Cameron, M. Caragiulo, P. A. Caraveo, E. Cavazzuti, C. Cecchi, E. Charles, A. Chekhtman, S. Cheung, C. ..., and Fermi LAT Collaboration. Fermi Large Area Telescope Detection of Extended Gamma-Ray Emission from the Radio Galaxy Fornax A. *ApJ*, 826:1, July 2016. doi: 10.3847/0004-637X/826/1/1.

C. E. Akujor and S. T. Garrington. Compact steep-spectrum sources - polarisation observations at 1.6, 4.9, 8.4 and 15 GHz. , 112:235, September 1995.

C. E. Akujor, R. E. Spencer, F. J. Zhang, R. J. Davis, I. W. A. Browne, and C. Fanti. MERLIN observations of steep-spectrum radio sources at 6 CM. *MNRAS*, 250:215–224, May 1991. doi: 10.1093/mnras/250.1.215.

S. W. Allen, R. J. H. Dunn, A. C. Fabian, G. B. Taylor, and C. S. Reynolds. The relation between accretion rate and jet power in X-ray luminous elliptical galaxies. *MNRAS*, 372:21–30, Oct 2006. doi: 10.1111/j.1365-2966.2006.10778.x.

Robert Antonucci. Unified models for active galactic nuclei and quasars. *Annual Review of Astronomy and Astrophysics*, 31:473–521, January 1993. doi: 10.1146/annurev.aa.31.090193.002353.

K. A. Arnaud. XSPEC: The First Ten Years. In George H. Jacoby and Jeannette Barnes, editors, *Astronomical Data Analysis Software and Systems V*, volume 101 of *Astronomical Society of the Pacific Conference Series*, page 17, January 1996.

Y. Avni. Energy spectra of X-ray clusters of galaxies. *ApJ*, 210:642–646, Dec 1976. doi: 10.1086/154870.

J. A. Baldwin, M. M. Phillips, and R. Terlevich. Classification parameters for the emission-line spectra of extragalactic objects. *Publications of the Astronomical Society of the Pacific*, 93: 5–19, February 1981. doi: 10.1086/130766.

B. Balmaverde, A. Capetti, and P. Grandi. The Chandra view of the 3C/FR I sample of low luminosity radio-galaxies. *A & A*, 451:35–44, May 2006. doi: 10.1051/0004-6361:20053799.

B. Balmaverde, A. Capetti, P. Grandi, E. Torresi, M. Chiaberge, J. Rodriguez Zaurin, G. R. Tremblay, D. J. Axon, S. A. Baum, G. Giovannini, P. Kharb, F. D. Macchetto, C. P. O'Dea, and W. Sparks. Extended soft X-ray emission in 3CR radio galaxies at z < 0.3: high excitation and broad line galaxies. *A & A*, 545:A143, Sep 2012. doi: 10.1051/0004-6361/201219561.

A. S. Bennett. The revised 3C catalogue of radio sources. *Memoirs of the Royal Astronomical Society*, 68:163, January 1962.

Stefano Bianchi and Matteo Guainazzi. The nature of the soft X-ray emission in obscured AGN. In Tiziana di Salvo, Gian Luca Israel, Luciano Piersant, Luciano Burderi, Giorgio Matt, Amedeo Tornambe, and Maria Teresa Menna, editors, *The Multicolored Landscape of Compact Objects and Their Explosive Origins*, volume 924 of *American Institute of Physics Conference Series*, pages 822–829, Aug 2007. doi: 10.1063/1.2774948.

Geoffrey V. Bicknell. Relativistic Jets and the Fanaroff-Riley Classification of Radio Galaxies. *The Astrophysical Journal Supplement Series*, 101:29, Nov 1995. doi: 10.1086/192232.

R. D. Blandford and R. L. Znajek. Electromagnetic extraction of energy from Kerr black holes. *MNRAS*, 179:433–456, May 1977. doi: 10.1093/mnras/179.3.433.

A. H. Bridle, E. B. Fomalont, G. G. Byrd, and M. J. Valtonen. The unusual radio galaxy 3C 288. *ApJ*, 97:674–685, March 1989. doi: 10.1086/115013.

A. M. Burgess and R. W. Hunstead. The Molonglo Southern 4 Jy Sample (MS4). I. Definition. *ApJ*, 131:100–113, January 2006a. doi: 10.1086/498677.

A. M. Burgess and R. W. Hunstead. The Molonglo Southern 4 Jy Sample (MS4). II. ATCA Imaging and Optical Identification. *ApJ*, 131:114–132, January 2006b. doi: 10.1086/498679.

J. O. Burns, W. A. Christiansen, and D. H. Hough. Multifrequency VLA observations of 3C 388 - Evidence for an intermittent jet. *ApJ*, 257:538–558, June 1982. doi: 10.1086/160010.

S. Buttiglione, A. Capetti, A. Celotti, D. J. Axon, M. Chiaberge, F. D. Macchetto, and W. B. Sparks. An optical spectroscopic survey of the 3CR sample of radio galaxies with z < 0.3. I. Presentation of the data. *A & A*, 495:1033–1060, March 2009. doi: 10.1051/0004-6361:200811102.

S. Buttiglione, A. Capetti, A. Celotti, D. J. Axon, M. Chiaberge, F. D. Macchetto, and W. B. Sparks. An optical spectroscopic survey of the 3CR sample of radio galaxies with z < 0.3 . II. Spectroscopic classes and accretion modes in radio-loud AGN. *A & A*, 509:A6, January 2010. doi: 10.1051/0004-6361/200913290.

S. Buttiglione, A. Capetti, A. Celotti, D. J. Axon, M. Chiaberge, F. D. Macchetto, and W. B. Sparks. An optical spectroscopic survey of the 3CR sample of radio galaxies with z < 0.3. III. Completing the sample. *A & A*, 525:A28, January 2011. doi: 10.1051/0004-6361/201015574.

Daniela Calzetti, Lee Armus, Ralph C. Bohlin, Anne L. Kinney, Jan Koornneef, and Thaisa Storchi-Bergmann. The Dust Content and Opacity of Actively Star-forming Galaxies. *ApJ*, 533:682–695, Apr 2000. doi: 10.1086/308692.

A. Capetti, F. Massaro, and R. D. Baldi. FRIICAT: A FIRST catalog of FR II radio galaxies. *A & A*, 601:A81, May 2017. doi: 10.1051/0004-6361/201630247.

Jason A. Cardelli, Geoffrey C. Clayton, and John S. Mathis. The Relationship between Infrared, Optical, and Ultraviolet Extinction. *ApJ*, 345:245, Oct 1989. doi: 10.1086/167900.

K. W. Cavagnolo, B. R. McNamara, P. E. J. Nulsen, C. L. Carilli, C. Jones, and L. Bîrzan. A Relationship Between AGN Jet Power and Radio Power. *ApJ*, 720:1066–1072, September 2010. doi: 10.1088/0004-637X/720/2/1066.

M. Chiaberge, W. B. Sparks, F. D. Macchetto, E. Perlman, A. Capetti, B. Balmaverde, D. Floyd, C. O'Dea, and D. J. Axon. The Infrared-dominated Jet of 3C 401. *ApJ*, 629:100–107, August 2005. doi: 10.1086/431236.

B. Czerny and B. You. Accretion in active galactic nuclei and disk-jet coupling. *Astronomische Nachrichten*, 337:73, February 2016. doi: 10.1002/asna.201512268.

M. Dadina. Seyfert galaxies in the local Universe ($z \leq 0.1$): the average X-ray spectrum as seen by BeppoSAX. *A & A*, 485:417–424, Jul 2008. doi: 10.1051/0004-6361:20077569.

D. O. Edge, J. R. Shakeshaft, W. B. McAdam, J. E. Baldwin, and S. Archer. A survey of radio sources at a frequency of 159 Mc/s. *Memoirs of the Royal Astronomical Society*, 68:37–60, January 1959.

G. Fabbiano, D. W. Kim, and G. Trinchieri. An X-Ray Catalog and Atlas of Galaxies. *The Astrophysical Journal Supplement Series*, 80:531, Jun 1992. doi: 10.1086/191675.

Andrew C. Fabian and Giovanni Miniutti. The X-ray spectra of accreting Kerr black holes. *arXiv e-prints*, art. astro-ph/0507409, July 2005.

B. L. Fanaroff and J. M. Riley. The morphology of extragalactic radio sources of high and low luminosity. *MNRAS*, 167:31P–36P, May 1974. doi: 10.1093/mnras/167.1.31P.

I. Fernini. Very Large Array Images at 8.4 Ghz of 40 Fanaroff-Riley II 3CR Radio Sources with 0.1 z 2.0. *ApJS*, 212:19, June 2014. doi: 10.1088/0067-0049/212/2/19.

David J. E. Floyd, Marek J. Kukula, James S. Dunlop, Ross J. McLure, Lance Miller, Will J. Percival, Stefi A. Baum, and Christopher P. O'Dea. The host galaxies of luminous quasars. *MNRAS*, 355:196–220, Nov 2004. doi: 10.1111/j.1365-2966.2004.08315.x.

G. Fossati, L. Maraschi, A. Celotti, A. Comastri, and G. Ghisellini. A unifying view of the spectral energy distributions of blazars. *MNRAS*, 299:433–448, September 1998. doi: 10.1046/j.1365-8711.1998.01828.x.

M. A. Gendre, P. N. Best, J. V. Wall, and L. M. Ker. The relation between morphology, accretion modes and environmental factors in local radio AGN. *MNRAS*, 430:3086–3101, Apr 2013. doi: 10.1093/mnras/stt116.

G. Ghisellini and A. Celotti. The dividing line between FR I and FR II radio-galaxies. *A & A*, 379:L1–L4, Nov 2001. doi: 10.1051/0004-6361:20011338.

G. Ghisellini, F. Haardt, and G. Matt. The contribution of the obscuring torus to the X-ray spectrum of Seyfert galaxies: a test for the unification model. *MNRAS*, 267:743–754, April 1994. doi: 10.1093/mnras/267.3.743.

G. Ghisellini, F. Tavecchio, L. Maraschi, A. Celotti, and T. Sbarrato. The power of relativistic jets is larger than the luminosity of their accretion disks. *Nature*, 515:376–378, November 2014. doi: 10.1038/nature13856.

G. Giovannini, G. B. Taylor, L. Feretti, W. D. Cotton, L. Lara, and T. Venturi. The Bologna Complete Sample of Nearby Radio Sources. *ApJ*, 618:635–648, Jan 2005. doi: 10.1086/426106.

Gopal-Krishna and P. J. Wiita. Extragalactic radio sources with hybrid morphology: implications for the Fanaroff-Riley dichotomy. *A & A*, 363:507–516, November 2000a.

Gopal-Krishna and P. J. Wiita. Extragalactic radio sources with hybrid morphology: implications for the Fanaroff-Riley dichotomy. *A & A*, 363:507–516, November 2000b.

Karl D. Gordon, Geoffrey C. Clayton, K. A. Misselt, Arlo U. Land olt, and Michael J. Wolff. A Quantitative Comparison of the Small Magellanic Cloud, Large Magellanic Cloud, and Milky Way Ultraviolet to Near-Infrared Extinction Curves. *ApJ*, 594:279–293, Sep 2003. doi: 10.1086/376774.

Paola Grandi. Seeking for photoionized plasma in the Narrow Line radio Galaxy 3C 33. XMM-Newton Proposal, Oct 2007.

R. C. Hartman, D. L. Bertsch, S. D. Bloom, A. W. Chen, P. Deines-Jones, J. A. Esposito, C. E. Fichtel, D. P. Friedlander, S. D. Hunter, L. M. McDonald, P. Sreekumar, D. J. Thompson, B. B. Jones, Y. C. Lin, P. F. Michelson, P. L. Nolan, W. F. Tompkins, G. Kanbach, H. A. Mayer-Hasselwander, A. Mücke, M. Pohl, O. Reimer, D. A. Kniffen, E. J. Schneid, C. von Montigny, R. Mukherjee, and B. L. Dingus. The Third EGRET Catalog of High-Energy Gamma-Ray Sources. *The Astrophysical Journal Supplement Series*, 123:79–202, Jul 1999. doi: 10.1086/313231.

M. Harvanek and M. J. Hardcastle. A VLA Study of 15 3CR Radio Galaxies. *ApJS*, 119:25–39, November 1998. doi: 10.1086/313154.

Timothy M. Heckman and Philip N. Best. The Coevolution of Galaxies and Supermassive Black Holes: Insights from Surveys of the Contemporary Universe. *Annual Review of Astronomy and Astrophysics*, 52:589–660, Aug 2014. doi: 10.1146/annurev-astro-081913-035722.

Predrag Jovanović and Luka Č. Popović. X-ray Emission From Accretion Disks of AGN: Signatures of Supermassive Black Holes. *arXiv e-prints*, art. arXiv:0903.0978, March 2009.

P. M. W. Kalberla, W. B. Burton, Dap Hartmann, E. M. Arnal, E. Bajaja, R. Morras, and W. G. L. Pöppel. The Leiden/Argentine/Bonn (LAB) Survey of Galactic HI. Final data release of the combined LDS and IAR surveys with improved stray-radiation corrections. *A & A*, 440:775–782, Sep 2005. doi: 10.1051/0004-6361:20041864.

Jun Kataoka and Łukasz Stawarz. X-Ray Emission Properties of Large-Scale Jets, Hot Spots, and Lobes in Active Galactic Nuclei. *ApJ*, 622:797–810, April 2005. doi: 10.1086/428083.

Guinevere Kauffmann and Timothy M. Heckman. Feast and Famine: regulation of black hole growth in low-redshift galaxies. *MNRAS*, 397:135–147, Jul 2009. doi: 10.1111/j.1365-2966.2009.14960.x.

K. I. Kellermann, R. Sramek, M. Schmidt, D. B. Shaffer, and R. Green. VLA Observations of Objects in the Palomar Bright Quasar Survey. *ApJ*, 98:1195, October 1989. doi: 10.1086/115207.

Lisa J. Kewley, Brent Groves, Guinevere Kauffmann, and Tim Heckman. The host galaxies and classification of active galactic nuclei. *MNRAS*, 372:961–976, November 2006. doi: 10.1111/j.1365-2966.2006.10859.x.

R. P. Kraft, J. Azcona, W. R. Forman, M. J. Hardcastle, C. Jones, and S. S. Murray. The Hot Gas Environment of the Radio Galaxy 3C 388: Quenching the Accumulation of Cool Gas in a Cluster Core by a Nuclear Outburst. *ApJ*, 639:753–760, Mar 2006. doi: 10.1086/499488.

R. P. Kraft, M. Birkinshaw, P. E. J. Nulsen, D. M. Worrall, J. H. Croston, W. R. Forman, M. J. Hardcastle, C. Jones, and S. S. Murray. An Active Galactic Nucleus Driven Shock in the Intracluster Medium around the Radio Galaxy 3C 310. *ApJ*, 749:19, Apr 2012. doi: 10.1088/0004-637X/749/1/19.

R. A. Laing, J. M. Riley, and M. S. Longair. Bright radio sources at 178 MHz : flux densities, optical identifications and the cosmological evolution of powerful radio galaxies. *MNRAS*, 204:151–187, July 1983. doi: 10.1093/mnras/204.1.151.

R. A. Laing, C. R. Jenkins, J. V. Wall, and S. W. Unger. Spectrophotometry of a Complete Sample of 3CR Radio Sources: Implications for Unified Models. In Geoffrey V. Bicknell, Michael A. Dopita, and Peter J. Quinn, editors, *The Physics of Active Galaxies*, volume 54 of *Astronomical Society of the Pacific Conference Series*, page 201, January 1994.

D. V. Lal, R. P. Kraft, W. R. Forman, M. J. Hardcastle, C. Jones, P. E. J. Nulsen, D. A. Evans, J. H. Croston, and J. C. Lee. A Chandra Observation of 3C 288—Reheating the Cool Core of a 3 keV Cluster from a Nuclear Outburst at z = 0.246. *ApJ*, 722:1735–1743, Oct 2010. doi: 10.1088/0004-637X/722/2/1735.

G. Lanzuisi, P. Ranalli, I. Georgantopoulos, A. Georgakakis, I. Delvecchio, T. Akylas, S. Berta, A. Bongiorno, M. Brusa, N. Cappelluti, F. Civano, A. Comastri, R. Gilli, C. Gruppioni, G. Hasinger, K. Iwasawa, A. Koekemoer, E. Lusso, S. Marchesi, V. Mainieri, A. Merloni, M. Mignoli, E. Piconcelli, F. Pozzi, D. J. Rosario, M. Salvato, J. Silverman, B. Trakhtenbrot, C. Vignali, and G. Zamorani. Compton thick AGN in the XMM-COSMOS survey. *A & A*, 573:A137, January 2015. doi: 10.1051/0004-6361/201424924.

J. P. Leahy and R. A. Perley. VLA images of 23 extragalactic radio sources. *ApJ*, 102:537–561, August 1991. doi: 10.1086/115892.

J. P. Leahy and A. G. Williams. The bridges of classical double radio sources. *MNRAS*, 210:929–951, October 1984. doi: 10.1093/mnras/210.4.929.

Wenhao Liu, Ming Sun, Paul Nulsen, Tracy Clarke, Craig Sarazin, William Forman, Massimo Gaspari, Simona Giacintucci, Dharam Vir Lal, and Tim Edge. AGN feedback in galaxy group 3C 88: cavities, shock, and jet reorientation. *MNRAS*, 484:3376–3392, Apr 2019. doi: 10.1093/mnras/stz229.

K.-H. Mack, U. Klein, C. P. O'Dea, and A. G. Willis. Multi-frequency radio continuum mapping of giant radio galaxies. , 123:423–444, June 1997. doi: 10.1051/aas:1997166.

Juan P. Madrid, Marco Chiaberge, David Floyd, William B. Sparks, Duccio Macchetto, George K. Miley, David Axon, Alessandro Capetti, Christopher P. O'Dea, Stefi Baum, Eric Perlman, and Alice Quillen. Hubble Space Telescope Near-Infrared Snapshot Survey of 3CR Radio Source Counterparts at Low Redshift. *The Astrophysical Journal Supplement Series*, 164:307–333, Jun 2006. doi: 10.1086/504480.

John Magorrian, Scott Tremaine, Douglas Richstone, Ralf Bender, Gary Bower, Alan Dressler, S. M. Faber, Karl Gebhardt, Richard Green, Carl Grillmair, John Kormendy, and Tod Lauer. The Demography of Massive Dark Objects in Galaxy Centers. *ApJ*, 115:2285–2305, June 1998. doi: 10.1086/300353.

Alessandro Marconi and Leslie K. Hunt. The Relation between Black Hole Mass, Bulge Mass, and Near-Infrared Luminosity. *ApJ*, 589:L21–L24, May 2003. doi: 10.1086/375804.

André R. Martel, Stefi A. Baum, William B. Sparks, Eric Wyckoff, John A. Biretta, Daniel Golombek, Ferdinando D. Macchetto, Sigrid de Koff, Patrick J. McCarthy, and George K. Miley. Hubble Space Telescope Snapshot Survey of 3CR Radio Source Counterparts. III. Radio Galaxies with z<0.1. *The Astrophysical Journal Supplement Series*, 122:81–108, May 1999. doi: 10.1086/313205.

Giorgio Matt. Iron K.alpha resonant absorption in warm around active galactic nuclei. *MNRAS*, 267:L17–L20, Apr 1994. doi: 10.1093/mnras/267.1.L17.

Patrick J. McCarthy, Hyron Spinrad, and Wil van Breugel. Emission-Line Imaging of 3CR Radio Galaxies. I. Imaging Data. *The Astrophysical Journal Supplement Series*, 99:27, Jul 1995. doi: 10.1086/192178.

Nicholas J. McConnell, Chung-Pei Ma, Karl Gebhardt, Shelley A. Wright, Jeremy D. Murphy, Tod R. Lauer, James R. Graham, and Douglas O. Richstone. Two ten-billion-solar-mass black holes at the centres of giant elliptical galaxies. *Nature*, 480:215–218, December 2011. doi: 10.1038/nature10636.

F. Meyer, B. F. Liu, and E. Meyer-Hofmeister. Re-condensation from an ADAF into an inner disk: the intermediate state of black hole accretion? *A & A*, 463:1–9, February 2007. doi: 10.1051/0004-6361:20066203.

Giulia Migliori, Paola Grandi, Giorgio G. C. Palumbo, Gianfranco Brunetti, and Carlo Stanghellini. Radio Lobes of Pictor A: An X-Ray Spatially Resolved Study. *ApJ*, 668:203–208, October 2007. doi: 10.1086/520870.

H. Miraghaei and P. N. Best. The nuclear properties and extended morphologies of powerful radio galaxies: the roles of host galaxy and environment. *MNRAS*, 466:4346–4363, Apr 2017. doi: 10.1093/mnras/stx007.

I. G. Momcheva, J. C. Lee, C. Ly, S. Salim, D. A. Dale, M. Ouchi, R. Finn, and Y. Ono. Nebular Attenuation in Hα-selected Star-forming Galaxies at z = 0.8 from the NewHα Survey. *ApJ*, 145:47, February 2013. doi: 10.1088/0004-6256/145/2/47.

R. Morganti, N. E. B. Killeen, and C. N. Tadhunter. The radio structures of southern 2-Jy radio sources. *MNRAS*, 263:1023–1048, Aug 1993a. doi: 10.1093/mnras/263.4.1023.

R. Morganti, N. E. B. Killeen, and C. N. Tadhunter. The radio structures of southern 2-Jy radio sources. *MNRAS*, 263:1023–1048, August 1993b. doi: 10.1093/mnras/263.4.1023.

Ramesh Narayan and Insu Yi. Advection-dominated Accretion: A Self-similar Solution. *ApJ*, 428:L13, June 1994. doi: 10.1086/187381.

S. G. Neff, L. Roberts, and J. B. Hutchings. VLA Maps of Radio Galaxies to Z = 1. *The Astrophysical Journal Supplement Series*, 99:349, Aug 1995. doi: 10.1086/192190.

Donald E. Osterbrock. *Astrophysics of gaseous nebulae and active galactic nuclei*. 1989.

V. Patiño-Álvarez, V. Chavushyan, J. León-Tavares, J. R. Valdés, A. Carramiñana, L. Carrasco, and J. Torrealba. Optical Spectrophotometric Monitoring of Fermi/LAT Bright Sources. *arXiv e-prints*, art. arXiv:1303.1893, March 2013.

E. Piconcelli, S. Bianchi, G. Miniutti, F. Fiore, M. Guainazzi, E. Jimenez-Bailon, and G. Matt. Heavy absorption and soft X-ray emission lines in the XMM-Newton spectrum of the type 2 radio-loud quasar 3C 234. *A & A*, 480:671–676, Mar 2008. doi: 10.1051/0004-6361:20078746.

P. Pjanka, A. A. Zdziarski, and M. Sikora. The power and production efficiency of blazar jets. *MNRAS*, 465:3506–3514, March 2017. doi: 10.1093/mnras/stw2960.

G. G. Pooley and S. N. Henbest. Observations of 48 extragalactic radio sources with the Cambridge 5-km telescope at 5 GHz. *MNRAS*, 169:477–526, December 1974. doi: 10.1093/mnras/169.3.477.

S. Rawlings, R. Saunders, P. Miller, M. E. Jones, and S. A. Eales. A New Identification for the Giant Radiosource 3C326. *MNRAS*, 246:21P, October 1990.

Christopher S. Reynolds, Laura W. Brenneman, and John T. Stocke. The interaction of 3C 401 with the surrounding intracluster medium. *MNRAS*, 357:381–386, Feb 2005. doi: 10.1111/j.1365-2966.2005.08669.x.

F. Ricci, L. Lovisari, R. P. Kraft, F. Massaro, A. Paggi, E. Liuzzo, G. Tremblay, W. R. Forman, S. Baum, C. O'Dea, and B. Wilkes. Stormy Weather in 3C 196.1: Nuclear Outbursts and Merger Events Shape the Environment of the Hybrid Radio Galaxy 3C 196.1. *ApJ*, 867:35, November 2018. doi: 10.3847/1538-4357/aae487.

G. Risaliti and M. Elvis. A Panchromatic View of AGN. In A. J. Barger, editor, *Supermassive Black Holes in the Distant Universe*, volume 308 of *Astrophysics and Space Science Library*, page 187, August 2004. doi: 10.1007/978-1-4020-2471-9_6.

R. T. Schilizzi, W. W. Tian, J. E. Conway, R. Nan, G. K. Miley, P. D. Barthel, M. Normandeau, D. Dallacasa, and L. I. Gurvits. VLBI, MERLIN and HST observations of the giant radio galaxy 3C 236. *A & A*, 368:398–407, March 2001. doi: 10.1051/0004-6361:20000288.

N. I. Shakura and R. A. Sunyaev. Reprint of 1973A&A....24..337S. Black holes in binary systems. Observational appearance. *A & A*, 500:33–51, June 1973.

M. Sikora, Ł. Stawarz, and J.-P. Lasota. Radio Loudness of Active Galactic Nuclei: Observational Facts and Theoretical Implications. *ApJ*, 658:815–828, April 2007. doi: 10.1086/511972.

S. R. Spangler and A. H. Bridle. Dual-frequency VLA observations of the extended radio galaxy 3C 166. *ApJ*, 87:1270–1278, September 1982. doi: 10.1086/113212.

S. R. Spangler, S. T. Myers, and J. J. Pogge. VLA observations of radio galaxies with extended lobe emission - 3C 79 and 3C 430. *ApJ*, 89:1478–1486, October 1984. doi: 10.1086/113649.

H. Spinrad, S. Djorgovski, J. Marr, and L. Aguilar. A third update of the status of the 3 CR sources : further new redshifts and new identifications of distant galaxies. *Publications of the Astronomical Society of the Pacific*, 97:932–961, October 1985. doi: 10.1086/131647.

M. R. Swain, A. H. Bridle, and S. A. Baum. Internal Structure of the Jets in 3C 353. *ApJL*, 507: L29–L33, November 1998. doi: 10.1086/311663.

Clive Tadhunter. Radio AGN in the local universe: unification, triggering and evolution. *Astronomy and Astrophysics Review*, 24:10, June 2016. doi: 10.1007/s00159-016-0094-x.

G. B. Taylor, D. H. Hough, and T. Venturi. Very Long Baseline Array Polarimetry of Three Powerful Radio Galaxy Cores. *ApJ*, 559:703–709, October 2001. doi: 10.1086/322355.

Yuichi Terashima and Andrew S. Wilson. Chandra Snapshot Observations of Low-Luminosity Active Galactic Nuclei with a Compact Radio Source. *ApJ*, 583:145–158, January 2003. doi: 10.1086/345339.

E. Torresi. The nuclear environment of 3C 33 as observed by Chandra and XMM-Newton. In *High Resolution X-ray Spectroscopy: Towards IXO*, page E43, Sep 2009.

E. Torresi, P. Grandi, A. Capetti, R. D. Baldi, and G. Giovannini. X-ray study of a sample of FR0 radio galaxies: unveiling the nature of the central engine. *MNRAS*, 476:5535–5547, June 2018. doi: 10.1093/mnras/sty520.

Scott Tremaine, Karl Gebhardt, Ralf Bender, Gary Bower, Alan Dressler, S. M. Faber, Alexei V. Filippenko, Richard Green, Carl Grillmair, Luis C. Ho, John Kormendy, Tod R. Lauer, John Magorrian, Jason Pinkney, and Douglas Richstone. The Slope of the Black Hole Mass versus Velocity Dispersion Correlation. *ApJ*, 574:740–753, August 2002. doi: 10.1086/341002.

Jonathan R. Trump, Chris D. Impey, Patrick J. McCarthy, Martin Elvis, John P. Huchra, Marcella Brusa, Gunther Hasinger, Eva Schinnerer, Peter Capak, Simon J. Lilly, and Nick Z. Scoville. Magellan Spectroscopy of AGN Candidates in the COSMOS Field. *The Astrophysical Journal Supplement Series*, 172:383–395, September 2007. doi: 10.1086/516578.

C. Megan Urry and Paolo Padovani. Unified Schemes for Radio-Loud Active Galactic Nuclei. *Publications of the Astronomical Society of the Pacific*, 107:803, September 1995. doi: 10.1086/133630.

J. V. Wall and J. A. Peacock. Bright extragalactic radio sources at 2.7 GHz- III. The all-sky catalogue. *MNRAS*, 216:173–192, September 1985. doi: 10.1093/mnras/216.2.173.

A. S. Wilson, A. J. Young, and P. L. Shopbell. Chandra X-Ray Observations of Pictor A: High-Energy Cosmic Rays in a Radio Galaxy. *ApJ*, 547:740–753, February 2001. doi: 10.1086/318412.

Ye Yuan, Min-Feng Gu, and Yong-Jun Chen. The pc-scale radio structure of MIR-observed radio galaxies. *Research in Astronomy and Astrophysics*, 18:108, Aug 2018. doi: 10.1088/1674-4527/18/9/108.